Politecnico di Milano

School of Industrial and Information Engineering

Master of Science in Materials Engineering and Nanotechnology

Development of Ta:TiO_2 plasmonic multilayer metamaterials

Supervisor: Prof. Andrea Li Bassi
Co-Supervisor: Dr. Cristina Mancarella

Master thesis of:
Lorenzo Stasi
919090

Academic Year 2019-2020

E tutti quei momenti andranno perduti nel tempo,
come lacrime nella pioggia.
Roy Batty/Rutger Hauer, Blade Runner, 1982

Tutta quella città, non si riusciva a vederne la fine [...]
Non è quello che vidi che mi fermò, Max. È quello che non vidi.
Puoi capirlo? Quello che non vidi...
In tutta quella sterminata città c'era tutto tranne la fine. C'era tutto.
Ma non c'era una fine. Quello che non vidi è dove finiva tutto quello.
La fine del mondo.
Novecento/Tim Roth, La leggenda del pianista sull'oceano, 1998

Hai aspettato molto?
Tutta la vita.
Deborah/Elizabeth McGovern a Noodles/Robert De Niro, C'era una volta in america, 1984

E allora, che cosa aveva scritto [Spada Spezzata]?
Sotto un unico cielo.
Il re di Qin/Daoming Chen rivolto a Senza Nome/Jet Li, Hero, 2002

Abstract

Plasmonics, the study of resonant interaction of electromagnetic waves with free electrons in condensed matter is an expanding research field. Metals such as gold and silver have demonstrated to be excellent choices for UV-Vis operation range. However, these metals have high optical losses approaching the infrared (IR) range. Therefore, Transparent Conductive Oxides (TCOs) have attracted increasing interest for plasmonic application in the IR. A promising candidate is Ta:TiO_2 (TaTO), displaying high carrier density and good chemical stability.

Metamaterials (artificial structured materials) exploit plasmonic effects to generate properties not observed in nature. The main interest lies in the possibility to obtain negative refraction, hence overcoming the diffraction limit of conventional lenses. Hyperbolic metamaterials (HMMs) are a sub-class that have gained particular attention due to the simple geometry and ease of fabrication. In fact, they can be obtain with multilayers structure, alternating metallic and dielectric layers or with metallic nanowires array in a dielectric matrix. Many are the example of Au and Ag combined with alumina and titania for the UV-Vis range, but the literature is still scarse for what concern the IR range. This thesis work aims to expand the knowledge about TaTO in the light of developing future plasmonic multilayers metamaterials. Multilayers were deposited by the pulsed laser deposition (PLD) method. PLD allows to deposit conductive and non-conductive layers using this material just via changing the deposition pressure. Exploiting this feature, a single step deposition can be performed without opening the vacuum chamber, drastically reducing the operating time.

A preliminary study was conducted on the single components that were later used in the multilayers. Thin films (20 nm, 10 nm, 5 nm) of Ta(10%):TiO_2 were deposited at 1 Pa in pure O_2 on glass substrate in order to evaluate their crystallization and electrical properties. Later, these three films were deposited on polycrystalline stoichiometric titania substrate. Such substrate helped the crystallization process thus ensuring improved electrical properties. Then, the effects of higher deposition pressure were analyzed. Ta(10%):TiO_2 films deposited at 3 Pa and 6 Pa in pure O_2 resulted both non-conductive, but the former crystal-

lized whereas the latter did not. Higher deposition pressures were explored on Ta(5%):TiO_2 as well. Film at 6 Pa in pure O_2 resulted amorphous and non-conductive as for Ta(10%):TiO_2. Film deposited at 3 Pa in mixed background atmosphere (Ar:O_2=5:1) turned out conductive and crystalline.

Successively, several multilayers were deposited. Metallic layers were obtained depositing TaTO at 1 Pa in pure O_2, whereas non-conductive ones were deposited at 3 Pa or 6 Pa in pure O_2. Multilayers with both 5% and 10% Ta concentration were synthesized. Different single layer thicknesses were explored in order to observe differences in the electrical and optical properties. Lastly, an attempt to create a fully conductive metamaterials was tried. Ta(5%):TiO_2 layers deposited at 1 Pa in pure O_2 were alternated with layers at 3 Pa in mixed atmosphere (Ar:O_2=5:1). Unfortunately, the result was not satisfying.

This thesis work is an preliminary and exploratory study on the synthesis, the structural, morphological, electrical and optical properties of these multilayers in the Vis-NIR range.

In the future, ellipsometric analysis should be performed in order to assess the hyperbolic regime, if present, of these multilayers. Moreover, the geometry dependence on the optical and electrical properties was not completely explored. The effect of the layers number has to be investigated too. Furhtermore, the combination of TaTO with TiO_2 could be invastigated, as well as the combination of TCOs and metals for a fully conductive multilayers with hyperbolic dispersion in the Vis-NIR.

Sommario

La plasmonica, lo studio dell'interazione risonante delle onde elettromagnetiche con gli elettroni liberi nella materia è un campo di ricerca in espansione. Metalli come oro e argento si sono dimostrati scelte eccellenti per il range UV-Vis. Tuttavia, questi metalli soffrono di grandi dissipazioni ottiche approcciando l'infrarosso (IR). Perciò, gli ossidi trasparenti conduttivi (TCO) hanno attratto un interesse crescente per applicazioni plasmoniche nell'IR. Un promettente candidato è Ta:TiO_2 (TaTO) che possiede un'alta densità di portatori e buona stabilità chimica.

I metamateriali (materiali artificialmente strutturati) sfruttano effetti plasmonici per generare proprietà non osservate in natura. L'interesse principale risiede nella possibilità di ottenere rifrazione negativa, quindi superare il limite di diffrazione delle lenti convenzionali. I metamateriali iperbolici (HMM) sono una sotto classe che ha ottenuto particolare attenzione a causa della loro geometria semplice e della facilità di fabbricazione. Infatti, possono essere ottenuti con una struttura a multilayer, alternando layer metallici e dielettrici, oppure con una disposizione ordinata di nanofili metallici in una matrice dielettrica. Molti sono gli esempi di Au o Ag combinati con alluminia o titania per il range UV-Vis, ma la letteratura è ancora scarsa per quanto riguarda l'IR. Questo lavoro di tesi punta a espandere la conoscenza del TaTO per uno sviluppo futuro di multilayer come metamateriale plasmonico. I multilayers sono stati depositati attraverso l'ablazione a laser pulsato (PLD). La PLD permette di depositare layer conduttivi e non di questo materiale, cambiando semplicemente la pressione di deposizione. Sfruttando questa caratteristica, è possibile depositare multilayer in un single-step, senza aprire la camera a vuoto, riducendo enormemente i tempi di operazione.

Uno studio preliminare è stato condotto sulle singole componenti che sarebbero state poi utilizzate nel multilayer. Film sottili (20 nm, 10 nm, 5 nm) di Ta(10%):TiO_2 sono stati depositati a 1 Pa in puro O_2 su un substrato di vetro, per valutare il loro grado cristallino e le loro proprietà elettriche. In seguito, gli stessi tre film sono stati depositati su un substrato policristallino di titania stechiometrica. Questo substrato ha aiutato il processo di cristallizzazione migliorando le proprietà elettriche. Successivamente, l'effetto di pressioni di deposizioni

più alte è stato analizzato. Film di Ta(10%):TiO_2 depositati a 3 Pa e 6 Pa in puro O_2 sono risultati non conduttivi, ma quello a 3 Pa ha cristallizzato mentre quello a 6 Pa no. Pressioni di deposizioni maggiori sono state esplorate anche per Ta(5%):TiO_2. Film a 6 Pa in puro O_2 sono risultati amorfi e non conduttivi come per Ta(10%):TiO_2. Film depositati a 3 Pa in un atmosfera mista (Ar:O_2=5:1) si sono rivelati conduttivi e cristallini.

Successivamente, diversi multilayers sono stati prodotti. I layer metallici sono stati ottenuti depositando TaTO a 1 Pa in puro O_2, mentre quelli non conduttivi sono stati depositati a 3 Pa o 6 Pa in puro O_2. I multilayers sono stati prodotti con una concentrazione di Ta pari al 5% e al 10%. Diversi spessori dei singoli sono stati sperimentati in modo da osservare differenze nelle properietà elettriche e ottiche. Infine, è stata provata la realizzazione di un multilayer interamente conduttivo. Layer di Ta(5%):TiO_2 depositati a 1 Pa in puro O_2 sono stati alternati a layer depositati a 3 Pa in atmosfera mista (Ar:O_2=5:1). Purtroppo, il risultato ottenuto non è stato soddisfacente.

Questo lavoro di tesi è uno studio preliminare ed esplorativo sulla sintesi e le proprietà strutturali, morfologiche, elettriche ed ottiche di questi multilayer nel range Vis-NIR.

Come prospettiva, un'analisi ellissometrica dovrebbe essere fatta in modo da scoprire il regime iperbolico, se presente, di questi multilayer. In più, la dipendenza geometrica sulle proprietà ottiche ed elettriche non è stata esplorata completamente. Gli effetti del numero di layer non sono stati investigati. Inoltre, anche la combinazione di TaTO con TiO_2 potrebbe essere investigata come le combinazioni di altri TCO con metalli per un multilayer totalmente conduttivo con una dispersione iperbolica nel Vis-NIR.

Ringraziamenti

Un ringraziamento speciale va a tutti i miei compagni di percorso che hanno reso questi cinque anni un'avventura indimenticabile. Senza di loro non sarei arrivato dove sono ora. Ringrazio dunque Alberto Quendolo, Daniele Visco, Stefano Reale, Emanuele Urbinati, Michele Valsecchi, Marco Benoliel, Lucia Simoncelli, Andrea Palmeri, Federico Rabino, Filippo Spada, Federico Aliprandi, Eugenio Chini, Matteo Colosio, Lorenzo Rossi, Guglielmo Campanella, Anthony Albanese, Martina Colombo, Sara Capitanio e Francesco Virgilio.

Un grazie è rivolto ai miei amici d'infanzia che mi hanno accompagnato durante tutta la vita, facendomi crescere e riflettere: Lorenzo Colli, Luca Bartolomei, Jacopo Rosi e Michela Bocchi.

Un ringraziamento va ovviamente verso i miei genitori e mio fratello che mi hanno sopportato e sostenuto durante le mie fatiche. Grazie per l'educazione, i valori e il forte senso di responsabilità che mi avete trasmesso.

Un grazie è dovuto ai miei professori del liceo i cui insegnamenti mi hanno fatto diventare un uomo migliore: Prof. Paolo Quaglia, Prof. Ivan Cervesato, Prof.ssa Giovanna Rodella, Prof.ssa Anna Del Viscovo.

Infine, voglio ringraziare il mio relatore e Prof. Andrea Li Bassi e la mia dottoranda Cristina Mancarella che hanno reso possibile questo lavoro di tesi sperimentale in un momento così delicato, come la pandemia di coronavirus.

Lorenzo Stasi, *19 Novembre 2020*

Contents

List of Figures

List of Tables

Introduction

Plasmonics studies the resonant interaction between light and the conduction electron gas in condensed matter. Electron gas is present in metals, since the outer valence electrons of each atom are shared and free to move throughout the crystal lattice. Thus, electrons can resonate with the electromagnetic (EM) radiation and oscillate collectively with respect the fixed background positive ions. The quantum of these oscillations is called bulk plasmon [1] and occurs at the plasma frequency ω_p. The latter depends on the carrier density n and the electron effective mass m^* of the material. At a planar metal-dielectric interface, a different plasmonic excitation can be generated: Surface Plasmon Polaritons (SPPs). SPPs are electromagnetic excitations of surface charges, propagating along the interface and evanescently confined in the perpendicular direction.

Gold and silver are the most employed metals for plasmonic applications in the UV-Vis, due to their optimal electrical properties. However, these metals suffer of high optical losses in the NIR range due to intraband transition. In addition, metals present a percolation limit when deposited on unideal substrate, setting a lower limit on the thickness. Furthermore, the plasma frequency of metals can not be tuned with flexibility, since the only parameters at disposal are the size and shape of nanoparticles. Therefore, the need for new materials capable of overcoming these problems has emerged. A promising class of mateirals is represented by Transparent Conductive Oxides (TCOs). TCOs are metal oxides that under heavy doping ($> 5\%$) become degenerate semiconductors. TCOs merge the high optical transparency in the Vis range with high carrier density ($\sim \times 10^{20}$ cm^{-3}) and low resistivity ($\sim \times 10^{-4}$ Ωcm). TCOs are compatible with CMOS (Complementary Metal-Oxide Semiconductor) technology and exhibit the plasma frequency in the NIR, due to the lower carrier density with respect to metals. The most employed TCO is ITO (indium tin oxide), but the presence of expensive indium pushed the research toward new materials. AZO (aluminum-doped zinc oxide) is a good candidate, being non-toxic and easy to fabricate, but it displays worse electrical properties than ITO. Another promising candidate is V group-doped TiO_2 (TaTO). Both Nb and Ta were explored but Ta has proven higher

solubility in the anatase crystalline structure of TiO_2 and the lower predicted electron effective mass. Hence, it is possible to increase the dopant concentration without affecting the mobility too much. Therefore, the plasma frequency can be tuned more easily.

Metamaterials (MMs) are engineered structured materials which exhibit properties not found in nature. The main interesting feature of MMs is the possibility to have negative refraction, if both the dielectric permittivity ε_r and the magnetic permeability μ_r are negative. Such properties could be exploited to create superlenses, able to overcome the diffraction limit. However, a MM with both negative ε_r and negative μ_r is difficult to obtain, thus scientists focused on a MM sub-class: Hyperbolic Metamaterials (HMMs). Ease to fabricate, simple geometry and flexible wavelength tunability are advantages that HMMs can offer. In fact, HMMs can be realized alternating metal and dielectric layers in multilayers structure or with metallic nanowires arrays in a dielectric matrix. HMMs rely their properties in the extreme anisotropy of the geometrical structure. In fact, for specific wavelenght interval, HMMs can behave as metal in one direction (negative dielectric permittivity) and as dielectric in the others (positive dielectric permittivity). Hence, the isofrequency surface transforms from an ellipse into an hyperbole, allowing the transmission of high-k modes, that in common materials are evanescent modes. HMMs rely on the SPPs coupling between different interfaces in order to sustain the high-k modes. HMMs can be used to realize hyperlenses, but spontaneous emission enhancement and sensing can benefit too. Most of HMMs combine Au or Ag with alumina or titania, hence the hyperbolic regime is found in the UV-Vis range. To reach the infrared regime, TCOs are the right candidates. Few examples of HMMs made out of TCOs (AZO/ZnO or ITO/In_2O_3 multilayers) are reported in literature [2]–[6]. Thus, the possibility to use TaTO in multilayered structure to obtain a HMM in the NIR is attracting. Moreover, in previous work [7], [8] it was shown how TaTO films can be made conductive or insulating just by changing the oxygen deposition pressure. Therefore, in this thesis work a first development of TaTO-only multilayer metamaterials is investigated. The following is the structure of this thesis work:

- **Chapter 1** summarizes the physic of plasmonics effects and the properties of transparent conductive oxides. Then, an overview on HMMs, their applications and the current state of the art is presented.
- **Chapter 2** deals with experimental setup and techniques used in this thesis work.
- **Chapter 3** presents the preliminary study of this thesis work. The properties of the single components of the future multilayers were analyzed in order to

comprehend better the overall behaviour of the multilayers.

- **Chapter 4** discusses the synthesis and characterization of the TaTO-only multilayers. Different architectures, different Ta contents and pressures were explored in order to assess a correlation between these parameters and the final properties.
- **Chapter 5** recalls the results obtained in this thesis work and describes future progress that can be implemented to continue the research.

During this work, I personally worked on the synthesis of the samples through PLD and the subsequent thermal treatments, as well as 4-point probe measurements, SEM and Raman analysis. UV/Vis/NIR spectrophotometry measurements was performed by C. Mancarella, but I analyzed and discussed all the acquired data.

Chapter 1

Plasmonics nanostructures and novel metamaterials

1.1 Plasmonics

Interaction between light and matter has always attracted interest in science. Among the many generated effects, plasmonic ones have gained particularly attention in the last decade [1]. They can be defined as resonant interaction between the electro-magnetic (EM) field and the electron gas inside a material. Such phenomena are possible if electrons are free to move inside the material itself, thus this behaviour was first observed in metals by Bohm and Pines in the 50s [9]. The most studied metals were gold and silver due to their optimal electrical properties (resistivity of the order $\sim 3 \times 10^{-8}$ and tens $cm^2V^{-1}s^{-1}$ regarding the mobility); however these metals suffer from high optical losses because of intraband transition. Moreover, their plasmonics response is not tunable. All these drawbacks pushed the research to alternative plasmonics materials such as semiconductor, transparent conductive oxides, metal nitrides and 2D materials [10]. Nevertheless, metals are suitable for a variety of applications, spanning from photovoltaics, photocatalysis and sensor.

1.1.1 Metals and bulk plasmons

Metals are constituted by a crystal lattice of positive ions and an electron gas. The latter is composed by all the shared valence electrons of each atoms. Electrical properties of metals can be described easily by the Drude model. [11]. The conductive electrons are free to move throughout the lattice experiencing several collisions in a time scale called relaxation time τ. At the same time, scattering among electrons are considered negligible. As a consequence, the direct conduc-

tivity (DC) σ of electrons can be defined as follows:

$$\sigma = \frac{ne^2\tau}{m^*} \tag{1.1}$$

where n is the electron density, e is the electron charge, τ is the so-called relaxation time and m^* is the effective mass. The correct, complete derivation of the conductivity should be obtained by solving the Boltzmann equation of transport, within the relaxation-time approximation [11]. In order to asses the time-varying properties of metals, we need to consider an external EM wave of the form $\mathbf{E} = E_0 e^{-i\omega t}$. Writing the equation of motion for the electrons:

$$m^* \frac{d^2\mathbf{x}}{dt^2} + m^*\gamma \frac{d\mathbf{x}}{dt} = -e\mathbf{E} \tag{1.2}$$

where $\gamma = 1/\tau$ is the dumping frequency; finally, the complex dielectric function can be found:

$$\varepsilon(\omega) = \varepsilon_r \left(1 - \frac{\omega_p^2}{\omega^2 + i\gamma\omega}\right) \tag{1.3}$$

$$\omega_p = \sqrt{\frac{ne^2}{\varepsilon_0 \varepsilon_r m^*}} \tag{1.4}$$

where ε_r is the background permittivity, ε_0 is the dielecric constant of vacuum and ω_p is the *plasma frequency*. For a more complete description, the reader is invited to refer to Ashcroft & Mermin [11]. In Fig. 1.1, it can be seen that for $\omega < \omega_p$, EM waves cannot travel in it, whereas for $\omega > \omega_p$, EM waves are sustained inside the material. When $\omega = \omega_p$, the permittivity goes to 0 (i.e. $\varepsilon(\omega_p) = 0$). This condition corresponds to a collective longitudinal oscillation by the electron gas with respect the fixed positive background of the ions; the quanta of this oscillations are called *bulk plasmons*. For metals, the plasma frequency falls in the ultra-violet (UV) range due to the high electron density ($\sim 10^{22}\ cm^{-3}$).

1.1.2 Surface plasmon polaritons and metal dielectric interfaces

Bulk plasmons are not the only possible plasmonics excitations. Indeed, at the interface between a metal (ε_m) and a dielectric (ε_d), it is possible to generate *surface plasmons*. If the interface is planar, then we talk about *Surface Plasmon Polaritons* (SPPs). SPPs are electromagnetic excitations of surface charges, propagating along the interface and evanescently confined in the perpendicular direction [1] (see Fig. 1.2a). SPPs can be derived form the wave equation, with particular boundary conditions. The latter express the continuity of the tangential components of the electric and magnetic fields across the interface and the fields must decrease

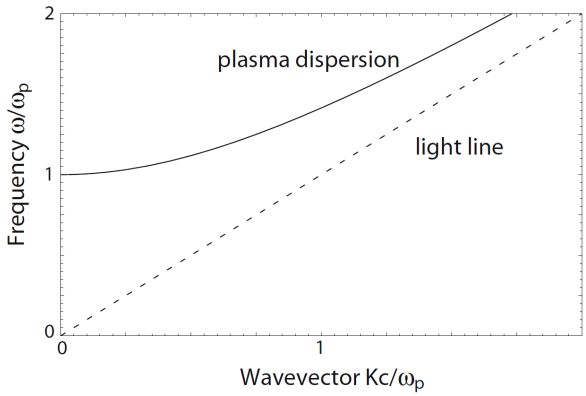

Figure 1.1: *Dispersion relation of a generic free electron gas. Taken from [1]*

away from the boundary and vanish infinitely far away [12]. The SPP dispersion relation is the following:

$$k = \frac{\omega}{c}\sqrt{\frac{\varepsilon_m \varepsilon_d}{\varepsilon_m + \varepsilon_d}} \tag{1.5}$$

where k is the in plane component of the wave vector and it is shown in Fig. 1.2b. At low frequency, the dispersion mode is close to the light line, whereas when frequency increases, it moves away from light-like behaviour and it tends asymptotically to:

$$\omega_{SPP} = \frac{\omega_p}{\sqrt{1+\varepsilon_d}} \tag{1.6}$$

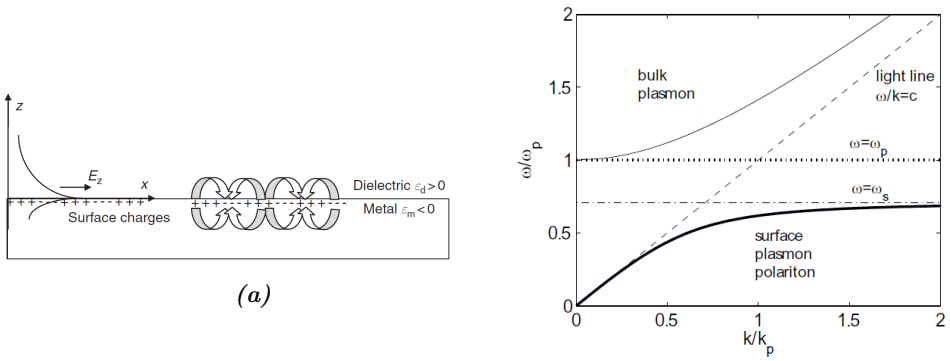

Figure 1.2: *(a) SPP mode. Electric charge and EM distribution at the interface. Taken from [13]. (b) Dispersion of SPP at metal-vacuum interface, where $k_p = \omega_p/c$. Adapted from [12].*

SPPs are surface waves, confined at the interface, hence they exist only if ε_m and ε_d have opposite sign. Moreover, SPPs can be excited only by transverse magnetic modes and they have longer momentum with respect to the photon at frequency ω. As a consequence, due to wavevector conservation, specific matching conditions

must be fulfilled in order to generate SPPs, for example prism coupling, grating coupling or near-field excitation [1]. The SPPs propagation length is defined as $L = 1/2Im[k_{SPP}]$, thus loss effects must be considered in order to obtained a truthful result. Losses are inglobed in the imaginary part of the dielectric function and linked to γ. Typical value of L are in the order of tens of μm. The penetration depth is instead different for metals and dielectric since it depends on the dielectric function of each component. Lastly, it is important to point out that a better confinement implies a lower propagation length.

1.1.3 Localized surface plasmon resonance from metal nanoparticles

The second important surface plasmons is observed in metal nanoparticles (NPs). In this case, we talk about *Localized Surface Plasmon Resonances* (LSPRs) [1]. LSPRs are non-propagating excitations of the conduction electrons of metal NPs coupled with EM wave (see Fig. 1.3). Contrary to SPPs, this excitation can be generated with direct light, thus no special matching conditions are required. The NPs dimensions are usually below 100 nm, much smaller with respect to the EM wavelength, thus the quasi-static approximation can be used [1]. Applying an external EM field will induce a dipole in the NPs, whose polarizability α is:

$$\alpha = 4\pi a^3 \frac{\varepsilon_m - \varepsilon_d}{\varepsilon_m + 2\varepsilon_d} \tag{1.7}$$

where a is the NP radius. The resonance condition is met when the denominator is minimum, thus when $Re[\varepsilon_m] = -2\varepsilon_d$, reached at the LSPR frequency:

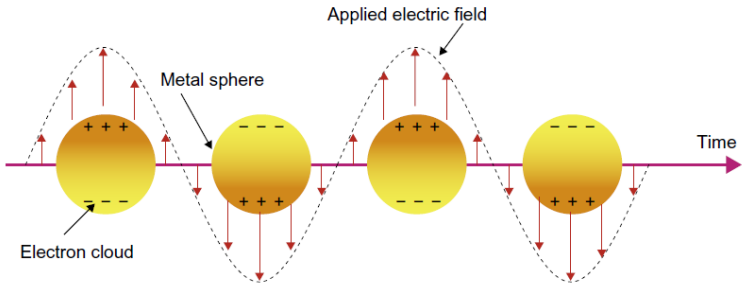

Figure 1.3: *Oscillation of the electron cloud caused by the external EM wave. Taken from [14].*

$$\omega_{LSPR} = \frac{\omega_p}{1 + 2\varepsilon_d} \tag{1.8}$$

The resonance condition is strongly dependent on the environment, opening the possibility of different matches between the dielectric and the metal NPs. However, LSPRs don't depend just on the surrounding. Size and shape as well have a strong influence; in particular, NPs with anisotropic shape can create two

different ω_{LSPR}. Lastly, the coupling effect between the NPs can raise additional effects. To properly describe the system, a more accurate and complex model is the Mie theory [1], which abandon the quasi-static approximation and used a rigorous electrodynamic approach.

1.2 Transparent conductive oxides

Transparent Conductive Oxides (TCOs) are a relatively new class of materials, which have found vast applications as electrodes in photovoltaic solar cells and in flat screen monitors [15]. TCOs merge high optical transparency in the visible range (350-750 nm) and low electrical resistivity ($\sim 10^{-4}\ \Omega cm$), though not as good as metals ($\sim 10^{-6}\ \Omega cm$). The most studied and employed TCO is indium-tin-oxide (ITO), displaying the lowest resistivity among all TCOs, good transparency and high stability in several environments [10], [16]. Nevertheless, indium is a very expensive and rare element, resulting in the need of new materials for applications. One good candidate, is zinc oxide, especially if doped with Al or Ga (respectively AZO and GZO). Being non-toxic, abundant and easy to fabricate, it has gained increasing attention [10], [16], even though it shows worse electrical properties with respect to ITO. Another promising candidate, is V group-doped (Ta or Nb) titanium dioxide, object of considerable research [7], [8], [17]–[20].

Furthermore, TCOs have attracted interest for the possibility to sustain plasmonic excitations in the near-infrared (NIR) regime, approaching the telecommunication window (1300 nm - 1550 nm), for a variety of novel applications. Such opportunity has opened due to the lower electron density with respect to metals. In fact, TCOs posses a carrier density spanning from $10^{19}\ cm^{-3}$ to $10^{21}\ cm^{-3}$, hence the plasma wavelength falls in the microwave range. Moreover, TCOs are compatible with CMOS (Complementary Metal-Oxide Semiconductor) technology and suffer from low optical losses, two crucial points in which metals fail, making TCOs promising materials for NIR plasmonics applications. In addition, the ease with which the plasma frequency can be tuned by changing the doping level is another advantage with respect to metals. In the future, TCOs can become the building block for plasmonics waveguides or metamaterials.

1.2.1 Doping

Metal oxide compounds are generally insulators, due to the ionic character in the chemical bonds and the large band gap (> 3 eV) [15]. In order to make them conducting, two approaches are possible: oxygen vacancies or extrinsic doping. In the former strategies, the material is tipically exposed to a reducing atmosphere,

generating a sub-stoichiometric compound [17]. The oxygen vacancies will act as double electron donors, but the carrier density achievable is not so high ($\sim 10^{19}$ cm^{-3}) [17]. In the latter, the material is heavily doped ($> 5\%$) by adding other elements/species in order to achieve p-type or n-type conduction. It is important to point out that a perfect stoichiometry can hinder the doping effect, thus a combination of both mechanisms is preferred. In addition, Qi *et al.* [21] showed how oxygen-rich atmosphere during the growth of TiO_2 promotes the formation of cationic vacancies, that act as electron killers. Furthermore, doping cannot be too high, otherwise the plasma frequency would blue-shift toward the Vis, the mobility would drop and transparency window would be reduced.

1.2.2 Electrical properties

Charge transport in TCOs can be effectively described by the Drude's model like for metals. TCOs posses a lower carrier density than metals, but more scattering mechanisms are present: electron-phonon scattering, ionized impurity scattering (Fig. 1.4b), grain boundary (GB) scattering (Fig. 1.4a) and surface scattering. The first is always present, in all materials, whereas the last one is significant only for thin films. The second is a typical characteristic of doped compounds. Indeed, TCOs (and semiconductors) rely on free electrons generated from n-doping in order to be conductive. Since TCOs are heavily doped and oxygen vacancies can be considered as ionized impurities too, this scattering mechanism is much more relevant than in semiconductors causing the mobility to reduce. GB scattering is a feature

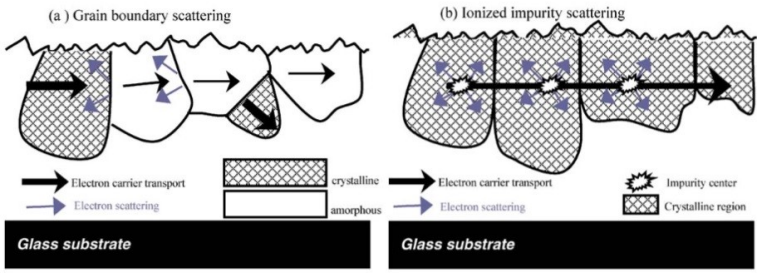

Figure 1.4: *Schematic representation of (a) GB scattering and (b) ionized impurity scattering. Adapted from [22]*

of polycrystalline films and it is still debated if it is the dominant mechanism in reducing the conductivity with respect to monocrystalline films. The orientation of the different grains creates distortion in the crystal lattice accommodated by defects. Such defects activate new energy levels within the band gap, acting as electron traps. As more electrons are trapped at the boundaries, a negative charge accumulates creating a potential barrier. Thus, electrons are repelled and the con-

ductivity decreases. In order to overcome this potential barrier, electrons must tunnel through it or be thermoionically emitted over it [15].

1.2.3 Optical properties

Due to the doping effect, the optical response of TCOs changes compared to the non-doped oxides. The first consequence is the Moss-Burstein (MB) effect (Fig. 1.5) [23]. It consists in an increase of the optical band gap, due to the partial filling of the conduction band (CB). Since the bottom of the CB is completely filled, photons with energy equal to the intial energy gap, E_g^0, will not be able to promote a transition, thus widening the transparency range.

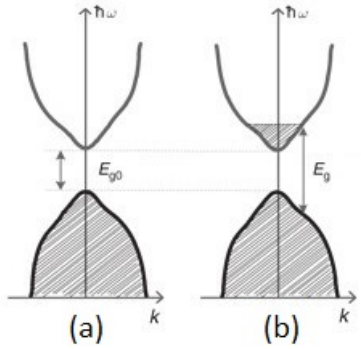

Figure 1.5: *(a) Schematic band structure of a metal oxide, with gap E_g^0. (b) Doping effect cause an increase in the optical band gap. Adapted from [24]*

The second consequence is the presence of the plasma frequency in the NIR regime. Generally, materials change behaviour around the plasma frequency, but not *exactly* at ω_p. As it can be seen in Fig. 1.6, at the plasma wavelength (λ_{PW}) it does not correspond an abrupt change in transmittance (T) or reflectance (R). On the contrary, there exist several characteristic wavelengths for each curve. λ_A expresses the absorption (A) peak, λ_M represents the minimum in reflection, λ_{RT} is the point where $T = R$. All these wavelengths don't have an analytical expression and their position change upon the material [15]. However, since those λ are really close to each other, it is possible to estimate the plasma wavelength just by performing simple optical characterization [25], [26].

1.2.4 Ta:TiO_2 as TCO

Titanium dioxide (TiO_2), or titania, is a widely studied transparent semiconductor that exhibits three different crystalline structures (see Fig. 1.7): the most stable form is rutile, while anatase and brookite are metastable [27]. The latter

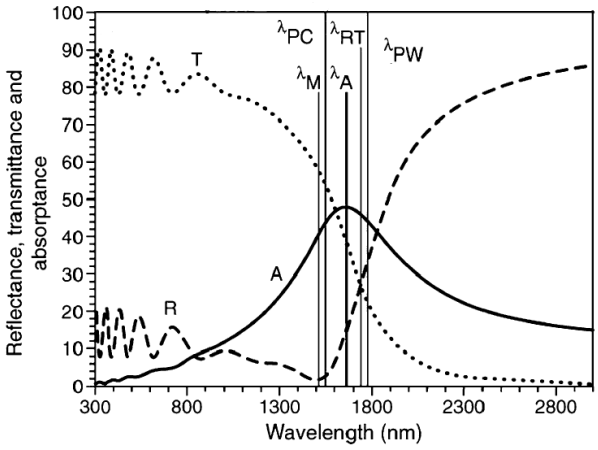

Figure 1.6: *The theoretical modeled reflectance, transmittance and absorptance. The carrier concentration was* 5×10^{20} cm^{-3}*, effective mass was* $0.4m_e$*, high-frequency permittivity was 4, and mobility was* 50 $cm^2V^{-1}s^{-1}$*. The film thickness was taken as 500 nm. Taken from [15].*

have an orthorhombic crystal structure, the others a tetragonal one. All three structures have a band gap above 3 eV, but mainly the anatase phase is interesting from an engineering point of view. In fact, anatase can be made conductive through oxygen vacancies and titanium interstitial atoms [28]. Anatase TiO_2 finds many applications as photoanode in dye-sensitized solar cells [29], [30] or in water splitting processes [31], [32].

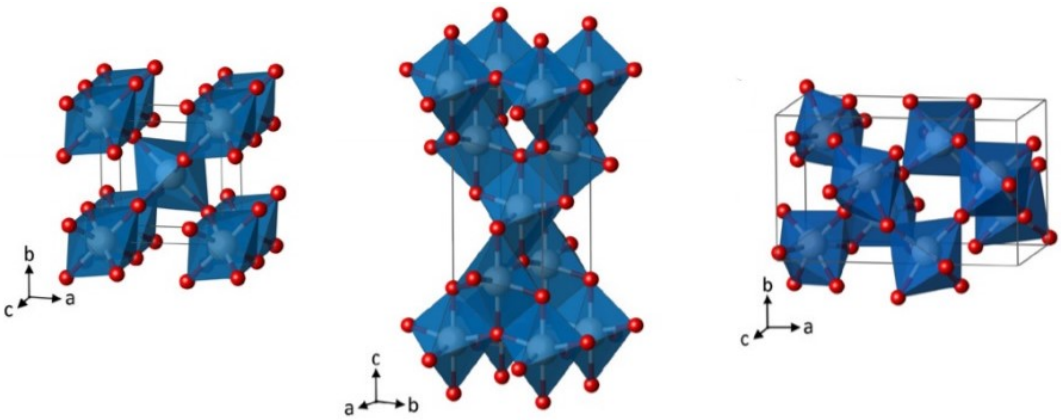

Figure 1.7: *Different crystal structure of titanium dioxide: rutile (left), anatase (center) and brookite (right). Adapted from [27].*

In order to further improve the electrical properties of anatase TiO_2, n-type doping can be performed. Ti belongs to the 4^{th} group in the periodic table, thus element from the 5^{th} can be exploited (Ta or Nb). The first study dates back to 2005, carried on by Hitosugi and his group [33]. They fabricated via pulsed laser

deposition (PLD) an epitaxial Nb-doped TiO_2 film onto a $SrTiO_3(100)$ substrate with outstanding electrical properties. The resistivity was 2.3×10^{-4} Ωcm, as low as ITO, for a doping concentration of 6%. Alongside the interesting Nb-doped, the same group explored the possibility of using Ta as doping element. In [34], an epitaxial Ta-doped TiO_2 film was produced via PLD. The optimum concentration was found to be 5% with a resistivity as low as 2.5×10^{-4} Ωcm. Even though Nb appears as a good candidate, Ta possesses two additional features that make it more promising: a higher solubility into the titania matrix and lower theoretically predicted electron effective mass [17]. Higher solubility means higher doping levels that can be used to tune ω_p and to increase the carrier concentration. A lower effective mass is desirable for the donor electrons because it allows higher mobility at higher doping levels.

Hitosugi's group explored the deposition of V-group doped TiO_2 on amorphous substrate like glass, since epitaxial growth on crystalline-oriented substrates is not a scalable process. The as-deposited film resulted amorphous, thus a thermal treatment in reducing atmosphere was necessary in order to promote crystallization. Such polycrystalline films show slightly worse electrical properties in comparison with the epitaxial ones, as expected since GB scattering is activated by the considerable amount of interfaces.

An exhaustive study of Ta-doped TiO_2 (TaTO) was carried on by Mazzolini in our laboratory [17]–[20]. Thermal treatments done in vacuum at 550°C gave in return conductive films, while air-annealed samples turned out to be insulating, meaning that oxygen vacancies play an important role. The main results found by Mazzolini are reported below:

(i) the optimal deposition condition for TaTO with 5% level doping: TaTO films were deposited via PLD in a background pressure of pure oxygen at 1,25 Pa. The resistivity was found to be 5×10^{-4} Ωcm, the carrier concentration $n = 8 \times 10^{20}$ cm^{-3} and mobility $\mu = 9.9$ $cm^2 V^{-1} s^{-1}$. Moreover, by increasing the pressure up to 2.25 Pa a deterioration of the electrical properties was observed (see Fig. 1.8), clear evidence that oxygen vacancies play an important role in the conduction of TaTO films.

(ii) The estimate of a plausible value for the TaTO plasma frequency: firstly Tauc plots were performed in order to calculate the band gap [35], because it differs from pure TiO_2 due to the MB effect. To do so, $(\alpha h\nu)^{1/r}$ $(r = 0.5)$ was plotted against the photon energy $h\nu$; the resulting trend had a linear regime, from which can be extrapolated the band gap. Afterwards, if the shift are plotted against $n^{2/3}$ where n is the carrier density, another straight line is obtained (see Fig. 1.9a). The slope is proportional to the effective

mass whose value was approximated to $2.9m_e$ (m_e is the electron mass). By knowing the permittivity of TiO_2, it was possible to assess $\lambda_p \sim 4160$ nm.

(iii) The observation of a trend regarding the material's carrier density and Raman spectra: a linear correlation was found between the carrier concentration n and the position of the $E_g(1)$ peak of pure TiO_2 (Fig. 1.9b). For increasing values of n, a blue-shift of the peak was observed, regardless of dopant concentration or doping material [18].

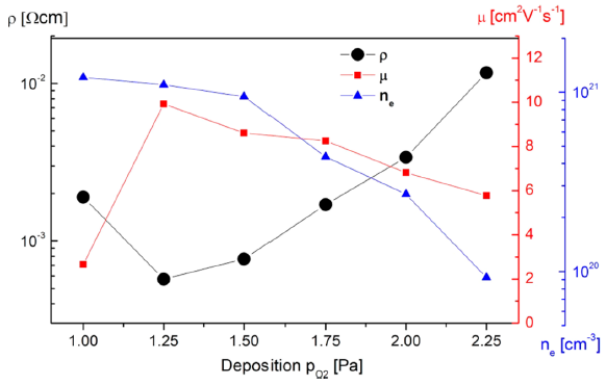

Figure 1.8: *Deterioration of the electrical properties of Ta(5%):TiO_2 films deposited at differnt oxygen preussure. Taken from [17]*

The research on TaTO was continued by Ornago [7] and Gaetani [8]. Ornago had to found again the optimal deposition condition for Ta(5%):TiO_2 because the laser wavelength in our laboratory was changed. He found that the best electrical properties were achieved at 1 Pa in pure oxygen atmosphere with a laser fluence of 2.2 J/cm^2. He studied the effect of higher oxygen pressure as well. The results confirmed what found by Mazzolini *et. al.* in [17]: increasing the pressure caused a worsening in the electrical properties and an increasing in the transmittance spectrum.

The effect of mixed background atmosphere, with composition of Ar:O_2=5:1 was inspected too, always on Ta(5%):TiO_2 [7], [8]. The final objective of this study was to obtain conductive porous films, since the pressure can be increased maintaining a low content of oxygen. Up to 4 Pa, the films kept the compact structure and electrical properties were worse with respect the optimal deposition condition of 1 Pa in pure oxygen. From 6 Pa to 15 Pa in mixed atmosphere, the porous morphology arose. Only the 6 Pa and 8 Pa sample underwent crystallization after the vacuum annealing, while the sample deposited at higher pressure did not. In plane electrical characterization gave unreliable result on the porous sample. Cross plane measurement should be performed in order to obtain a truthful result.

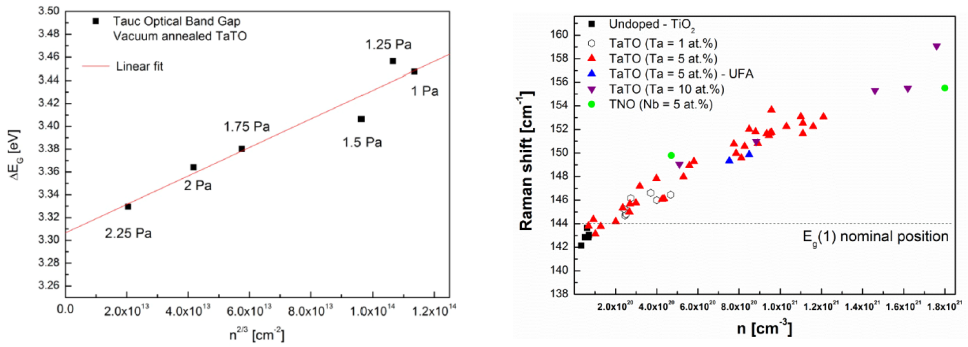

(a) *(b)*

Figure 1.9: *(a) Tauc optical band gap as a function of $n^{2/3}$ for vacuum annealed TaTO films deposited at different oxygen partial pressures. Taken from [17]. (b) $E_g(1)$ position against carrier density. Taken from [19].*

1.3 Metamaterials

When approaching the term *metamaterial* (from Greek $\mu\varepsilon\tau\alpha$, beyond), a rigorous and unambiguous definition is still lacking. A first one could be "an arrangement of artificial structural elements, designed to achieve advantageous and unusual electromagnetic properties" [36]. However, such definition is too general, thus many leading experts in the field prefer to add comments as "properties unlike any naturally occurring substance" or "not observed in nature". Nevertheless, to establish if a property is naturally present in a material would require long researches and time. Hence, a good definition is the one proposed by Cai & Shalaev in [36]: "a metamaterial is an artificially structured material which attains its properties from the unit structure rather than the constituent materials. A metamaterial has an

Figure 1.10: *Architecture of Smith et al. [37] for the first NIM. The red squares represent the resonators, deposited on fiberglass, and the vertical stripes running through the squares are the wires. Taken from [37].*

inhomogeneity scale that is much smaller than the wavelength of interest, and its

electromagnetic response is expressed in terms of homogenized material parameters". As it can be understood from the last definition, metamaterials are made up by using at least two different materials, usually a metal (or a material with metallic behaviour, like a TCO) and a dielectric. Moreover, the requirement of a sub-wavelength structure is crucial in order to treat the metamaterial as a uniform material, with effective properties.

The interest for metamaterials started in 1960s, when the russian physicist Victor Veselago supposed the existence of a material with both negative dielectric permittivity and magnetic permeability [38]. The latter is achievable only with metamaterials, whereas the former is a common property of metals. Such combination can generate a metamaterial with negative refractive index (NIM), which can go beyond the diffraction limit of light. Therefore, such metamaterials can be used as a super lens [39] or sub-wavelength waveguides. In 2000, Smith *et al.* [40] demonstrated Velesago's prediction with a periodic array of copper split-ring resonators and wires mounted on interlocking sheets of fiberglass circuit board (see Fig. 1.10).

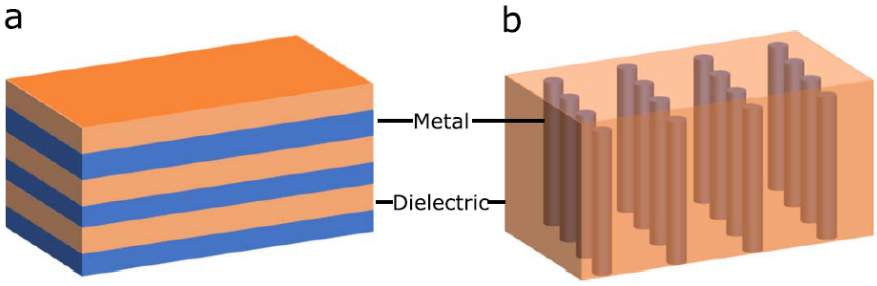

Figure 1.11: *(a) Metal-dielectric layered structure and (b) nanowire arrays. Taken from [41].*

Nevertheless, the realization of simultaneously negative ε_r and μ_r is difficult, since the majority of materials are non-magnetic. Hence, scientists have focused on a metamaterials sub-class: hyperbolic metamaterials (HMMs). HMMs have advantages of relative ease of fabrication at optical frequencies, broadband non-resonant and 3D bulk responses, flexible wavelength tunability and simple geometries [42]. The simplest and most studied geometries are the *layered structures* and the *nanowire arrays* (see Fig. 1.11). For the purpose of this thesis work, only the layered structure will be analyzed in detailed, but it is important to point out that other configurations exist, such as the *multilayer fishnet* or the *nanopyramids arrays* (see Fig. 1.12) [43].

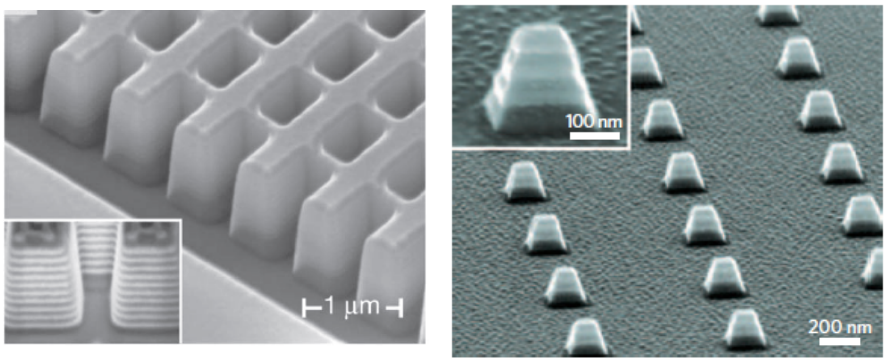

(a) *(b)*

Figure 1.12: *(a) Multilayers fishnet structure. Taken from [41]. Nanopyramids arrays structure. Taken from [43].*

1.3.1 Hyperbolic dispersion and effective medium theory

In the layered architecture, the unit cell or period is composed by one layer of metallic material, with permittivity ε_m and one layer of dielectric, with permittivity ε_d. If the thickness of the unit cell is much smaller than the wavelength of the EM radiation, then the responses of the single components are outweighed by an average response of the system as a whole. Thus, "effective" properties must be defined, and cannot be the mere sum of the original ones. The most used models used to describe the EM response are the Bruggeman's effective medium theory (EMT) and the Maxwell-Garnett theory (MGT). The former is used when the materials are present in a similar ratio, the latter is used when one material can be seen as a "host" and the other is in the form of inclusion or dispersed particles [36]. In the case of a layered structure, the EMT is the correct one to use. It is evident the anisotropy of such system, hence the dielectric permittivity will be described by a tensor:

$$\hat{\varepsilon} = \begin{bmatrix} \varepsilon_{xx} & 0 & 0 \\ 0 & \varepsilon_{yy} & 0 \\ 0 & 0 & \varepsilon_{zz} \end{bmatrix} = \begin{bmatrix} \varepsilon_{\parallel} & 0 & 0 \\ 0 & \varepsilon_{\parallel} & 0 \\ 0 & 0 & \varepsilon_{\perp} \end{bmatrix} \tag{1.9}$$

The z axis is the one passing through the layers, namely the anisotropic axis, thus the subscript $\perp$ is referred to it, whereas the subscripts $\parallel$ are referred to the plane layers. EMT provides the equation for $\varepsilon_{\parallel}$ and $\varepsilon_{\perp}$, starting from ε_m, ε_d and their corresponding thicknesses d_m and d_d (p is the filling metal content):

$$\varepsilon_{\parallel} = p\varepsilon_m + (1-p)\varepsilon_d \qquad \frac{1}{\varepsilon_{\perp}} = \frac{p}{\varepsilon_m} + \frac{1-p}{\varepsilon_d} \qquad p = \frac{d_m}{d_m + d_d} \tag{1.10}$$

In order to analyze wave propagation inside anisotropic media, Maxwell's equations have to be solved, keeping in mind the different permittivity in every direction. The final and important result is the dispersion relation for TM modes:

$$\frac{k_x^2 + k_y^2}{\varepsilon_\perp} + \frac{k_z^2}{\varepsilon_\parallel} = \frac{\omega^2}{c^2} \tag{1.11}$$

Since the permittivity function (of both metal and dielectric component) changes sign as a function of the frequency, it is possible that either $\varepsilon_\perp$ or $\varepsilon_\parallel$ are negative. As a consequence, from an algebric point of view, Equation 1.11 becomes that of an hyperbola, hence the name *hyperbolic* metamaterials. There could exist two spectral range in which the above condition is met: when $\varepsilon_\parallel > 0$ and $\varepsilon_\perp < 0$, the HMM is called *Type I* or hyperbolic dielectric (referring to its behavior in the xy plane); in the opposite situation, $\varepsilon_\parallel < 0$ and $\varepsilon_\perp > 0$, the HMM is a *Type II* [44] (see Fig. 1.13).

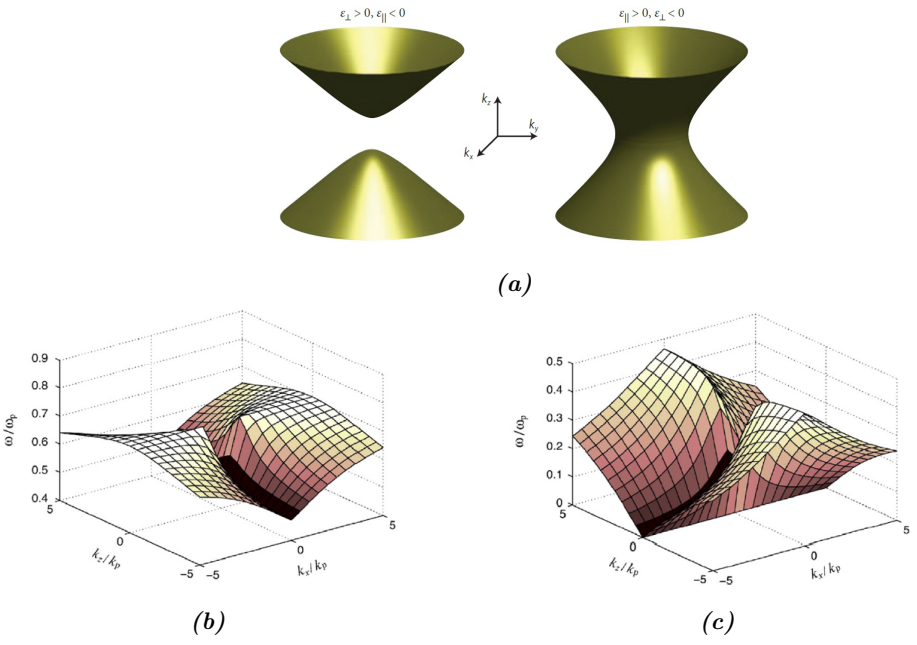

Figure 1.13: *Different representations of isofrequency surfaces: on the left, Type I is depicted, on the right Type II. (a) Adapted from [43], (b) and (c) adapted from [44].*

The hyperbolic dispersion indicates that HMMs support the propagation of electromagnetic waves with large wavevectors known as high-k modes, which are typically evanescent in conventional isotropic media, such as air and glass. Such feature will be exploited to overcome the diffraction limit of conventional lenses, in order to further increase the resolution [44].

Even though EMT provides great results, it is not enough to fully explain the

HMMs behaviour. Firstly, the wavelength of high-k modes, $\frac{2\pi}{k}$, will eventually become smaller than the layer thickness, hence EMT is not valid anymore [45]. Moreover, no further physical insight is given by EMT, other than associate the high-k modes to bulk propagating waves. Since metal-dielectric interfaces are present, it is straightforward to think a plasmonic nature of such modes, hence they take the name of *volume plasmon polaritons* (VPPs). Indeed, Zhukovsky *et al.* [45] proved that in a layered HMM, the VPPs originate from coupling of SPPs in the individual metal layers by virtue of the Bloch theorem. They concluded that high-k waves in HMMs can be physically understood as "Bloch VPPs", and can be seen as a distinct type of plasmonic excitations (for further analyses, see [45]).

1.3.2 Metal-dielectric multilayers

The most studied HMMs in literature implement Au or Ag as metallic component, due to their optimal electrical properties among metals [46]–[51]. Fulfill the impedance matching, $|\varepsilon_m| \sim |\varepsilon_d|$, is crucial in order to generate the SPPs which couple with each other into Bloch VPPs, sustaining the high-k modes inside the metamaterial [41]. Hence, Al_2O_3 and TiO_2 were selected as dielectric component, since the amplitude of their dielectric functions is comparable with the one of gold and silver in the UV-Vis operation range. Different combination of geometry, layers thicknesses, metal filling content were tried to obtain the desired application .

Approaching the NIR, it is well known that Au and Ag become too lossy due to the intraband transition. Therefore, it emerges the need of new metallic component in order to create a metamaterial that can operate in the infrared regime. Research focuses on the dielectric component too, since the impedance matching condition must be always achieved.

1.3.3 TCO multilayers

Trilayer TCO-metal-TCO structures were implemented in order to increase the electrical performances without affecting too much the transparency in the Vis region. The metallic layer has to be very thin in order to not hinder the transmissivity, but at the same time a continuous films is necessary to increase the electrical properties. ITO and AZO have been object of deep study since they possess the best properties among all the TCOs [52]–[58]. For the inter metallic layer, Ag and Au were selected, since they exhibit the lowest resistivity. As expected, resistivity, carrier density and mobility improve for thicker inter metallic layer, while transmittance reduces. Such trend was also found for novel trilayers

structures of (Nb-Ta):TiO_2-Cu-(Nb-Ta):TiO_2 and ITO-TiN-ITO [59], [60]. Moreover, the crossover wavelength (wavelength at which the trilayers' dielectric function changes sign from negative to positive) shifts towards shorter wavelength for thicker metallic inter layer. Such behaviour was reported in the ITO-TiN-ITO trilayers structure as well. This is a first example of how the plasma frequency can be tailored with the geometry/structure.

TCO-dielectric multilayers as HMM in the infrared are an emerging field. Not many examples are reported in literature, mainly relying on AZO/ZnO structure [2]–[5]. To the extent of the writer knowledge, combination of ITO and its oxide, In_2O_3, in order to obtain a HMM has been poorly investigated [6]. In this paper, the multilayers were composed by 16 layers of 10 nm and displayed both type I (between 1.13 μm and 1.58 μm) and type II (for wavelength higher than 1.61 μm) hyperbolic dispersion relation. Naik *et al.* [2] were the first to demonstrate that AZO/ZnO multilayers display the hyperbolic dispersion relation in the infrared range, between 1.84 μm and 2.4 μm; the structure was composed of 16 layers, each one 60 nm thick. Kelly *et. al.* [5] studied the influence of geometrical parameters on the plasmonic response of AZO/ZnO multilayers. They found four important results:

- ω_p increases for increasing number of periods (AZO layer + ZnO layer). Even though the metal filling ratio p (metal percentage in the period) remains the same (see Eq. 1.10), the thicker samples increase the transfer ability of surface atoms in the crystal, increasing the Al concentration.

- ω_p decreases for increasing substrate temperature (T>150°C), due to segregation of Al_2O_3 at the grain boundaries.

- ω_p decreases for increasing AZO content in the period.

- ω_p decreases for increasing period thickness (at constant metal filling ratio p and constant total thickness).

The third result is not discussed in detailed and it is quite counterintuitive, since increasing the metal filling content p should result in a more metallic behaviour of the multilayers (see Eq. 1.10), hence a higher plasma frequency. Such result can be an indication of how geometry can prevail over the properties of single materials. In section 4.3 further details can be found.

A complete comprehension of geometrical parameters affecting the optical, electrical and plasmonic properties of multilayers is still lacking. This thesis work aims to provide a partial explanation of the influence of period thickness on the aforementioned properties of TaTO-only multilayers.

1.4 Applications

HMMs are appealing for several applications, relying on their unique property, namely the hyperbolic dispersion relation. The fact that high-k modes are sustained inside the material open the possibility to novel and exotic application, not realizable before.

One of the first studied phenomena was negative refraction for TM polarized modes. In an isotropic media, the isofrequency surface is a sphere, thus the wavevector **k** and the Poynting vector **S** are parallel (see Fig. 1.14 on the left). In a common anisotropic media, generally there is a non-zero angle between **k** and the Poynting vector **S**, due to the birefringence of the crystal and the incidence direction (see Fig. 1.14 in middle). In an HMM, if the angle increase to the point where the projections of **k** and **S** along certain orientations are opposite to each other, then a NIM-like behavior is expected [36], as depicted in Fig. 1.14 on the right.

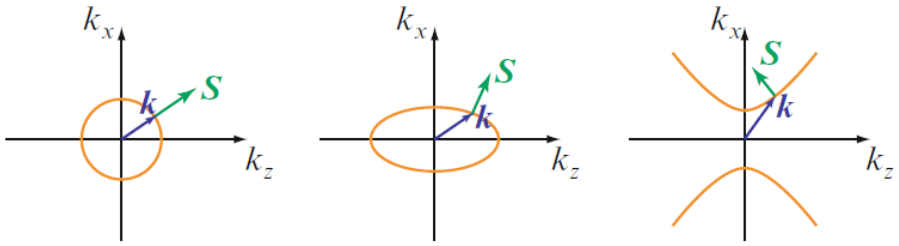

Figure 1.14: *Isofrequency surfaces and Poynting vector for isotropic crystal with $\varepsilon_x = \varepsilon_z$ (left), anisotropic crystal with ε_x, $\varepsilon_z > 0$ (middle), HMM (right). Taken from [36].*

The signs of k_z and S_z become opposite due to the strong curvature of the hyperbola. This opposite directionality leads to a optical negative refraction. Optical negative refraction can be exploited to obtain partial focusing [61], as shown in Fig. 1.15a, hence HMMs slabs have great potential to become lenses. Another interesting application for light-beam-manipulation is angular optical transparency [62]. Photonic crystals exhibit such properties as well, but the relatively large transparency window and complex architecture limit their practical implementations. On the contrary, HMMs can achieve narrow optical transparency filtering effect, due to the topological transition of the isofrequency surface, from elliptical to hyperbolic topology [42]. Close to the point of topological transition of the isofrequency surface (from elliptical to hyperbolic), the special dispersion topology leads to a narrow optical angle filtering effect, hence transmission of the incident light beam is allowed only in the normal direction (see Fig. 1.15b).

In addition, HMMs have promising potential in high resolution imaging. Low-k vector components of the spatial spectrum encode large geometric features, while

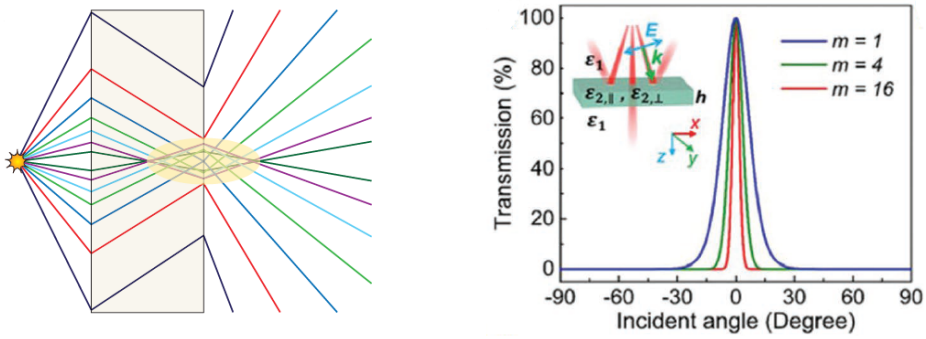

(a) *(b)*

Figure 1.15: *(a) Partial refocusing by a HMM. Taken from [43]. (b) Narrow optical filtering. Taken from [62].*

high-k vectors describe finer details [44]. In an isotropic media, characterized by a spherical isofrequency surface, modes with wavevector exceeding such sphere are forbidden, thus called evanescent waves. This phenomena, called diffraction limit, correspond to a loss of information. HMMs naturally sustain high-k modes without resonant mechanisms, making them ideal candidate to improve the resolution [63]. Although the multilayered HMMs could transmit a sub-wavelength image, the structure could not magnify it, neither could the output image be manipulated by a conventional optical lens.

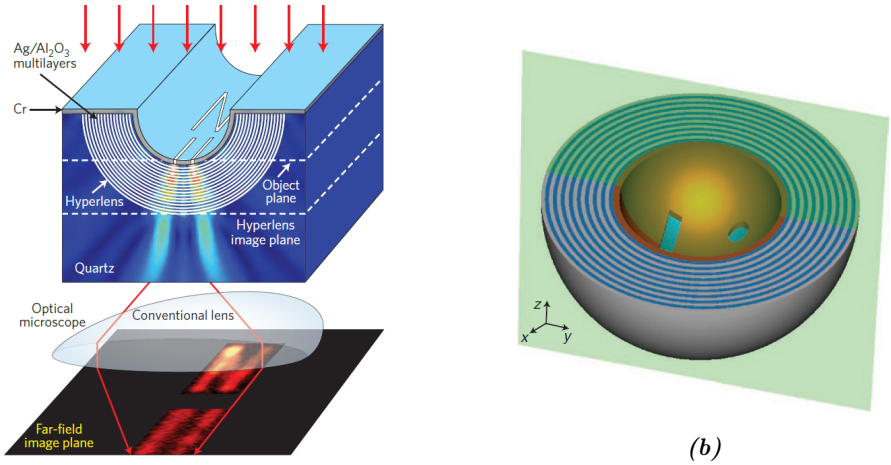

(a) *(b)*

Figure 1.16: *(a) cylindrical hyperlens, by Liu et al. [46]. (b) spherical hyperlens by Rho et al. [49].*

To overcome these problems, a *hyperlens* was proposed. The first implementation was optimized for UV light [46], consisting of 16 layer (35 nm each) of Ag and alumina (see Fig. 1.16a). In the cylindrical configuration, the image is trans-

ferred along the radial direction and gradually magnified. Once the diffraction limit is overcome, conventional lenses can be used to further resolve the image. The resolution is limited by the operation wavelength and the device geometry: $\Delta \propto (R_{inner}/R_{outer})\lambda$. An additional drawback of cylindrical hyperlens is the limited magnification to only one dimension, making it impractical for full imaging applications [42]. A new route to overcome these drawbacks is to use instead a spherical hyperlens (see Fig. 1.16b) with magnification directions covering the whole 2D plane. Ag was alternated to Ti_3O_5 to obtain super-resolution in the visible range. Despite the great advantage of 2D magnification, the performance of the spherical hyperlens is limited by defects in fabrication, which causes distortion in the subsequent far-field image.

The great opportunity given by HMMs to overcome diffraction limit can be exploited as well in high resolution nanolitography [42], [44]. Photolitography has been widely employed by the integrated circuit industries and semiconductor manufacturing due to the high resolution and cost effectiveness. Although ultraviolet light or X-ray can be used to improve the resolution, the instrumental complexity and cost are not bearable. High resolution can be achieved by interference photolitography using HMMs [64]. Xu *et al.* [65] developed a multilayer HMM consisting of Ag (20 nm) and SiO_2 (30 nm) that was able to produce feature size of 40 nm in the photoresist, from a wavelength of 442 nm. However, energy loss happens in the HMM leading to an electric field of limited intensity interacting with the photoresist, hence long exposure time are required.

Another possible application is spontaneous emission (SE) enhancement, desirable in several field such as solid state lighting [66], [67], optical communications [68] or quantum computing with single photon sources [69], [70]. SE is determined by the Fermi's golden rule:

$$\Gamma_{fi} = \frac{2\pi}{\hbar} \left|\langle f, 1_k | H_{int} | i, 0_k \rangle\right|^2 \rho(\hbar\omega_k) \tag{1.12}$$

where $\langle i, 0_k|$ is the initial state, $|f, 1_k\rangle$ is the final state, H_{int} represents the hamiltonian interaction and ρ is the photon density of state (PDOS) at transistion frequency $\omega_{fi} = \omega_k$, namely the number of available electromagnetic modes for the emitter to radiate, per unit frequency and unit volume. By changing the surrounding, it is possible to modify the PDOS, thus increasing the SE. This concept was first studied by Purcell [71] who compared the SE rate in a cavity with respect to free space. SE can be achieved via plasmonic resonance as well, avoiding the need of cavities. Nevertheless, both these two methods are resonant processes related to ω_k, thus limiting the number of emission modes. HMMs can overcome this drawback and can realize a broadband enhancement SE [72]. Since hyperbolic isofrequency surface is open, a much larger PDOS is achievable, hence

a larger number of modes can be generated. Many are the examples reported in literature [47], [48], [50], [73].

Sensing can take benefit from HMMs too, since are highly sensitive to refractive index changes caused by the surrounding environment, from visible to IR [41], [74], [75]. Sreekanth *et al.* proposed a structure with HMM covered with a two-dimensional nanohole grating and microfluidic channel on it. Such device is able to detect small molecules at picomole concentrations. Subsurface sensing can be realized as well [76]. HMMs in the IR (semiconductors or TCO) can be employed for non-invasve sensing. Quality control in integrated circuits (ICs) or microelectromechanical devices (MEMs) can be implemented since silicon is transparent to IR wavelengths. Therefore, cracks or defects can be detected through the scattering and diffraction of IR light.

1.5 Objectives of this thesis work

This thesis work aim to explore the possibility and performance of Ta:TiO_2 as metamaterial in the NIR and understand the geometry dependence on the optical, electrical and plasmonic properties. The starting point was given by Gaetani [8] in his TaTO-only multilayer. To the extent of the writer knowledge, no one as ever attempt to produce a metamaterial by using only one material. Such opportunity is possible because by changing the deposition pressure, a conductive or non-conductive film can be obtained. This could be helpful in reducing the losses and to have a better continuity at the interface. In order to do so, several experiments have been performed:

- A preliminary studied have been conducted on Ta(10%):TiO_2: ultrathin (20 nm, 10 nm, 5 nm) layers were deposited at 1 Pa in pure oxygen on glass substrate to evaluate their properties in the perspective of realizing a multilayer structure. The same layers were deposited on stoichiometric titania substrate as well. In this case, the focus was on the enhancement of the electrical properties for future applications as transparent electrodes in solar cells.

- Higher deposition pressure in both pure oxygen and mixed atmosphere were investigated on Ta(5%):TiO_2 and Ta(10%):TiO_2 (3 Pa and 6 Pa in pure oxygen and 3 Pa in Ar:O_2=5:1) These films were expectd to be non-conductive, hence they could be use in the metamaterial.

- Then, the multilayers were deposited and a full characterization were performed. Layers deposited at 1 Pa in pure oxygen were alternated to layers deposited at higher pressure. Both multilayer of Ta(5%):TiO_2 and Ta(10%):TiO_2 will be produced to observed the differences in their optical and electrical

properties. Two main architecture were produced: in the first one, each layer had the same thickness (20 nm or 10 nm), hence the metallic filling ratio was $p = 0.5$; in the second one, the filling ratio was changed to $p = 0.33$ (dielectric layers had double thickness with respect the conductive ones) and $p = 0.66$ (conductive layers had double thickness with respect the dielectric ones).

All the sample are deposited by PLD, using a nanosecond pulsed laser (Nd:YAG second harmonic, $\lambda = 532$ nm. Structural, morphological, electrical and optical characterization were performed using scanning electron microscopy (SEM), Raman spectroscopy, four-point probe electrical measurements and UV/Vis/NIR spectrophotometry.

Chapter 2

Experimental techniques

2.1 Pulsed Laser Deposition

Pulsed Laser Deposition (PLD) is a physical vapour deposition (PVD) technique employed for the deposition of thin films and multilayers. The deposition process happens inside a vacuum chamber; a monochromatic pulsed laser beam impinges on the target material, generating a *plasma plume* orthogonal to the target surface. The ionized species inside the plume travel to the substrate, which is located in front of the target at a precise distance, and the film growth starts. It is a versatile technique, since it allows to deposit several classes of materials, such as metals, ceramics, oxides, semiconductors, polymers and even biomolecules [77]. Moreover, it is possible to deposit films with the same chemical composition of the target, enabling the deposition of materials with a high complex stoichiometry. For example, PLD is the most suitable technology for the production of cuprate high-temperature-superconductor $YBa_2Cu_3O_7$. Such possibility originates from the non-thermal nature of the ablation process. In fact the energy absorbed by the target material is much higher than that needed for evaporation, hence the vaporization flux is independent on the vapour pressure of the target's constituents [78]. Naturally, the portion of ablated material is very small and it corresponds to the laser spot dimension. However, PLD presents some drawbacks too. First, the homogeneous deposition area is pretty small ($\sim cm^2$), thus limiting this technique to a laboratory scale. In order to partially overcome such problem, a roto-translation of the substrate and target can be implemented to enlarge the deposition area. Secondly, the formation of micrometric particles, called *droplets*, could be included in the film, causing inhomogeneity in the film itself; lastly, impurities in the target might be present and crystallographic defects in the film can arise due to the particles of high kinetic energy impinging onto the substrate [79]. The duration of the laser pulse can span from nanoseconds down to femtoseconds and the main

difference is in the physical mechanism of the ablation process [77].

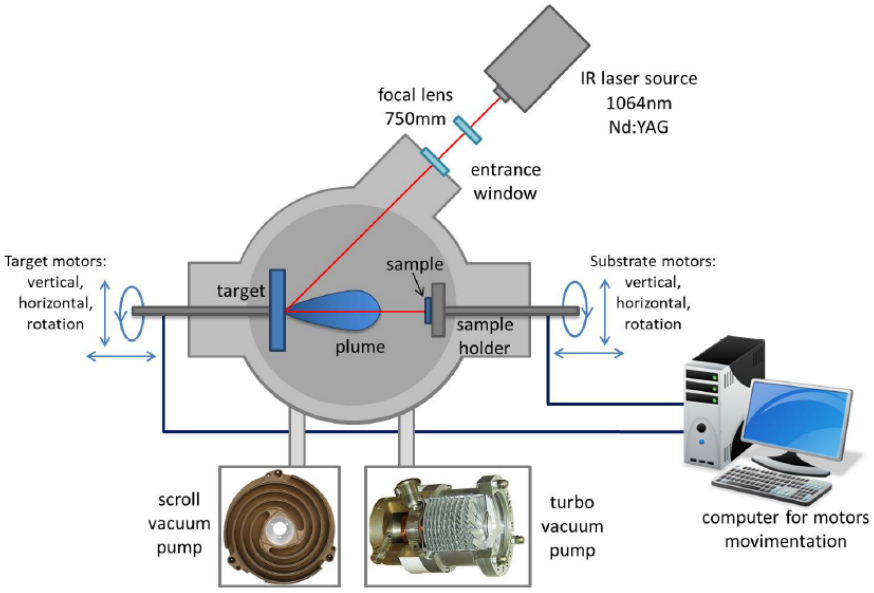

Figure 2.1: *Schematic representation of a PLD apparatus. Taken from [80].*

The PLD apparatus can be seen in Fig. 2.1. It consists of a vacuum chamber (usually made of stainless steel), in which are present both the target and substrate, facing each other. The proper degree of vacuum is obtained by a pumping system: a primary pump (scroll pump) is able to reach a pressure of the order of few pascal. Successively, a turbomolecular pump is used to reach the desired level of vacuum, around 10^{-5} Pa. The laser beam is located outside the chamber, hence an optical path is needed in order to let it enters in, usually with an incident angle between 40°-50° with respect to the target surface. In the case of nanosecond pulses (the ones used to deposit all the samples in this thesis work), the ablation process is mainly thermal since the bulk electrons have the time to transfer the absorbed energy to the phonons, via electron-phonon scattering (process of the order of picoseconds) [77]. The energy density of the laser, called laser fluence (J/cm^2), has to reach the *ablation treshold* in order to ablate the material. Laser fluence can be adjusted by modifying the optical path of the laser before entering into the chamber. As soon as the laser pulse hits the target, an ablation plasma called *plasma plume* is ejected orthogonal to the target surface. Since the plume expansion starts before the end of the pulse, it is able to absorb some energy, making the plasma more energetic and ionized; hence, the ablated particles can cluster inside the plume, before reaching the substrate. An additional feature is the possibility to inlet inert or reactive gasses in the chamber (not shown in Fig. 2.1). The presence of a background gas strongly influences the deposition

condition, affecting the film properties:

- at low pressure, the particles travel almost collisionless, thus they arrive at the substrate highly energetic and compact films are produced;
- by increasing the pressure, the ablated particles lose energy due to collision with the gas molecules, cluster formation inside the plume is favoured, thus porous film are obtained. Furthermore, the plasma plume results more confined and the *shock front* appears clearer [77].

In the presence of reactive gasses like oxygen, chemical reaction with the ablated species can happen inside the plume. A classification on the deposition regimes can be made by introducing the dimensionless parameter L. It is defined as the ratio between the target-substrate distance d_{ts} and the plasma plume lenght l_p. Therefore, three regime can be defined:

- $L < 1$: the substrate is situated *in plume*. In this situation, the formation of clusters in the plasma plume is reduced and the particles arrive with high energy at the substrate, thus compact film are expected to form. Atoms can reach energies up to tens of eV.
- $L \sim 1$: the substrate is *at the plume edge*. The substrate is positioned at the end of the plume, hence the ablated species have more time to interact with each other and the reactive gas. As a consequence, the clusters arrive at the substrate with lower energy with respect the previous scenario.
- $L > 1$: the substrate is located *outside the plume*. The conditions just described above are enhanced, thus more clustering with even lower energy is expected, generating nanoporous films.

The PLD apparatus used in this thesis work exploits a Nd:YAG nanosecond pulsed laser, with second harmonic at $\lambda = 532\ nm$, repetition rate $f_p = 10\ Hz$ and pulse duration $\sim 6\ ns$. The target-substrate distance was kept fixed, $d_{ts} = 5\ cm$, whereas different laser fluence and background pressure were employed (more details are provided in the results chapters). As substrates, Si (100) and soda-lime glass were used. The samples were obtained by ablating Ta_2O_5:TiO_2 with molar ratios 0.025:0.975 and 0.05:0.95, corresponding to a Ta atomic content of 5% and 10% respectively. The vacuum chamber was designed by our laboratory and uses an Agilent TriScroll 600 as primary pump and a Pfeiffer Vacuum TMU 521 turbomolecular pump. The gasses pressure was controlled by a MKS Multi Gas Controller 647C.

In order to deposit my sample, a test specimen was deposited for 15 min. Then, form cross section SEM analysis the thickness was measured and the deposition rate was calculated in order to deposited the sample with nominal thickness.

2.2 Scanning Electron Microscopy

Scanning Electron Microscopy (SEM) was employed to assess the morphology of the deposited films. This characterization technique is able to acquire images of electrically conductive samples with spatial lateral resolution down to few nanometers. A schematic representation of the whole apparatus is depicted in Fig 2.2a. Monochromatic electrons are emitted by an electron-gun, produced via thermoionic effect or field emission. Successively, they are accelerated by a voltage that can range between 200V-30kV, before hitting the sample. The electron beam is collimated by the use of electromagnetic lenses, in order to reduce as much as possible the diffraction limit and consequently the lateral resolution. The whole apparatus works in vacuum to avoid collision between electrons and air molecules.

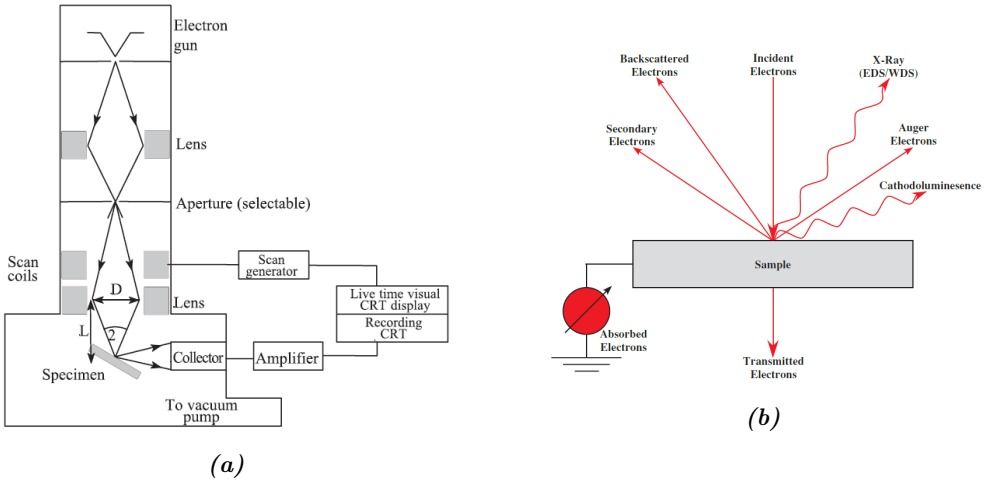

Figure 2.2: *(a) Schematic representation of the SEM apparatus. Taken from [81]. (b) Possible signals emitted from the sample after the interaction with the electron beam. Taken from [82].*

After the beam hits the sample, different signals are generated (see Fig. 2.2b) and distinct detectors are used to collect each one of them. Backscattered electrons and secondary electrons are the most relevant for imaging purpose. The former are able to discern between compact or porous structure, whereas the latter give the sense of depth, providing morphological and topographic information [82]. In this work, a Field Emission Zeiss SEM Supra 40 was used to collect the cross section images of the samples and all the pictures shown in this work were obtain by using secondary electrons. The voltage bias was set at 5 kV for all the pictures shown in the following chapters.

2.3 Raman spectroscopy

Raman spectroscopy is one of the most important vibrational spectroscopy techniques. It is based on the inelastic scattering of monochromatic light with a molecule or a solid, and it can give information regarding chemical bonds, different material phases and crystalline structure [81]. Atoms in crystals vibrate due thermal energy around their equilibrium position. The collective oscillations of atoms generate lattice waves, described as quantum independent harmonic oscillators. The lattice waves are known as normal modes and the quantum of energy is called phonon. When the monochromatic beam hits the crystal, the system (photon + crystal) is excited to a virtual state. The word "virtual" is used to indicate that the system is in a non-stationary state [83] (see Fig. 2.3). Successively, three different processes can occur:

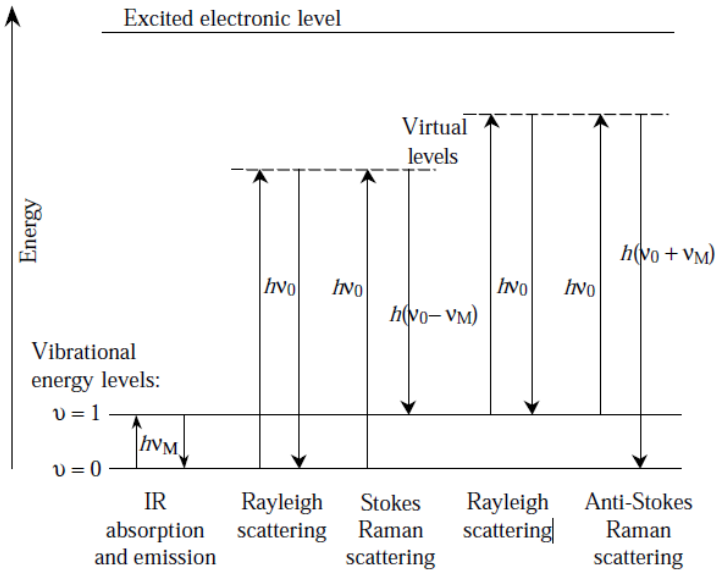

Figure 2.3: *Possible Raman scattering processes. ν_0 is the incoming frequency of the photon, whereas $\hbar\nu_M$ is the energy of the vibrational state. Taken from [83].*

- **Rayleigh elastic scattering**: the crystal relaxes to the initial vibrational state, emitting a photon with the same energy.
- **Stokes inelastic scattering**: the lattice de-excites into a higher vibrational state with respect to the initial one (which means that a phonon has been created), emitting a photon with lower energy.
- **Anti-Stokes inelastic scattering**: with lower probability, the lattice returns to a lower vibrational state with respect to the starting one (which

means that a phonon has been annihilated), emitting a photon with higher energy. Such process happens only if the crystal is initially at a higher energy state when absorbs the incoming photon. The probability that the crystal is in a higher vibrational state as a starting level scales with the temperature.

Stokes transitions are more frequent with respect the Anti-Stokes ones, therefore show more intense signals and are exploited for the Raman spectroscopy. Due to energy and momentum conservation, only phonons at the center of the Brillouin zone can give Raman signal. In addition, a vibrational mode is Raman-active only if there is a change in one component of the tensor of the polarizability α. It is important to note that the outcome of Raman spectroscopy are the vibrational frequencies proper of the crystal or the molecule, hence Raman spectroscopy acts as a fingerprint for each material. Disorder, defects and quantum confinement can broader the Raman peaks (thus giving additional information on the crystal structure) and possible peak-shifts can arise.

In this thesis work, Raman spectroscopy has been used to assess if the samples had been crystallized after the thermal treatment. The instrument at the laboratory is a Renishaw InVia micro Raman spectrometer, equipped with an optical microscope. The light wavelength was set to $\lambda = 514\ nm$, coming from a Argon ion laser; the laser power was 0,13 mW to avoid any modification in the samples.

2.4 Thermal treatments

The samples obtained via PLD resulted amorphous, hence they were exposed to thermal treatment in order to induce crystallization. To preserve the oxygen-related defect chemistry, which affects carrier density of the Ta:TiO_2 specimens, vacuum annealing was performed. The apparatus is composed by a home-made stainless steel vacuum chamber, the correlated vacuum system, a heating system placed inside the chamber and an electronic control to set the thermal treatment (ramps and temperature). Vacuum annealing was performed at 5.5×10^{-5} mbar and 550°C, reached with a ramp of 10°C/min. Dwell time was set to 1 hour. Cooling was obtained with the same ramp, but at the end it slowed down.

The vacuum system is composed of a primary Edwards rotary pump connected in series to a Varian Turbo-V 250 MacroTorr turbomolecular pump. The heating system is run by a Tectra HC3500 Heater Controller and the temperature is collected with an Impac IGA 120 pyrometer.

In few cases, air annealing treatments were done, using a Lenton muffle furnace, reaching a temperature of 500°C with heating and cooling ramps of 4°C/min. Dwell time was set at 2 hours.

2.5 Van der Pauw method (four-point probe)

In order to assess the electrical properties of the samples, the four-point probe method proposed by van der Pauw [84] was implemented. Such method allows to extract the resistivity and the Hall mobility of the films, regardless of its geometry or shape. Requirements to be satisfied are the following:

- uniform thickness of the samples;
- continuous film, with no holes across the surface;
- contacts of small dimension with negligible resistance, placed at the specimen's corners.

Once the contacts are placed on the sample's surface, an impressed current (at known value) flows between two subsequent contacts. The voltage drop is measured between the two remaining contacts (see Fig. 2.4). By changing the current

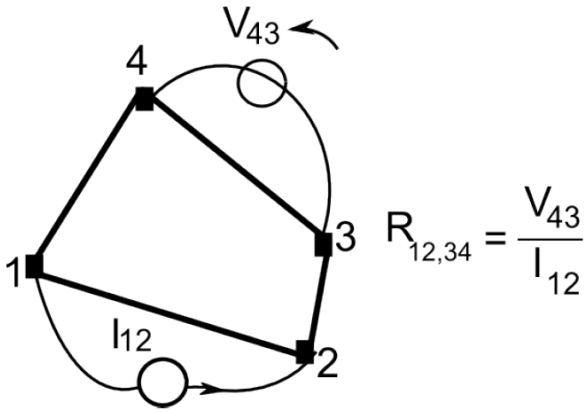

Figure 2.4: *Schematic representation of the 4-point probe method introduced by van der Pauw. Taken from [85].*

flow to the next couple of electrodes, 4 configurations are obtained. In addiction, it is possible to reverse the current direction, ending with a total of 8 configurations. The measured resistance values should respect the following equation due to symmetry condition:

$$\begin{aligned} R_{21,34} &= R_{12,43} \\ R_{32,41} &= R_{23,14} \\ R_{43,12} &= R_{34,21} \\ R_{14,23} &= R_{41,32} \end{aligned} \qquad \begin{aligned} R_{21,34} + R_{12,43} &= R_{43,12} + R_{34,21} \\ R_{32,41} + R_{23,14} &= R_{14,23} + R_{41,32} \end{aligned} \tag{2.1}$$

If Equations 2.1 are respected, it is possible to retrieve the resistance on the two sides of the sample (vertical and horizontal), respectively R_a and R_b. By exploiting the van der Pauw equation, the sheet resistance R_S is finally obtained:

$$e^{-\pi \frac{R_a}{R_S}} + e^{-\pi \frac{R_b}{R_S}} = 1 \tag{2.2}$$

The resistivity is recover just by multiplying R_S by the film's thickenss d:

$$\rho = R_S d \tag{2.3}$$

With the same setup, it is possible to perform Hall measurements to extrapolate the mobility μ of the film. A magnetic field $\mathbf{B}$ is applied perpendicularly with respect to the current flux, hence the electrons will experience a Lorentz force, which displaces them. Such displacement induce a potential difference, called Hall voltage V_H, orthogonal to the initial electric field that induce the current (see Fig. 2.5):

$$V_H = \frac{IB}{qdn} \tag{2.4}$$

where I is the current, B the magnetic field, d the film's thickness, q the particle's charge and n the carrier density. By using the Drude model, explained in section 1.1.1, the mobility is finally retrieved:

$$\mu = \frac{1}{qn\rho} \tag{2.5}$$

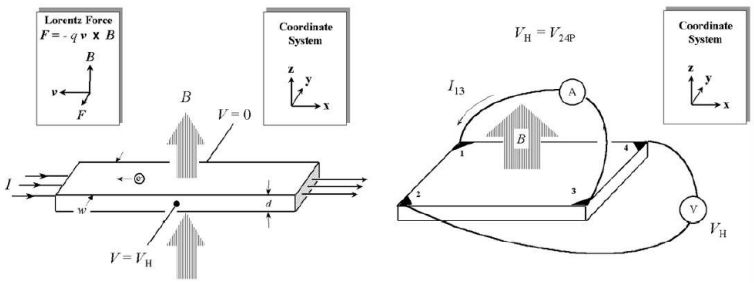

Figure 2.5: *On the left, a scheme of the Hall effect is shown. On the right, Hall effect measurement is represented. Taken from [85].*

To perform Hall mobility measurements, the cross configuration is used (see Fig. 2.5) rather then the parallel one, employed for resistivity measurements. The 2 initial configuration become 4 by inverting the current flow. In addition, it is possible to invert the magnetic field, hence the final configuration and values of V_H are 8. A zero $\mathbf{B}$ measurement is needed in order to assess the initial voltage

generated by the electric field in order to discriminate the contribution of the Hall effect alone.

The machinary used in my thesis work was a Keithley 2400 SourceMeter, used as a current source, and a Keysight 34972A LXI Data acquisition unit controlled with a computer. Each electrical configuration was achieved by a custom-built-switch, that selected the contacts between which the current flows. Raw data were analyzed by a specific MatLab code. Hall measurements were performed using a 0.57 T permanent magnet. In order to obtain an error bar, each sample was characterized multiple times.

2.6 UV/Vis/NIR Spectrophotometry

When light hits matter, a fraction of the intensity will be transmitted (T), one reflected (R), one absorbed (A) and a last portion will be scattered (S):

$$T + R + A + S = 1 \tag{2.6}$$

To establish the optical properties of the TCO films, a spectrophotometer was implemented. It consists of an integrating sphere (made by spectralon, a fluoropolymer with the highest reflectance among all materials) used to collect all the transmitted or reflected light, a light beam, several detectors to collect the light after the interaction and two sites where the samples can be located.

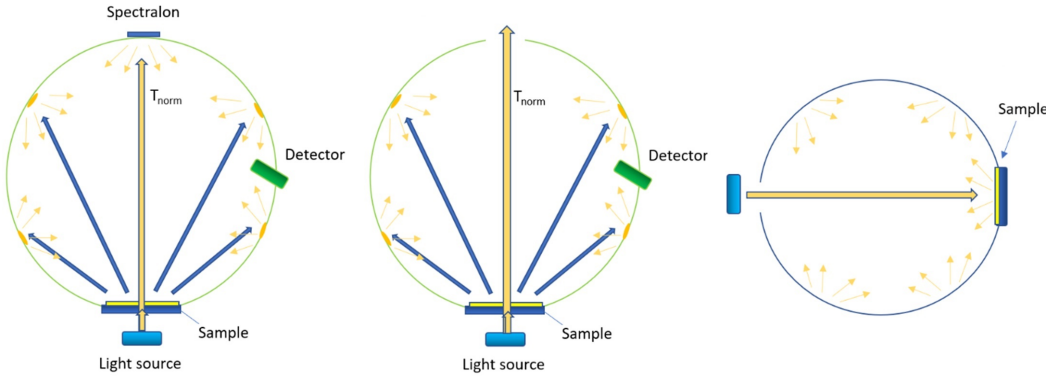

Figure 2.6: *Schematic representation of the three different configuration used to obtain the optical properties of the deposited films: total T on the left, diffuse T in the middle, R on the right.*

In order to get the transmittance T, the specimen is placed at the entrance of the integrating sphere, with the deposited film toward the sphere (see Fig. 2.6). The second aperture is occupied by a spectralon tap. In this configuration is possible to collect all the transmitted and diffuse light. To distinguished between

the direct and diffuse transmittance, the spectralon tap is removed, in order to let the transmitted light goes out and recover only the diffuse transmitted light. Another configuration is used to obtain the reflectance R (see Fig. 2.6). In this case, the sample is placed at the exit of the integrating sphere, with the film looking the light beam (hence the film is always toward the inside of the sphere). All signals are normalized as follows:

$$T_{film} = \frac{T_{tot}}{T_{glass}} \tag{2.7}$$

$$R_{film} = R_{tot} - \left(R_{glass} T_{film}^2\right) \tag{2.8}$$

The measurements were performed by Dr. C. Mancarella at the Centre for Nanoscience and Technology (CNST) of the Italian Institute of Technology (IIT) in Milan. The apparatus was composed by a Lambda 1050 UV/Vis/NIR system with a Perkin Elmer 150 mm integrating sphere. Transmittance and reflectance measurements were performed in the range 250-2000nm, with a data interval of 2 nm.

Chapter 3

Preliminary studies

Before depositing the Ta:TiO_2-only multilayers, it was necessary to understand the properties of the single components. A deep study on Ta:TiO_2 with 5% doping level (from now on shortened as TaTO5%) was carried out by Ornago [7] and Gaetani [8] in their thesis works. They explored different deposition pressure, both in pure oxygen and in mixed gas atmosphere, the effect of thickness on the electrical properties and the effect of different thermal treatments. In this chapter I show the electrical, optical and morphological properties of thin samples of Ta:TiO_2 with 10% level doping (from now on shortened as TaTO10%) deposited on glass and on stoichiometric titania. The aim is to improve the electrical properties and the degree of crystallinity of these ultrathin films in order to exploit them in thin multilayers. Later, the effect of higher deposition pressures will be presented. In this case, non-conductive films are expected, that combined with conductive layers should create a hyperbolic metamaterial.

3.1 Thin Ta(10%):TiO_2

Before showing the properties of the thin TaTO10%, I will make a brief summary of the previous work in which the attempt to produce thin layers had been made. The first try was carried on by Ornago, who was able to obtain conductive films of TaTO5% down to 20 nm on glass substrate [7]. He also explored the possibility to increase the dopant concentration up to 10%. He decided to use the same laser fluence employed for the TaTO5% (2.2 J/cm^2), which causes an incomplete crystallization after the vacuum annealing thermal treatment. For this reason, the electrical properties achieved were not optimal and showed higher resistivity and a very low mobility with respect to TaTO5%. B. Bricchi found the optimal fluence at 2.73 J/cm^2, obtaining a full crystallization of the samples, increased mobility and lower resistivity [86] (work still in progress and not published yet). Gaetani tried to

Deposition parameters					Electrical properties		
Reference	Substrate	d (nm)	Ta%	F $\left(\frac{J}{cm^2}\right)$	ρ (Ωcm)	n $\left(\frac{1}{cm^3}\right)$	μ $\left(\frac{cm^2}{Vs}\right)$
Past work	Glass	50	5	2.2	1.2×10^{-3}	1×10^{21}	5.32
Past work	Glass	20	5	2.2	6×10^{-3}	6.87×10^{20}	1.5
Past work	Glass	10	5	2.2	0.49	2.26×10^{19}	-
Past work	Glass	50	10	2.73	1.21×10^{-3}	1.56×10^{21}	4.09
Past work	Glass	20	10	2.73	3.82×10^{-3}	7.4×10^{20}	2.26
Past work	Glass	10	10	2.73	0.54	3.58×10^{19}	0.31
Past work	TiO_2	50	5	2.2	1.5×10^{-3}	1×10^{21}	4
Past work	TiO_2	20	5	2.2	2.8×10^{-3}	8.8×10^{20}	2.6
Past work	TiO_2	10	5	2.2	$2.6. \times 10^{-2}$	-	-
Past work	TiO_2	5	5	2.2	-	-	-
This work	TiO_2	20	10	2.73	1.25×10^{-3}	1.85×10^{21}	2.72
This work	TiO_2	10	10	2.73	6.65×10^{-3}	4.94×10^{20}	2
This work	TiO_2	5	10	2.73	3.28×10^{-2}	3.25×10^{20}	0.79
This work	Glass	20	10	2.73	1.57×10^{-3}	1.83×10^{21}	2.28
This work	Glass	10	10	2.73	-	-	-
This work	Glass	5	10	2.73	-	-	-

Table 3.1: *Several samples of TaTO deposited at different parameters and substrate, with their respective electrical properties: ρ is the resitivty, n is the carrier density, μ is the mobility. The titania substrate is always 50 nm thick; F is the laser fluence.*

further reduce the thickness of TaTO5% layers, but with a different approach. He deposited 50 nm, 20 nm, 10 nm and 5 nm thick layers on a stoichiometric titania substrate [8]. As a clarification, it is not the case of epitaxial growth, because the underneath TiO_2 layers are polycrystalline, but the presence of crystalline grains can ease the crystallization process of TaTO5%. Before depositing the TaTO5%, 50 nm thick films of TiO_2 were annealed in air for 4 hours at 500°C, hence they had to be considered non-conductive, since the air annealing thermal treatment fills all the oxygen vacancies in the anatase structure. 50 nm and 20 nm thick samples were successfully produced, with good electrical properties, whereas it wasn't possible to assess the electrical properties of the 10 nm and 5 nm thick film. Gaetani gave as a reason the presence of a dead layer of 8 nm, arising from diffusion of Ta in the titania layer or diffusion of oxygen from the titania into the TaTO5% film.

The same approach was exploited in my work to deposit thin films of TaTO10% and to observe if the electrical properties would be enhanced. All the analysis performed below were done on thermally treated samples (vacuum annealing). SEM images in Fig. 3.1 do not show a marked interface between the titania substrate and the TaTO10% layers, which can be attributed to a continuity in the

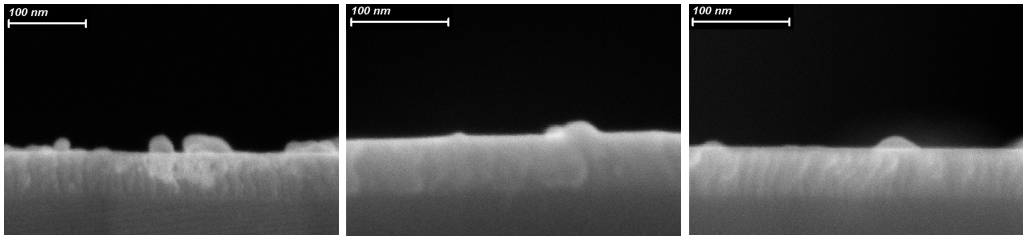

(a) *(b)* *(c)*

Figure 3.1: *SEM images of the TaTO10% layers deposited on 50 nm of titania. (a) 20 nm thick layer, (b) 10 nm thick layer and (c) 5 nm thick layer.*

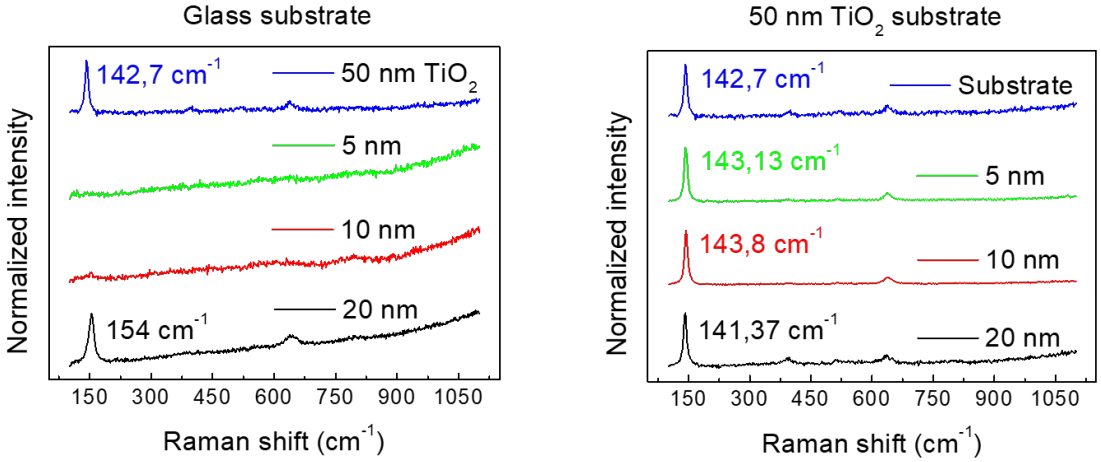

(a) *(b)*

Figure 3.2: *(a) Raman spectra of TaTO10% deposited on glass substrate. (b) Raman spectra of TaTO10% deposited on titania substrate.*

crystal structure. The same three thin layers (20 nm, 10 nm, 5 nm) were deposited on glass too, but SEM images were not acquired.

For these samples, the interpretation of the Raman spectra in Fig. 3.2a is unequivocal. The 20 nm thick layer has crystallized, whereas the 10 nm and 5 nm thick layers have not. The considerable $E_g(1)$ blue shift (154 cm^{-1}) in case of 20 nm layer is attributed to the high carrier density in TaTO10%, as predicted from the $E_g(1)$-carrier density relationship found by Mazzolini *et. al.* [18]. By looking the Raman spectra in Fig. 3.2b, it would seem that all the TaTO10% layers have crystallized, due to the presence of the characteristic anatase peak. However, the position of the $E_g(1)$ peak is around 142 cm^{-1}, indicating that the possible signal of the thin TaTO10% layers (20 nm, 10 nm, 5 nm) is completely covered by the strong signal coming from the thicker titania substrate (50 nm). Thus, by looking at the Raman spectra alone, the crystallization of the samples cannot be asses for sure. Nevertheless, it is not enough to establish if the 10 nm and 5 nm layers

deposited on TiO_2 are still amorphous, due to the lattice matched substrate.

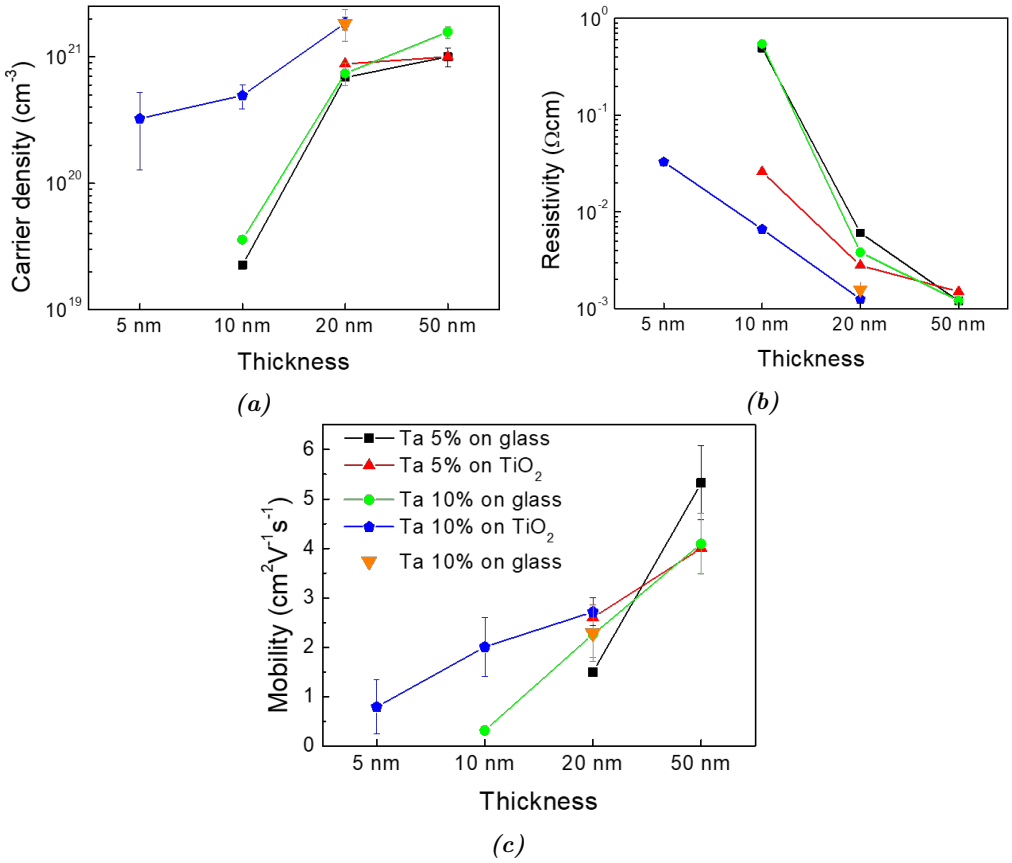

Figure 3.3: *(a) carrier density, (b) resistivity, (c) mobility of thin layers of TaTO deposited on glass and TiO_2. The upside down orange triangle stands for the sample deposited in this work. All the values are reported in table 3.1.*

Electrical analysis helps to understand, since it was possible to measure all the three samples deposited on TiO_2, indicating that at least a partial crystallization has occurred. The electrical properties of the 20 nm on titania shows outstanding resistivity and carrier density values (see Fig. 3.3) not expected from TaTO10% that usually presents more defects and lower mobility due to the higher dopant concentration. In fact, not only it outperforms the counterpart deposited on glass, but also the counterpart of TaTO5% deposited on the titania substrate. In addition, the 20 nm thick layer exhibits almost the same resistivity and carrier density of a TaTO10% 50 nm thick sample deposited on glass ($\sim 1.2 \times 10^{-3}\ \Omega cm$ and $\sim 1 \times 10^{21}\ cm^{-3}$), but with a lower mobility (2.72 instead of 4.09 $cm^2V^{-1}s^{-1}$). The same discussion holds for the 10 nm layer on titania: if both the counterparts of TaTO10% on glass and of TaTO5% on TiO_2 resulted almost insulating, the 10 nm TaTO10% sample on titania shows very good properties, similar to

a 20 nm layer of TaTO5% on glass ($\sim 6 \times 10^{-3}\ \Omega cm$, $\sim 5 \times 10^{20}\ cm^{-3}$ and $\sim 2\ cm^2V^{-1}s^{-1}$). Electrical properties can be measured, against expectations, even for the 5 nm thick specimen on TiO_2, although it presents poor properties. In fact, no measurements have been reported for such low thickness neither of TaTO5% or TaTO10%. Moreover, it possesses better properties than a 10 nm thick layer of TaTO5% deposited both on glass and on titania, and a 10 nm thick layer of TaTO10% deposited on glass (values are reported in table 3.1).

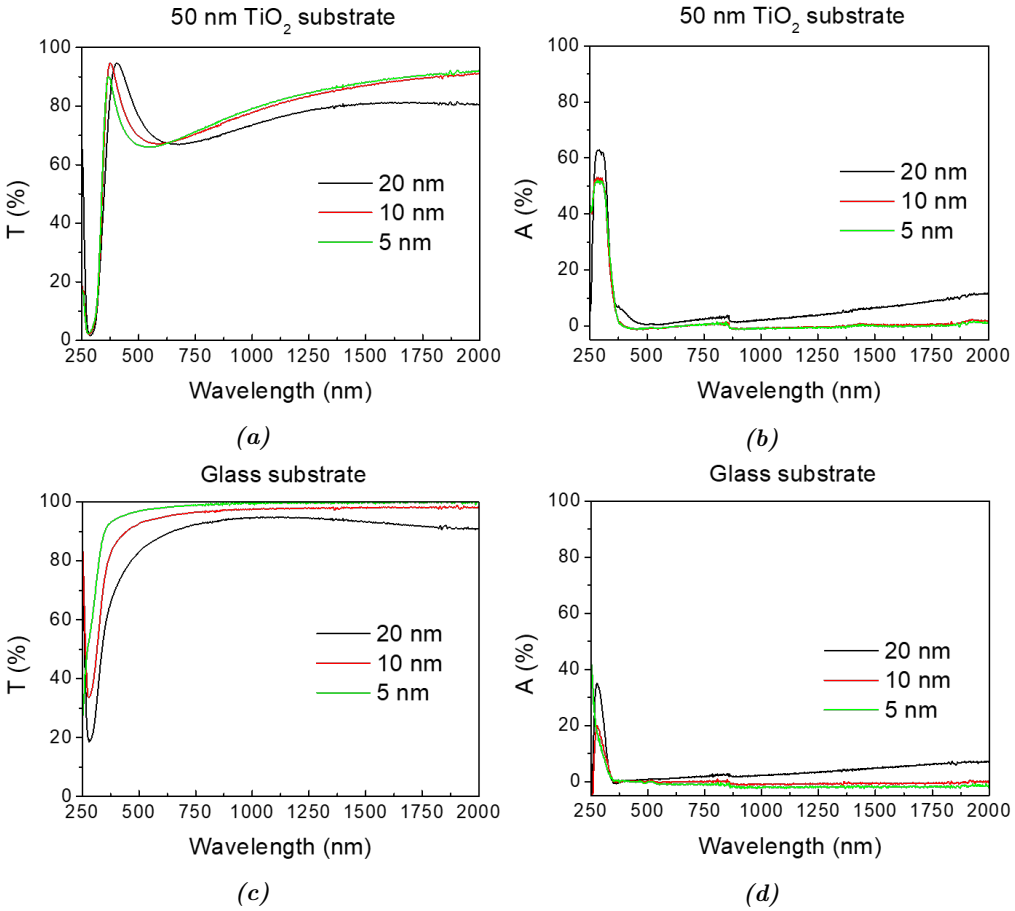

Figure 3.4: *(a) T (transmission) spectra of TaTO10% deposited on titania substrate. (b) A (absorbance) spectra of TaTO10% deposited on titania substrate. (c) T (transmission) spectra of TaTO10% deposited on glass substrate. (d) A (absorbance) spectra of TaTO10% deposited on glass substrate.*

As a concluding remark, it can be stated that the TiO_2 substrate influences much more the crystallization and the electrical properties of TaTO10% rather than TaTO5%. The reason might be associated to the higher carrier density of TaTO10% that avoid the formation of the dead layer. Moreover, it is possible that TaTO10% wets better the surface, hence a layer by layer growth is favoured

with respect to an island growth, giving in return continuous films already at 5 nm and 10 nm. The results obtained are very promising, since the TaTO5% layers on titania did not show such improvement in the electrical properties due to the aforementioned dead layer.

Electrical characterization on the samples deposited on the glass substrate was possible only on the 20 nm thick layer. Such sample shows similar values of mobility and resistivity with respect to previously deposited samples, whereas the carrier density has doubled (from $7.4 \times 10^{20}\ cm^{-3}$ to $1.83 \times 10^{21}\ cm^{-3}$). Furthermore, the 20 nm film of TaTO10% on glass deposited in this work shows better properties with respect to 20 nm of TaTO5% deposited both on glass or titania substrate.

The corresponding optical properties are displayed in Fig 3.4. For thicker samples transmittance reduces and absorbance increases, in agreement with the Lambert-Beer law. Samples deposited on 50 nm titania show an interference fringe at $\sim$ 600 nm in the transmission spectra probably caused by the titania substrate, not present in the case of specimen deposited on glass substrate. The slight increase in the absorption towards 2000 nm may be caused by the carrier density, associated to a plasmonic response.

3.2 Increasing the pressure

It is well known that increasing the deposition pressure causes the formation of porous and less conductive films [7], [8], [17], [18]. Such non-conductive layers can be employed in the multilayer structure in the attempt of creating a new metamaterial. From previous studies, it was discovered that films of TaTO5% deposited in the pressure range of $0.5 \div 4$ Pa in pure oxygen exhibit a compact structure and they crystallize into anatase after the vacuum annealing thermal treatment [7], [8]. In particular, the best electrical properties were achieved at 1 Pa, while increasing the pressure resulted in their deterioration (resistivity $\sim 10^{-2}$ Ωcm, carier density $\sim 10^{20}\ cm^{-3}$ and mobility $\sim 10^{-1}\ cm^2V^{-1}s^{-1}$) due to oxygen related defects that act as electron traps.

In order to obtain a porous structure, a 400 nm thick sample of TaTO5% was deposited at 6 Pa (in pure oxygen) and SEM analysis reveals the porous morphology as expected (see Fig. 3.5a). The film doesn't crystallize after the vacuum thermal treatment (see Fig. 3.6). A possible reason can be attributed to a higher oxygen desorption due to a higher surface area exposed, leading to a too defective structure. On the contrary, it was shown that TiO_2 films crystallize into anatase if thermally treated in air [87]. As a consequence, electrical characterization was not possible to perform. The optical analysis will be presented shortly after, for a better comparison of the obtained spectra.

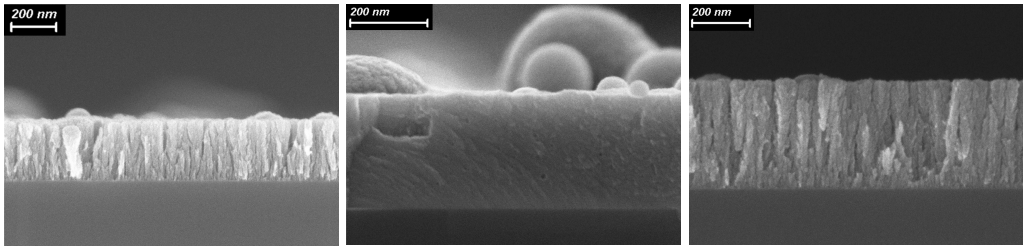

(a) *(b)* *(c)*

Figure 3.5: *SEM image of (a) TaTO5% deposited at 6 Pa, (b) TaTO10% deposited at 3 Pa and (c) TaTO10% deposited at 6 Pa in pure oxygen atmosphere.*

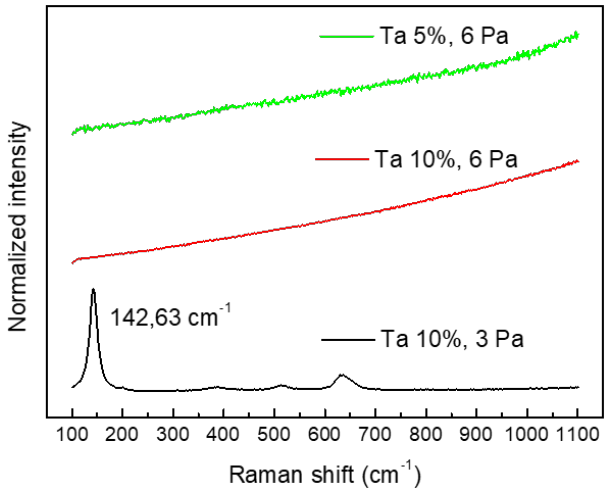

Figure 3.6: *Raman spectra of vacuum annealed TaTO5% deposited at 6 Pa and TaTO10% deposited at 3 Pa and 6 Pa in pure oxygen atmosphere.*

Then, I studied the effect of higher pressure on more doped films as well, namely TaTO10%. The selected pressures were 3 Pa and 6 Pa, since these values should give a compact and a porous structure. The samples were vacuum annealed and then characterized. The thickness was set to 500 nm for both films.

SEM images confirmed that at 3 Pa the film remains compact, whereas at 6 Pa a more porous structure arises (see Fig. 3.5b and 3.5c).

From the Raman spectra in Fig. 3.6, it can be easily observed that only the 3 Pa layer crystallizes in anatase ($E_g(1)$ peak at $142\,cm^{-1}$), whereas the 6 Pa layer has not. The same explanation previously stated for TaTO5% holds for the corresponding TaTO10% deposited at 6 Pa. As a consequence, it was possible to perform the electrical analysis only on the 3 Pa specimen. As expected from a higher pressure deposited sample, the electrical properties were poor with $\rho = 0.142\ \Omega cm$, $n = 4.48 \times 10^{19}\ cm^{-3}$ and $\mu = 1.77\ cm^2V^{-1}s^{-1}$. The optical properties of the aforementioned samples (TaTO5% at 6 Pa, TaTO10% at 3 Pa and TaTO10% at 6

Pa) are depicted in Fig. 3.7. It can be seen that both the TaTO5% and TaTO10% deposited at 6 Pa films show weaker contribution from interference fringes, higher transmittance and higher absorbance than the TaTO10% deposited at 3 Pa film. Such behaviour can be justified by considering that the 6 Pa samples are amorphous and possess a porous structure, hence it can entrap the light, favouring enhanced absorption. Such hypothesis can be supported by the low reflectance with respect the 3 Pa specimen. The estimated optical band gap with the Tauc plot calculation for these 3 films are 3.375 eV, 3.18 eV and 3.09 eV for TaTO10% at 3 Pa, TaTO10% at 6 Pa and TaTO5% at 6 Pa respectively.

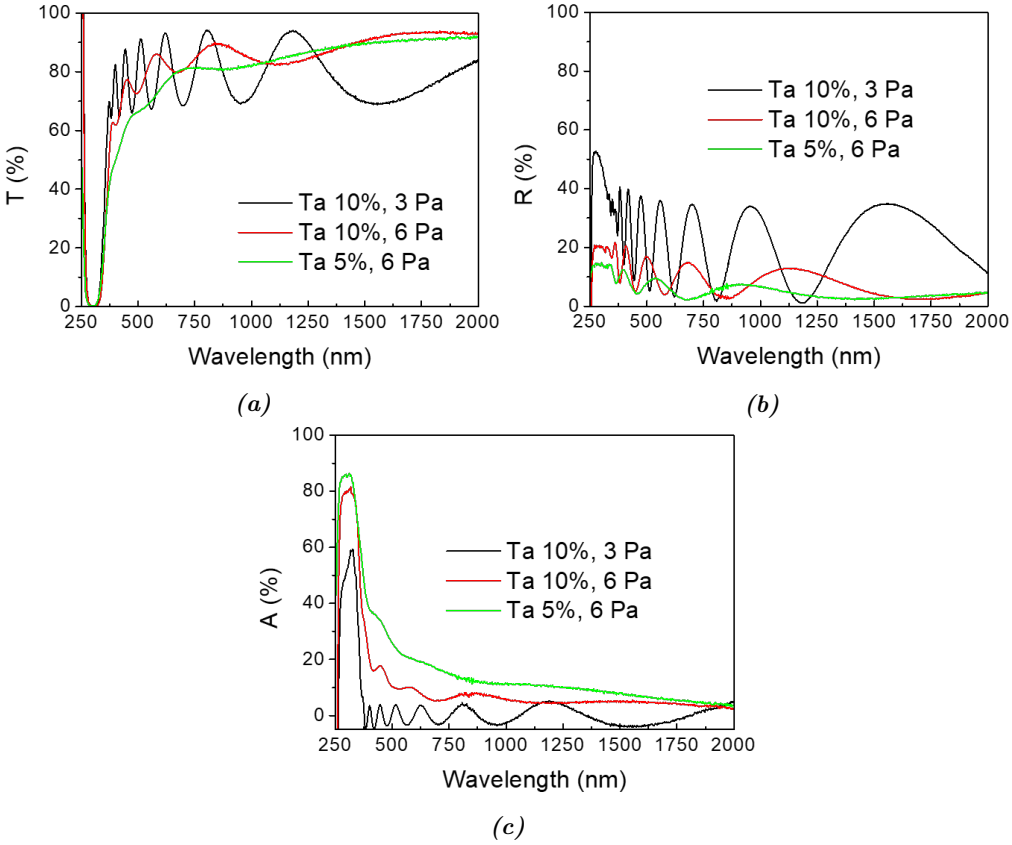

Figure 3.7: *(a) T, (b) R and (c) A of TaTO5% deposited at 6 Pa and TaTO10% deposited at 3 Pa and 6 Pa in pure oxygen atmosphere.*

3.2.1 Mixed atmosphere

Not only oxygen, but a mixed atmosphere of Ar:O_2 in proportion 5:1 was explored. Such ratio was optimized in previous works [7], [8]. The aim of the mixed atmosphere is dual: at low pressure, since Ar atoms are lighter than oxygen molecules, the plasma plume possesses less "stopping power" with respect to the same pres-

sure in pure oxygen. Therefore, the ablated species arrive at the substrate with higher kinetic energy and the deposited films are more compact and with numerous defects. At higher pressure, the objective is to obtain conductive porous films, since the pressure can be increased with a low content of oxygen, hence preserving the defect chemistry of the anatase structure. Previous works [7], [8] on TaTO5% had shown that up to 6 Pa the films crystallized after vacuum thermal treatment, while electrical characterization was possible only on the 4 Pa sample, with a resistivity of 2.2×10^{-2} Ωcm. Since the 4 Pa films in Ar:O_2 shew poor electrical properties, in my work I deposited a 500 nm thick film at 3 Pa in mixed atmosphere hoping to improve them. SEM image shows a compact, but more defective structure (see Fig. 3.8a) due to the high kinetic energy particles. Indeed, the Raman spectra appears more noisy and the $E_g(1)$ peak is blue-shifted to 147 cm^{-1}, indicating that the films might possess higher carrier density (see Fig. 3.8b).

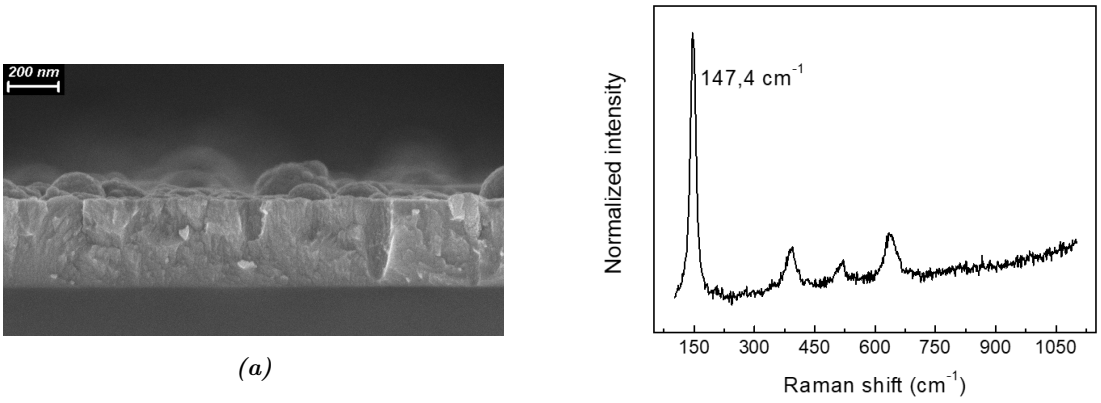

(a) *(b)*

Figure 3.8: *(a) SEM image and (b) the Raman spectra of TaTO5% deposited at 3 Pa in mixed Ar:O_2 atmosphere, 500 nm thick.*

In fact, the electrical properties reveal a conductive behaviour of such film ($\rho = 4.84 \times 10^{-3}$ Ωcm, $n = 6.19 \times 10^{20}$ cm^{-3} and $\mu = 2.46$ $cm^2V^{-1}s^{-1}$), never obtained before for films deposited at 3 Pa in pure oxygen ($\rho = 0.142$ Ωcm, $n = 4.48 \times 10^{19}$ cm^{-3} and $\mu = 1.77$ $cm^2V^{-1}s^{-1}$ for TaTO10%). The carrier density value is in agreement with the Raman shift reported in [18]. Moreover, such values are close to a 100 nm thick film of TaTO5% deposited at 1 Pa in pure oxygen ($\rho = 1 \times 10^{-3}$ Ωcm, $n = 9,86 \times 10^{20}$ cm^{-3} and $\mu = 3$ $cm^2V^{-1}s^{-1}$), the atmosphere that gives the best electrical properties. For what concerns the optical properties (see Fig. 3.9), the sample deposited in mixed atmosphere shows lower transmittance and higher absorbance compared to the TaTO10% deposited at 3 Pa in pure oxygen, due to the higher carrier density and the more compactness (deposition rate is lower than in pure oxygen). Approaching 2000 nm, the TaTO5%

shows decreasing T and increasing A, therefore it might be due to the plasma frequency falling in the NIR. The estimated optical band gap with the Tauc plot calculation results 3.26 eV.

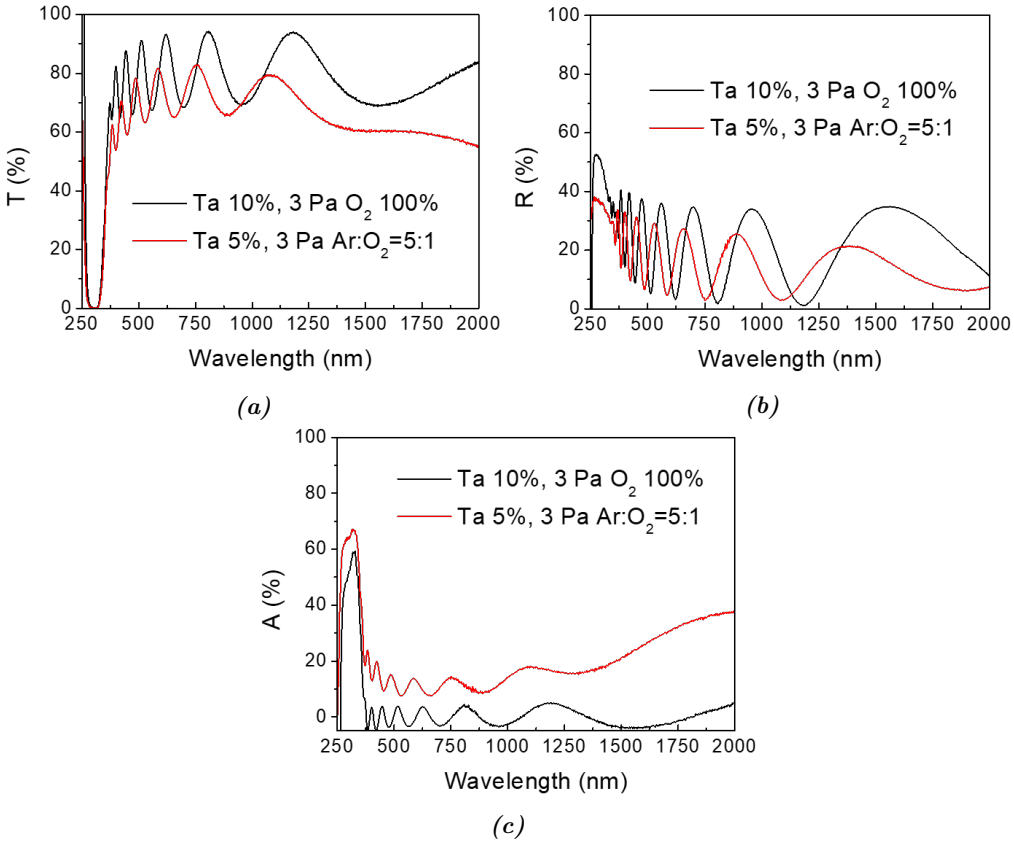

Figure 3.9: *(a) T, (b) R and (c) A of TaTO5% deposited at 3 Pa in mixed atmosphere and TaTO10% deposited at 3 Pa in pure oxygen atmosphere.*

Summarizing, thin layers of 20 nm, 10 nm and 5 nm of TaTO10% deposited on a titania substrate have been produced. The first and second one exhibits optimal electrical properties compared to a sample deposited on glass substrate or to TaTO5% of same thickness. Electrical characterization is possible even on the thinnest layer, a result never obtained before.

When the pressure is increased, layers of both TaTO5% and TaTO10% deposited at 6 Pa in pure oxygen resulted amorphous. On the contrary, at 3 Pa crystallization occurr for both TaTO5% and TaTO10%. In a pure oxygen atmosphere the film results insulating, while the mixed atmosphere ($Ar:O_2$=5:1) is able to produced conductive films.

Chapter 4

Multilayers

In this chapter, the properties of TaTO-only multilayers will be presented. The architecture consists of alternating non-conductive and conductive layers. All the samples are composed of 10 layers: 5 are deposited at higher pressure, in order to behave as non-conductive layers and 5 are deposited at 1 Pa in pure oxygen, hence conductive. The last one is always the conductive one, in order to allow electrical characterization. Stoichiometric TiO_2 has not be used for the dielectric component in order to deposited the multilayers in a single step deposition, without opening the vacuum chamber, thus reducing a lot the deposition time. Therefore, for the non-conductive layers, both 3 and 6 Pa in oxygen were explored. These two particular values were selected since with the former a compact structure is obtained, while with the latter a porous one is achieved, hence differences in electrical and optical properties can arise (see section 1.2.4). Moreover, since the dielectric component changes, the hyperbolic range can change.

Different architectures have been designed. The first and simplest one was composed by conductive and non-conductive layers of same thickness. This structure was produced both with only TaTO5% or TaTO10% and alternating pressure of 3 Pa and 1 Pa or 6 Pa and 1 Pa (from now on shortened as 3/1 Pa and 6/1 Pa) in pure oxygen atmosphere. In the second system, different thicknesses were used. In one case the higher pressure layers were doubled with respect the conductive ones, in the other the opposite configuration was explored. Again, both TaTO5%-only and TaTO10%-only structures were deposited and only 3/1 Pa was employed in pure oxygen atmosphere. Lastly, a change in the gas atmosphere was examined, in particular layers deposited at 3 Pa of $Ar:O_2$=5:1 were alternated with layers at 1 Pa in pure oxygen, in order to obtain a fully conductive multilayers. Only TaTO5% was used for this structure.

All the analysis were performed after the vacuum annealing thermal treatment. Even though the electrical characterization was always performed on the 1 Pa layer

(the last one), the obtained values have to be considered as effective properties of the whole film, since a contribution from the layers below can be non-negligible.

P (Pa)	Gas	Ta%	d_{1Pa} (nm)	$d_{HigherP}$ (nm)	d_{nom} (nm)	d_{meas} (nm)
3/1	O_2	5	20	20	200	208
3/1	O_2	5	10	10	100	103
6/1	O_2	5	20	20	200	181
6/1	O_2	5	10	10	100	88
3/1	O_2	10	20	20	200	176
3/1	O_2	10	10	10	100	90
6/1	O_2	10	20	20	200	154
6/1	O_2	10	10	10	100	73
3/1	O_2	10	40	20	300	272
3/1	O_2	10	20	40	300	261
3/1	O_2	5	40	20	300	272
3/1	O_2	5	20	40	300	271
3/1	Ar:O_2/O_2	5	20	20	200	186
3/1	Ar:O_2/O_2	5	10	10	100	90

Table 4.1: *List of all the multilayers deposited in this thesis work. d_{1Pa} stands for the thickness of the 1 Pa layer; $d_{HigherP}$ stands for the thickness of the 3 or 6 Pa layer; d_{nom} is the nominal thickness of the multilayers; d_{meas} is the measured thickness of the multilayers.*

4.1 Ta 5%, metal filling content p=0.5

In this section, multilayers of TaTO5% will be analysed, in which the compact and the higher pressure layers have the same thickness, hence metal filling content $p = 0.5$ (see Eq. 1.10). First, using the pressure of 3/1 Pa in pure oxygen two samples were deposited, one with single layer thickness of 20 nm (for a total nominal thickness of 200 nm) and one with thinner layer of 10 nm (for a total nominal thickness of 100 nm). Later, the same approach was employed for the pressure of 6/1 Pa, for a total of four samples.

SEM analysis of morphology

From the cross section SEM images, the 3/1 Pa structures appear compact and homogeneous as expected, and the single component cannot be distinguished (see Fig. 4.1a and 4.1b). The measured thickness (from SEM cross sections) of these multilayers is in good agreement with the nominal one, with an average value of 208 nm for the thicker structure and 103 nm for the thinner one.

Looking at the SEM images of the 6/1 Pa structures (see Fig. 4.1c and 4.1d), it is possible to discern the single layers without any effort. The compressed layers

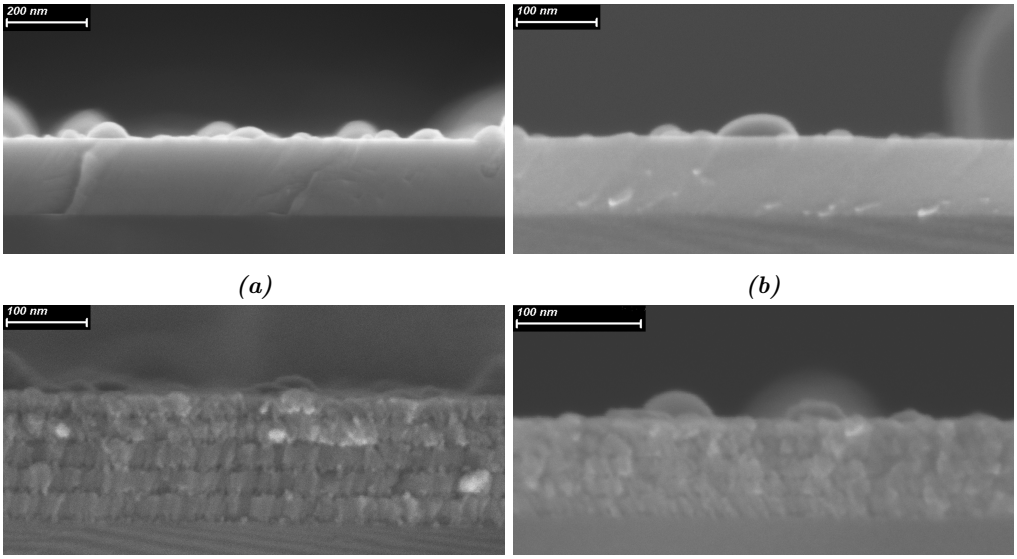

Figure 4.1: *SEM images of TaTO5% multilayers deposited at (a) 3/1 Pa, thicker sample (200 nm), (b) 3/1 Pa, thinner one (100 nm), (c) 6/1 Pa, thicker sample (200 nm) and (d) 6/1 Pa, thinner one (100 nm).*

correspond to the ones deposited at 6 Pa. The squeezing effect of the porous layers can be attributed to the weight of the above compact layer deposited at 1 Pa and/or to an effect of interpenetration of the latter in the former. As a consequence, the measured thickness results lower with respect the nominal one, respectively 181 nm for the thicker multilayers and 88 nm for the thinner one.

Raman analysis

From the Raman spectra (see Fig. 4.2), it can be seen that the characteristic peaks of anatase TiO_2 are present, thus all the four structures crystallize after the vacuum annealing. In particular, the 6/1 Pa multilayers appear noisier than the 3/1 Pa due to the amorphous component (layer at 6 Pa). In fact, in section 3.2, the TaTO5% film resulted amorphous after the vacuum annealing. For both deposition pressures, the thinner structures show noisier spectra with respect to the thicker ones. The $E_g(1)$ peaks are more blue-shifted for the 6/1 Pa structure than the 3/1 Pa ones: in the former, the signal is coming only from the layers at 1 Pa since the ones at 6 Pa are amorphous and give zero contribution; in the latter, the Raman signal is coming from both layers at 3 Pa and 1 Pa, hence the peak position is a convolution of the two. As explained in section 1.2.4, Mazzolini *et. al.* [18] found a relation that linked the carrier density and the Raman shift of the $E_g(1)$ peak. Layers at 3 Pa behave as dielectric, hence their peak position

resemble the anatase TiO_2 one. On the contrary, layers deposited at 1 Pa possess higher carrier density, hence a blue-shift is present on the peak position.

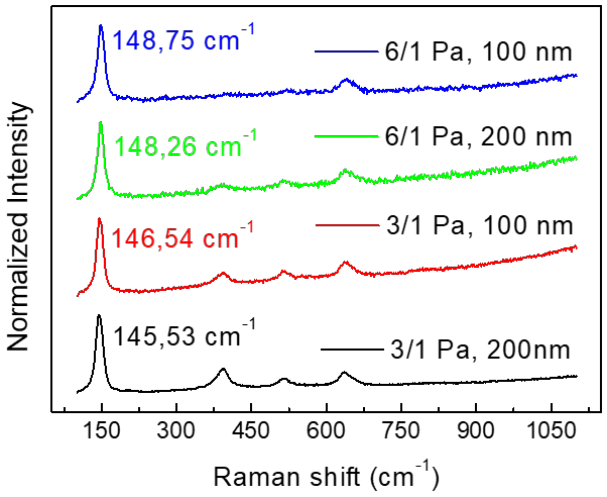

Figure 4.2: *Raman spectra of the 3/1 Pa and 6/1 Pa TaTO5% multilayers after vacuum annealing.*

Electrical properties

Electrical characterization was possible on all the four samples (see table 4.2). The electrical properties of the TaTO5% 6/1 Pa multilayers improve for higher thickness, since surface scattering at the interfaces becomes less relevant. In addition, the reported values for these multilayers are better than TaTO5% thin films of 20 nm and 10 nm deposited at 1 Pa in pure oxygen. On the contrary, the electrical properties of the TaTO5% 3/1 Pa multilayers do not show a particular trend. In these films, by reducing the thickness, the resistivity decreases and the carrier density increases. Such behaviour is unusual, because it has been proved that lowering the thicknesses causes a deterioration of such properties [7]. Nevertheless, the electrical properties of TaTO5% thin films of 20 nm and 10 nm deposited at 1 Pa are worse than the 3/1 Pa multilayers. In general, the 3/1 Pa films possess higher resitivity and lower mobility with respect to the 6/1 Pa counterparts. Such behaviour is rather unexpected and counterintuitive since the introduction of amorphous and porous layers is supposed to worsen the electrical properties. It seems like that the TaTO5% is not the right choice for the production of multilayer with tunable properties, since a significant variation of the properties between the four samples is not present (see Fig. 4.3). More details will be provided in the next sections. The four multilayers possess worse properties with respect to film of equal thickness of TaTO5% deposited at 1 Pa in pure oxygen. It is not surprising,

Deposition parameters					Electrical properties		
P (Pa)	d_{nom} (nm)	d_{meas} (nm)	Ta%	F $\left(\frac{J}{cm^2}\right)$	ρ (Ωcm)	n $\left(\frac{1}{cm^3}\right)$	μ $\left(\frac{cm^2}{Vs}\right)$
3/1	200	208	5	2.2	6.07×10^{-3}	4.2×10^{20}	3.36
3/1	100	103	5	2.2	5.97×10^{-3}	5.98×10^{20}	1.86
6/1	200	181	5	2.2	4.37×10^{-3}	4.37×10^{20}	3.62
6/1	100	88	5	2.2	4.97×10^{-3}	3.97×10^{20}	3.22
1	200	200	5	2.2	7.26×10^{-4}	9.2×10^{20}	8.36
1	100	100	5	2.2	1×10^{-3}	9.86×10^{20}	6.3

Table 4.2: *Electrical properties of TaTO5% multilayers deposited at 3/1 and 6/1 Pa in pure oxygen. d_{nom} and d_{meas} stand for the nominal and measured thickness respectively. F is the laser fluence.*

since the insertion of non-conductive layers is expected to deteriorate the electrical properties.

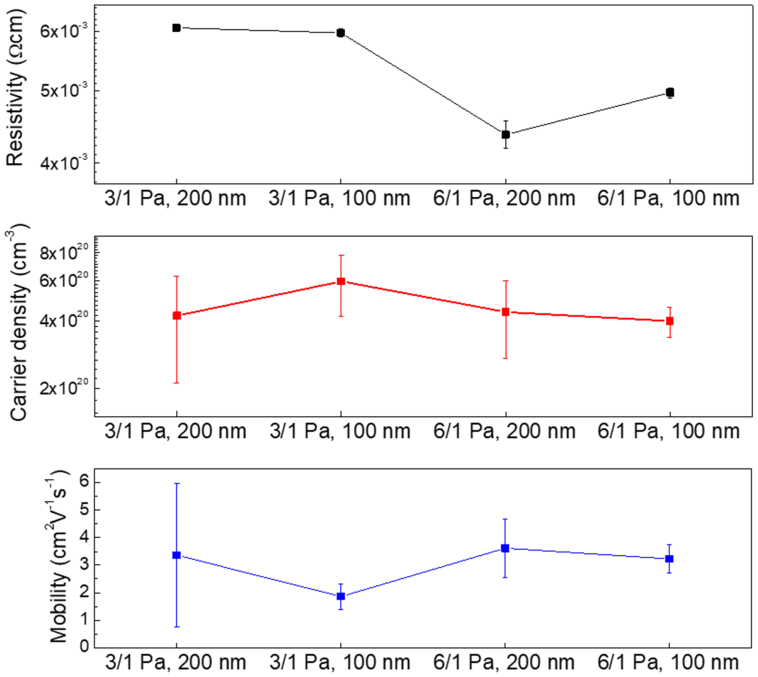

Figure 4.3: *Electrical properties of TaTO5% multilayers deposited at 3/1 and 6/1 Pa in pure oxygen.*

Optical properties

The optical properties of the TaTO5%-only multilayers display a specific trend: thicker films show more interference fringes, lower transmittance and higher reflectance toward the NIR region with respect to the thinner ones, in accordance

to the Lamber-Beer law (see Fig. 4.4). Moreover, the 6/1 Pa multilayers exhibit higher transmittance and lower reflectance than their 3/1 Pa counterparts, due to the presence of the amorphous and porous layers at 6 Pa that allow the passing of light more easily. The absorbance spectra appear almost the same for all the four films. Approaching 2000 nm, the absorbance tail of the 3/1 Pa 100 nm thick multilayers is the highest (see Fig. 4.4c). Such behaviour can be related to the free carrier absorption, since it possesses a higher carrier density with respect to the other samples.

All the four structures do not show signs of plasmonic response, hence the plasma frequency and the hyperbolic regime might be in the deep infrared part of the spectrum. Ellipsometric analysis must be performed to assess where such multilayers exhibit the hyperbolic dispersion relation.

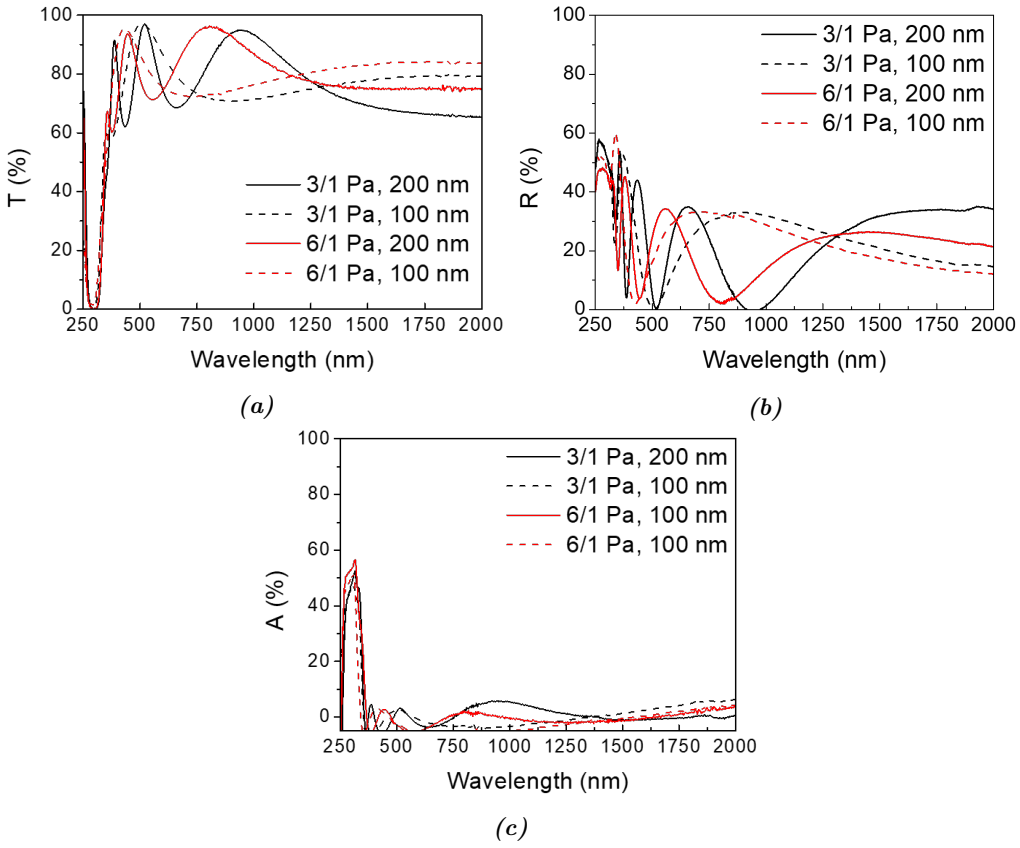

Figure 4.4: *(a) T, (b) R and (c) A of TaTO5% mulitlayers deposited at 3/1 Pa and 6/1 Pa in pure oxygen atmosphere.*

To sum up, four TaTO5% multilayers have been produced. The SEM images, Raman spectra and optical analysis reflect the predicted behaviour of such films: compact structure for the 3/1 Pa multilayers, $E_g(1)$ peak position more shifted for

6/1 Pa films and higher transmissivity for thinner sample and higher pressure. The main concern regards the electrical properties, especially for the 3/1 Pa structures. The measured ρ, n and μ exhibited unexpected values. In fact, fully crystalline films should possess better properties with respect to multilayers with amorphous component. Finally, the little change in the optical and electrical properties might be a sign that TaTO5% is not the right material to obtain significant modulation of the plasmonic response.

4.2 Ta 10%, metal filling content p=0.5

In this section, multilayers with higher Ta content (10%) will be analyzed. The architectures are the same explained in section 4.1, hence 3/1 Pa and 6/1 Pa structures with single layers of equal thickness, first 20 nm, later 10 nm, for a total of four multilayers, for a nominal thickness of 200 nm and 100 nm.

SEM analysis of morphology

SEM images display compact structures for the 3/1 architectures, with no distinction between the single layers. Even though the 3/1 multilayers look compact, the measured thickness is lower with respect to the nominal one, respectively of 176 nm and 90 nm instead of 200 nm and 100 nm.

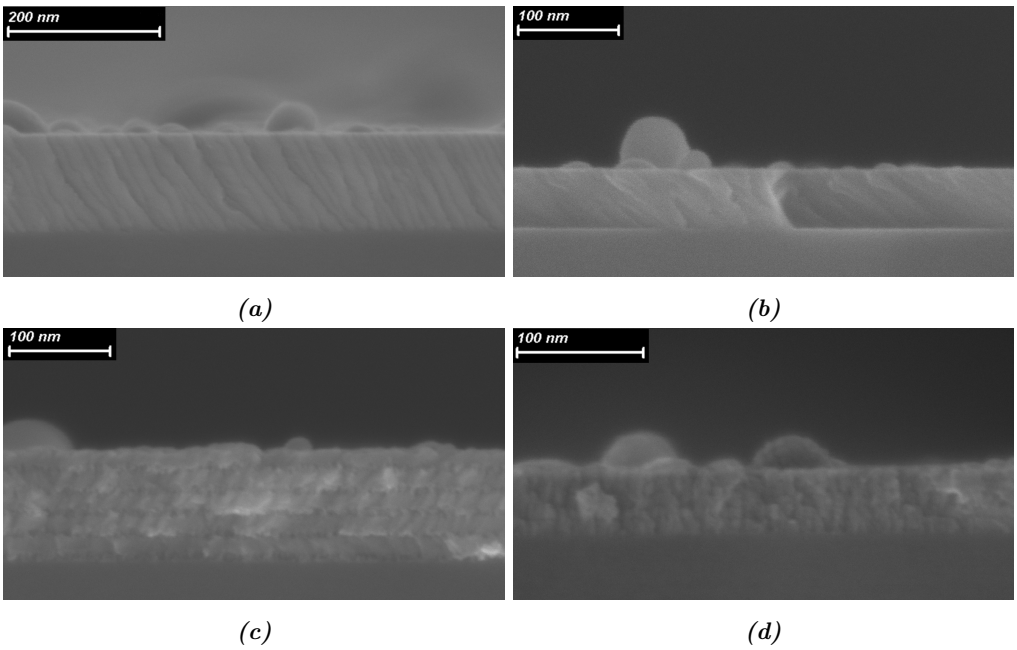

Figure 4.5: *SEM images of TaTO10% multilayers deposited at (a) 3/1 Pa, thicker sample (200 nm), (b) 3/1 Pa, thinner one (100 nm), (c) 6/1 Pa, thicker sample (200 nm) and (d) 6/1 Pa, thinner one (100 nm).*

On the contrary, in the 6/1 Pa multilayers each layer is clearly visible, and the porous one (6 Pa) appears thinner, exactly as observed in the TaTO5% 6/1 Pa multilayers. The reasons of this squeezing effect are the same given for the TaTO5% 6/1 Pa multilayers. As a consequence of the squeezing, the thicknesses of these multilayers are 154 nm and 73 nm respectevely.

Raman analysis

The Raman spectra of these architectures exhibit the characteristic $E_g(1)$ peak, sign that all four multilayers have crystallized after the vacuum annealing (see Fig. 4.8b). Such consideration is not trivial, especially for the 6/1 Pa 100 nm thick structure since it implements an amorphous 10 nm thick layer at 6 Pa (see section 3.2) and a 10 nm thick layer at 1 Pa of TaTO10%, which has been shown to not crystallize on glass substrate (see section 3.1).

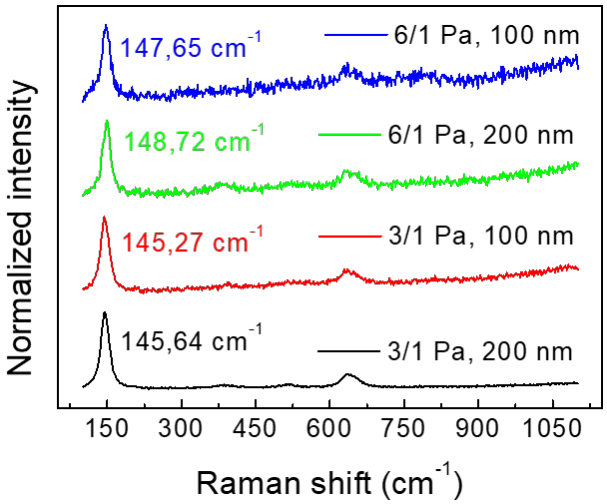

Figure 4.6: *Raman spectra of the TaTO10% multilayers deposited at 3/1 Pa and 6/1 Pa in pure oxygen atmosphere.*

The spectra exhibit the same trend of the counterpart with TaTO5%: (i) 3/1 Pa multilayers are less noisier than the 6/1 Pa ones due to the absence of the amorphous layers (6 Pa); (ii) thinner multilayers show noisier spectra; (iii) the $E_g(1)$ peak of the 6/1 Pa structures is more blue-shifted with respect to the 3/1 Pa ones. The reason has to be found in the presence of the amorphous layers: in the 6/1 Pa structure, such layers give no contribution to the Raman signal, hence the $E_g(1)$ position is given only by the 1 Pa layers. The Raman shift is in accordance with the carrier density relation found by Mazzolini [18]. In the 3/1 Pa structure instead, both the 3 Pa and 1 Pa layers are crystalline, thus they both contribute to the $E_g(1)$ peak position. It has to be noticed that the TaTO10%

6/1 Pa multilayers are much noisier than the TaTO5% ones. A possible reason can be attributed to the fact that the TaTO10% is more defective and it has more difficulties in the crystallization process than the TaTO5% due to the higher Ta content [7].

Electrical properties

The four multilayers show similar values of carrier density, i.e. $n \sim 7 \times 10^{20}\ cm^{-3}$, while for increasing pressure and reduced thickness the resistivity increases and the mobility decreases (see table 4.3). Such trend can be explained by considering two

Deposition parameters					**Electrical properties**		
P (Pa)	d_{nom} (nm)	d_{meas} (nm)	Ta%	F $\left(\frac{J}{cm^2}\right)$	$\rho\ (\Omega cm)$	$n\ \left(\frac{1}{cm^3}\right)$	$\mu\ \left(\frac{cm^2}{Vs}\right)$
3/1	200	176	10	2.73	2.07×10^{-3}	7.82×10^{20}	3.89
3/1	100	90	10	2.73	3.18×10^{-3}	6.87×10^{20}	2.93
6/1	200	154	10	2.73	4.07×10^{-3}	7.16×10^{20}	2.17
6/1	100	73	10	2.73	8.18×10^{-3}	6.72×10^{20}	1.2
1	200	200	10	2.73	9.55×10^{-4}	1.62×10^{21}	4.02
1	100	100	10	2.73	8.22×10^{-4}	1.76×10^{21}	4.3

Table 4.3: *Electrical properties of TaTO10% multilayers deposited at 3/1 and 6/1 Pa in pure oxygen. d_{nom} and d_{meas} stand for the nominal and measured thickness respectively. F is the laser fluence.*

aspects: (i) in thinner samples, surface scattering is more relevant and more defects are present in the films (confirmed by noisier Raman spectra); (ii) the presence of amorphous layers hinder the electrons movement causing in lower mobility and higher resistivity. Except for the 6/1 Pa 100 nm thick multilayers, each one of them outperform their TaTO5% counterpart in carrier density and resitivity, but not in mobility. The reason has to be attributed to the higher Ta content: if on one hand more Ta results in more conduction electrons (and lower resistivity), on the other it causes more distortion in the lattice and enhanced ionized impurity scattering causing lower mobility. It is important to notice that for TaTO10% the architecture (layers period and pressures) influences more the electrical properties than for TaTO5%. It would seem that TaTO10% has a higher sensitivity to the structure rather than TaTO5%. In fact, the differences for each deposited multilayers are enhanced (see Fig. 4.7).

Optical properties

The optical properties of the four multilayers are depicted in Fig. 4.8. From the transmission and reflectance spectra (see Fig. 4.8a and 4.8b) it can be seen

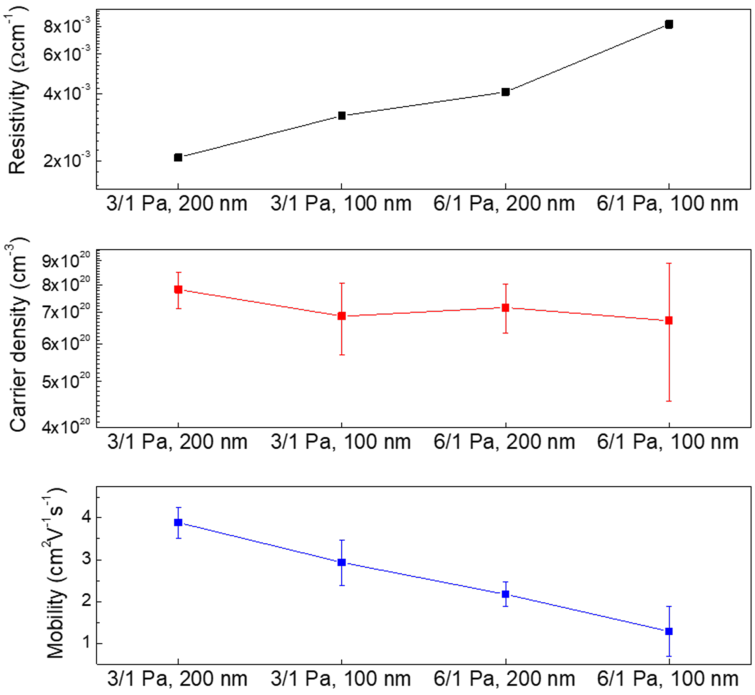

Figure 4.7: *Electrical properties of TaTO10% multilayers deposited at 3/1 and 6/1 Pa in pure oxygen.*

that thicker sample exhibits more interference fringes and lower transmittance, in accordance to the Lamber-Beer law, and higher reflectance. Moreover, 6/1 Pa multilayers shows more transmittance and lower reflectance with respect to the 3/1 Pa ones, due to the presence of the amorphous and porous layers, which ease the transmission of light. The absorption spectra of the four multilayers look almost the same, except for the 6/1 Pa 200 nm thick films, that possesses the highest absorbance approaching the NIR region. Such effect might be related to the 20 nm layers of 6 Pa, that can promote enhanced absorption due to the porous and disordered structure. Furthermore, the 3/1 Pa and 6/1 Pa 200 nm thick films exhibit a decreasing tail in the transmission spectra, possible indication of the plasma frequency in the NIR region. Such behaviour would seem to be in disagreement with [5]. In fact, it has been reported that for AZO/ZnO mulitlayers with increasing layer thickness, the plasma frequency decreases, whereas in the TaTO10% samples it seems to increase. Further analysis and investigation must be performed to assess this hypothesis, since AZO and TaTO are very different materials.

Nevertheless, this is the greatest difference compared to the TaTO5% multilayers, since in the latter, approaching the wavelength of 2000 nm, the transmittivity seems to reach a plateau, hence the plasma frequency should be in the far in-

frared. In conclusion, the effect of the structure is more effective and evident on the TaTO10% rather than the TaTO5% as anticipated in the discussion on the electrical properties.

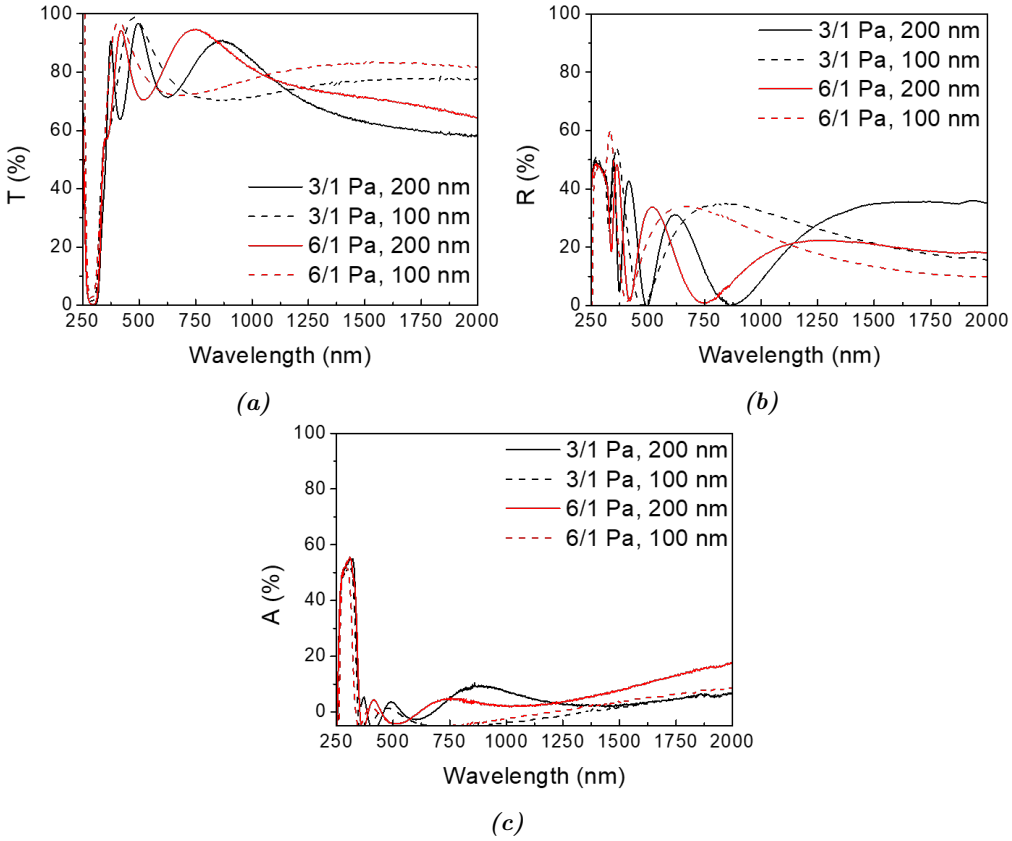

Figure 4.8: *(a) T, (b) R and (c) A of TaTO10% deposited at 3/1 Pa and 6/1 Pa in pure oxygen atmosphere.*

Summarizing, TaTO10% multilayers have been efficiently produced. Crystallization occurs for all the four samples, even for the 100 nm 6/1 Pa which implemented both amorphous layers and 10 nm thick layers of TaTO10%. Raman spectra and optical properties follow the same trend of the TaTO5% samples. Electrical properties display a specific trend, in agreement with the properties of the single component at 1 Pa and the combination with the compact and porous layers. Finally, the modulation of the properties is more effective for TaTO10% than TaTO5%.

4.3 Changing the period

In this part of this thesis work, a new architecture will be presented. In the previous sections, the dielectric layers (3 Pa or 6 Pa) and conductive ones (1 Pa) had the same thickness, 20 nm or 10 nm. Next, I have created a structure in which the thickness of one of the two layer is doubled with respect the other, hence 5 layers of 40 nm were alternated to 5 layers of 20 nm for a total of 10 layers with a period of 60 nm and a total thickness of 300 nm. The pressure has been set to 3/1 Pa in pure oxygen, since these value should give better electric properties (verified for TaTO10% but not for TaTO5%), measured thickness close to the nominal ones and no amorphous component. Both TaTO5%-only and TaTO10%-only multilayers have been produced. For each Ta content, two sample were deposited, one in which the conductive layer is thicker (metal filling content $p = 0.66$) and one in which the dielectric layer is thicker (metal filling content $p = 0.33$), for a total of four samples. The effect of having different layer thickness can be seen on the effective dielectric constant of the films (see Eq. 1.10). Therefore, multilayers with thicker conductive layers should exhibit the plasma frequency and the hyperbolic dispersion closer to the visible region of the spectra, while multilayers with thicker dielectric layers should exhibit those properties in the infrared.

All the analysis were performed on vacuum annealed samples. In order to simplify and shorten the notation, I will call the sample with thicker conductive layer C-TaTO5% and C-TaTO10%, conversely D-TaTO5% and D-TaTO10% the ones with thicker dielectric layer. The pressure will be omitted since only 3/1 Pa has been employed for these films.

SEM analysis of morphology

SEM images reveal compact structure for all the four samples, as expected for a 3/1 Pa pressure. No marked interfaces are visible between each layer, in accordance with the previous deposited multilayers at the same pressure range. No differences can be observed between the TaTO5% or the TaTO10% multilayers. The measured thickness of these sample is a little lower with respect the nominal one, around 270 nm (precise values can be found in table 4.4).

Raman analysis

All Raman spectra display the $E_g(1)$ peak, thus all the samples have crystallized into anatase (see Fig. 4.10a). The two structures made of TaTO10% show a bigger difference among the $E_g(1)$ peaks than the counterparts of TaTO5% ($\sim 4\ cm^{-1}$ and $\sim 1.4\ cm^{-1}$). This is another indication that the TaTO10% is more sensitive to structural modification than TaTO5%.

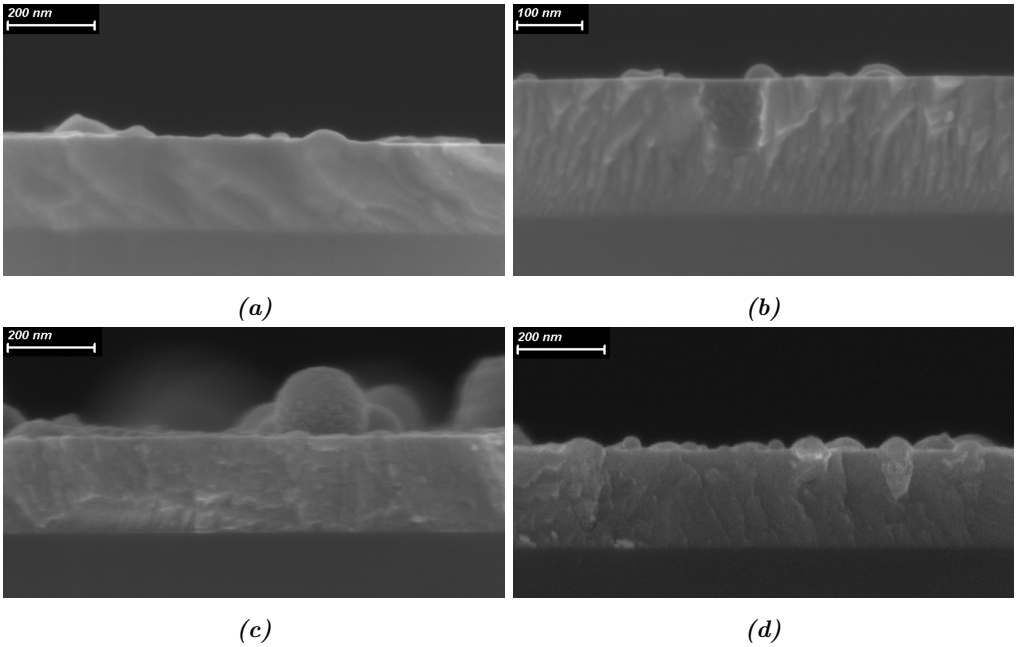

Figure 4.9: *SEM images of (a) D-TaTO10%, (b) C-TaTO10%, (c) D-TaTO5% and (d) C-TaTO5% deposited at 3/1 Pa in pure oxygen atmosphere.*

Peak deconvolution was possible only on D-TaTO10% and C-TaTO10% films (see Fig. 4.10b and 4.10c). The peaks positions reveal the two distinct contribution of the layer deposited at 3 Pa and 1 Pa, respectively at $\sim$ 141 cm^{-1} and $\sim$ 150 cm^{-1}. These value are in agreement with the $E_g(1)$ position of individual films of TaTO10% deposited at 3 Pa and 1 Pa (see section 3.2 and 3.1). The difference in intensity is associated to the higher content of one of the two components in the film. Deconvolution on the TaTO5% films was tried, but unreliable results were obtained. Moreover, for the C-TaTO5% and D-TaTO5%, a strange behaviour of the $E_g(1)$ peak can be observed. The former sample has thicker conductive layers, hence should exhibit a more blue-shifted peak with respect to the latter, but from the Raman spectra in Fig. 4.10a the opposite can be observed. Furthermore, the electrical analysis confirm that C-TaTO5% has higher carrier density than D-TaTO5%, making the interpretation of such spectra more difficult (results in table 4.4). A possible explanation can be given based on the Ta diffusion: in the C-TaTO5%, there can be diffusion from the thicker layers at 1 Pa to the thinner ones at 3 Pa, thus the localization of the carrier density is spread over the whole film and the Raman signal appears red-shifted. On the contrary, in the D-TaTO5% such effect is less pronounced, due to the thinner conductive layers and the thicker dielectric ones, which hinder the diffusion. Thus, the electrons remain more localized, inside the 1 Pa layers, hence the contribution to the Raman signal

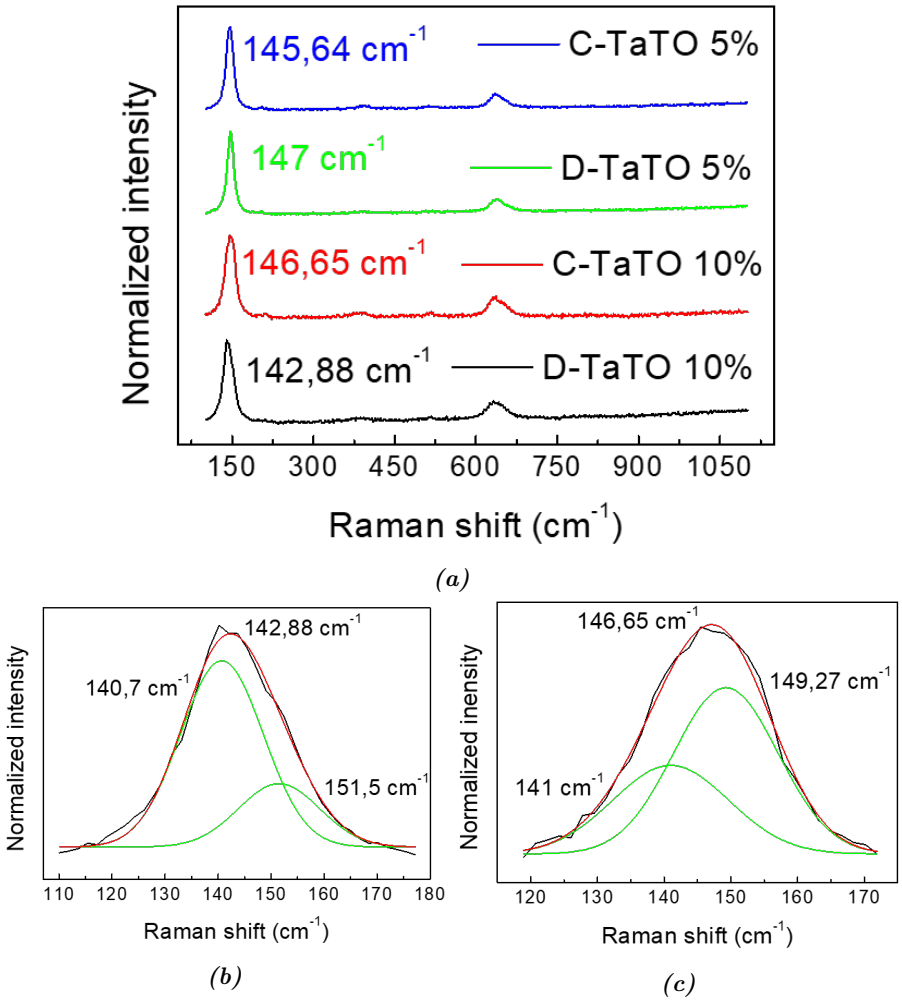

Figure 4.10: *(a) Raman spectra of the new architecture multilayers of TaTO10% and TaTO5% deposited at 3/1 Pa in pure oxygen atmosphere. Peak deconvolution of (b) D-TaTO10% and (c) C-TaTO10%*

of these layer can contributed to blue-shift of the $E_g(1)$ peak. Such explanation does not pretend to be the right one and must be confirmed by other analysis.

Electrical properties

As expected, the multilayers with thicker conductive layers show better properties, but the improvement is more evident for the TaTO10% films with respect to TaTO5% (see Fig. 4.11). This is another proof that the former material responds much more to structural modification compared to the latter. In particular, TaTO10% films possess higher values of n than the TaTO5% counterparts, but lower mobility, as excepted from an higher dopant concentration. Regarding the resistivity, the lowest value is achieved by C-TaTO10%, whereas D-TaTO10% dis-

plays the highest one (see table 4.4).

Deposition parameters				Electrical properties		
Name	d_{th} (nm)	d_{emp} (nm)	F $\left(\frac{J}{cm^2}\right)$	ρ (Ωcm)	n $\left(\frac{1}{cm^3}\right)$	μ $\left(\frac{cm^2}{Vs}\right)$
D-TaTO10%	300	272	2.73	4.46×10^{-3}	4.6×10^{20}	3.1
C-TaTO10%	300	261	2.73	1.11×10^{-3}	1.29×10^{21}	4.38
D-TaTO5%	300	272	2.2	3.88×10^{-3}	3.35×10^{20}	4.85
C-TaTO5%	300	271	2.2	3.03×10^{-3}	4.2×10^{20}	4.91

Table 4.4: *Electrical properties of the new architecture multilayers of TaTO10% and TaTO5% deposited at 3/1 Pa in pure oxygen. d_{th} and d_{emp} stand for the nominal and measured thickness respectively. F is the laser fluence.*

By recalling the properties of a 200 nm thick multilayers of TaTO10% deposited at 3/1 Pa with single layers of equal thickness (20 nm) ($\rho = 2.07 \times 10^{-3}$ Ωcm, $n = 7.82 \times 10^{20}$ cm^{-3}, $\mu = 3.89$ $cm^2V^{-1}s^{-1}$, see table 4.3), it can be seen how in the C-TaTO10% all the properties improve, while in the D-TaTO10% they worsen, as expected. Such trend is in agreement with the structural modification implemented in these mulitlayers. In fact, increasing the metal filling content p, the multilayers gain more metallic behaviour.

Focusing on the TaTO5%, the same statement can not be done. The properties of a 200 nm thick multilayers of TaTO5% deposited at 3/1 Pa with single layers of equal thickness (20 nm) do not fit between the C-TaTO5% and the D-TaTO5%. The former sample shows the lowest mobility ($\mu = 3.36$ $cm^2V^{-1}s^{-1}$) and the highest resistivity ($\rho = 6.07 \times 10^{-3}$) among these three samples, while the carrier denisty ($n = 4.2 \times 10^{20}$ cm^{-3}) is the same of C-TaTO10%. Such behaviour is difficult to understand, hence more analysis should be performed.

Comparing the C-TaTO10% with a TaTO10% film of 200 nm deposited at 1 Pa in pure oxygen ($\rho = 9.55 \times 10^{-4}$ Ωcm, $n = 1.62 \times 10^{21}$ cm^{-3}, $\mu = 4.02$ $cm^2V^{-1}s^{-1}$), it can be noticed small differences between the electrical properties of the two films. The same cannot be said for C-TaTO5% and a TaTO5% film of 200 nm deposited at 1 Pa in pure oxygen ($\rho = 7.26 \times 10^{-4}$ Ωcm, $n = 9.2 \times 10^{20}$ cm^{-3}, $\mu = 8.36$ $cm^2V^{-1}s^{-1}$). The former samples possesses worse properties than the latter.

Optical properties

The optical properties of these multilayers are reported in Fig. 4.12. Since the samples have almost the same thickness, they show the same interference fringes in all the three spectra. A clear trend is evident in T spectra (Fig. 4.12a): more Ta content and thicker conductive layers result in lower transmittance. In particular, the C-TaTO10% has the lowest T at 2000 nm, possible indication of the plasma

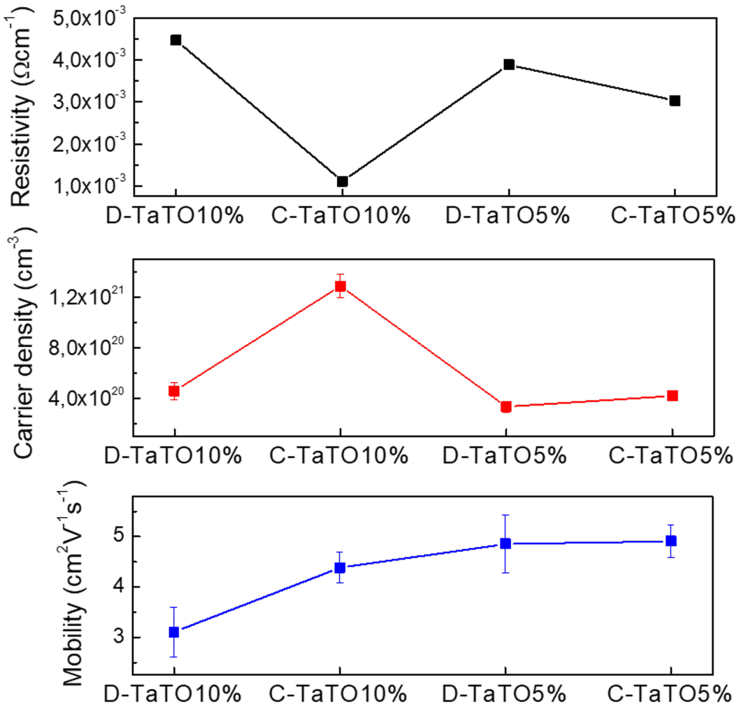

Figure 4.11: *Electrical properties of the new architecture multilayers of TaTO10% and TaTO5% deposited at 3/1 Pa in pure oxygen.*

frequency in the NIR region. Such behaviour is in disagreement with what reported in [5] for AZO/ZnO multilayers. In this work, it was found that increasing the AZO content in the period (thickness of AZO layer + ZnO layer) leads to a decrease in the plasma frequency. From the optical analysis it would seem that C-TaTO10%, which has a higher content of conductive layer in the period, exhibits the plasma frequency at shorter wavelength with respect to D-TaTO10%. Further analysis have to be performed to confirm such evidence. Reflectance is almost equal for the TaTO10% samples, whereas in the C-TaTO5% it is a little bit higher than the D-TaTO5% (see Fig. 4.12b). In the absorption spectra (see Fig. 4.12c), it can be seen how the C-TaTO10% presents the highest value. Combined with the T spectra, it can be assessed that this behaviour is associated to the high carrier density, corresponding to plasmonic response. Also in this case, the optical properties of the TaTO10% change much more with respect the TaTO5%, confirming that the structural modification have more influence on the former material rather then on the latter.

In this section, the properties of the new architecture were presented. TaTO10% confirms to be the right material to obtain considerable modification both in electrical and optical properties as a function of geometry. Moreover, D-TaTO10%,

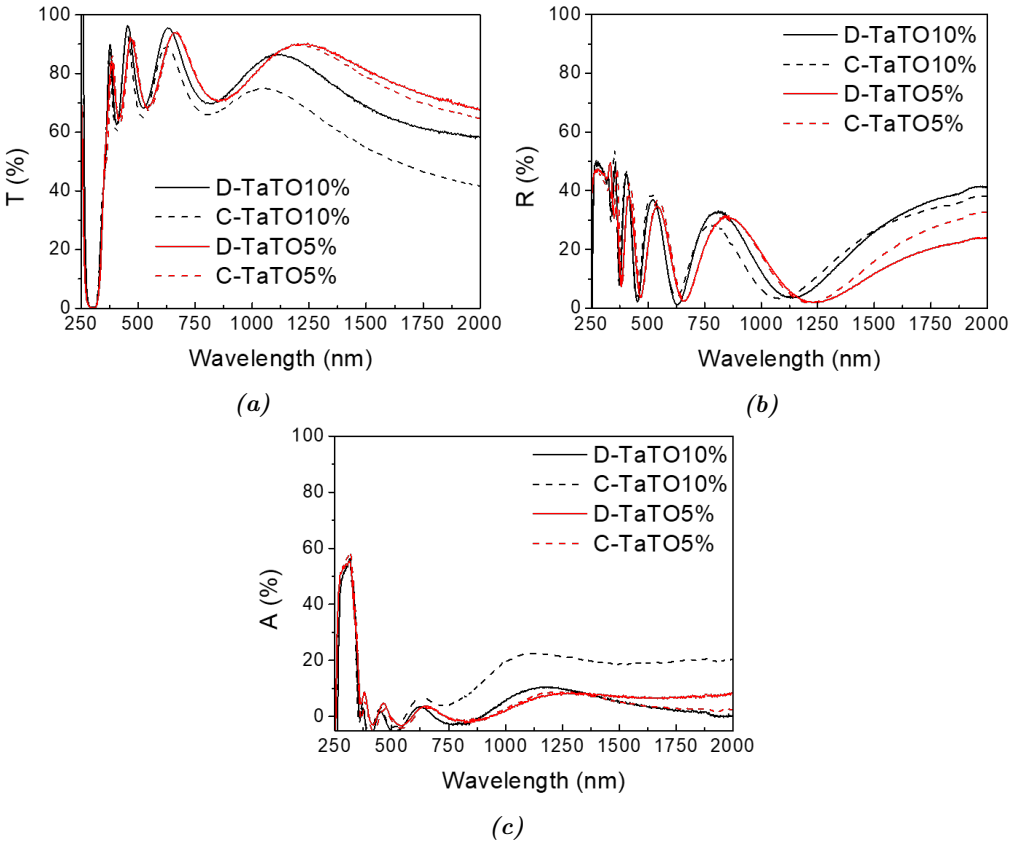

Figure 4.12: *(a) T, (b) R and (c) A of the new architecture multilayers of TaTO10% and TaTO5% deposited at 3/1 Pa in pure oxygen atmosphere.*

C-TaTO10% properties are consistent with the one of a 200 nm thick multilayers of TaTO10% deposited at 3/1 Pa with layers of equal thickness.

On the contrary, D-TaTO5% and C-TaTO5% possess almost the same optical and electrical properties, suggesting that TaTO5% is not sensible to structural modification. Raman spectra of these structure are of difficult interpretation, since the $E_g(1)$ peaks do not follow the expected relationship with the measured carrier density.

4.4 Changing the gas mixture

In section 3.2.1 the properties of a TaTO5% film deposited at 3 Pa in a mixed background atmosphere, namely Ar:O_2=5:1, were presented. The sample was compact, crystalline and conductive ($\rho = 4.84 \times 10^{-3}\ \Omega cm$, $n = 6.19 \times 10^{20}\ cm^{-3}$ and $\mu = 2.46\ cm^2V^{-1}s{-}1$), but with much more defects compared to a sample deposited at 1 Pa in pure oxygen. In the attempt to realize a multilayers (and maybe a HMM) fully conductive, 5 layers at this particular pressure (3 Pa in

mixed atmosphere) were alternated to 5 layers at 1 Pa in pure oxygen. The single layer thickness was set equal for the two deposition pressure, and only TaTO5% was used. Two sample were deposited, one with 20 nm thick layer, for a nominal thickness of 200 nm, and the other with 10 nm thick layers, for a nominal thickness of 100 nm.

All the analysis were performed after the vacuum annealing. In order to simplify the notation and the comparison with the other samples, I will refer to these multilayers as TaTO5% 3/1 Pa m.a. (mixed atmosphere), even though only the layers at 3 Pa were deposited in a mixed atmosphere, while the 1 Pa layers were deposited in pure oxygen. In order to emphasize the obtained data and to provide a better comparison, all the 3/1 Pa multilayers with single layers of same thickness deposited in this thesis work will be presented in the following section.

SEM analysis of morphology

The cross section images acquired at SEM reveal a compact structure as expected from the morphology of the single components. Like the other multilayers deposited at 3/1 Pa, it is not possible to discern the single layers, hence a continuity in the crystal structure can be assumed. The measured thickness of these multilayers is slightly lower the nominal one, 186 nm and 90 nm for the thicker and thinner samples respectively. Such behaviour was observed in all the samples deposited at 3/1 Pa, except for the TaTO5% mulitlayers with layers of equal thickness (see section 4.1).

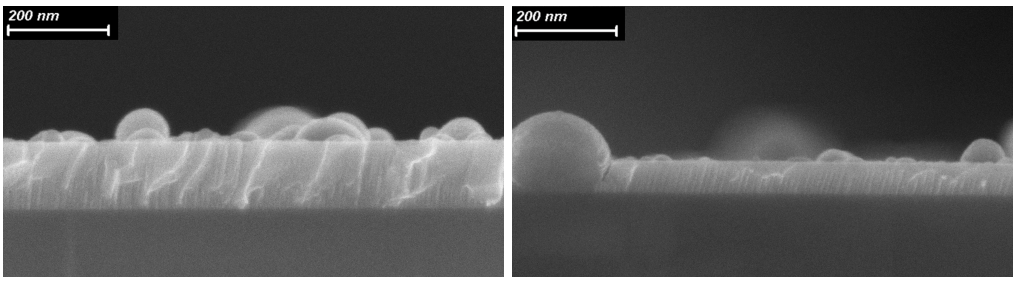

(a) *(b)*

Figure 4.13: *SEM images of the TaTO5% multilayers deposited at 3/1 Pa in mixed atmosphere: (a) the thicker sample (200 nm), (b) the thinner one (100 nm).*

Raman analysis

The Raman spectra confirm that a full crystallization has occurred for both samples. The $E_g(1)$ peak is more blue-shifted with respect the other 3/1 Pa multilayers of same total thickness, confirming that more conductive films have been deposited

effectively. Moreover, the noisier spectra of TaTO5% 3/1 Pa m.a. films with respect to the TaTO5% 3/1 Pa multilayers can be related to the layers deposited at 3 Pa in Ar:O_2, which have been proved to be more defective. The blue-shift is more pronounced for the thicker structure than the 100 nm thick film, since in thinner layers the surface effects become more significant.

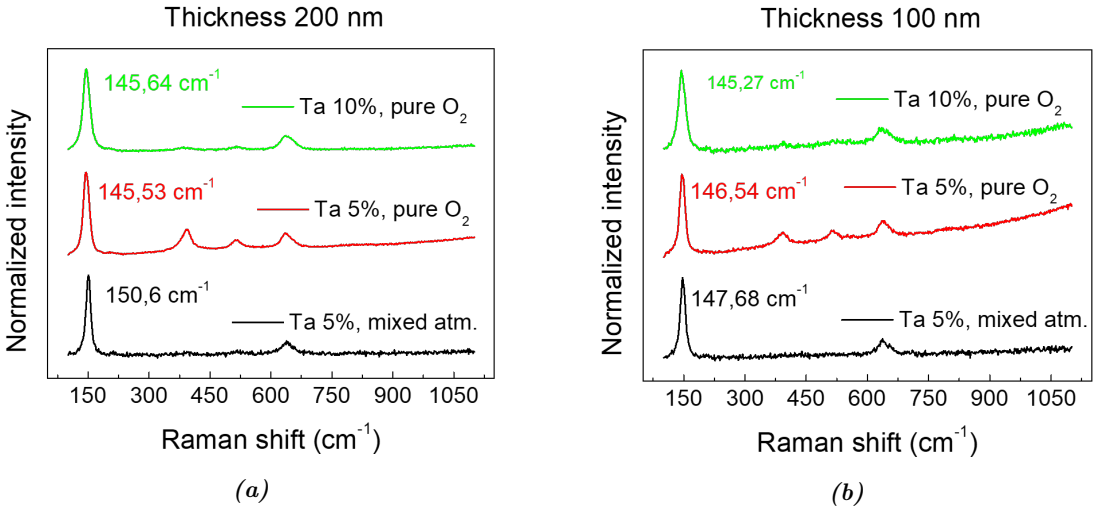

Figure 4.14: *Raman spectra of all the 3/1 Pa multilayers deposited in this thesis work: (a) 3/1 Pa, thicker sample (200 nm), (b) 3/1 Pa, thinner one (100 nm).*

Electrical properties

The two films of TaTO5% 3/1 Pa m.a. exhibit really good properties, outperforming the counterparts with different deposition parameters, in resistivity, carrier density and mobility (see table 4.5). It should not be surprising, since in the former samples the layers deposited at 3 Pa in mixed atmosphere are conductive, whereas the layers at 3 Pa in pure oxygen resulted insulating, for both TaTO5% and TaTO10%. Indeed, it looks like that fully conductive multilayers have been successfully produced. These values are very similar to the ones of 200 nm ($\rho = 7.4 \times 10^{-4}\ \Omega cm$, $n = 9.2 \times 10^{20}\ cm^{-3}$ and $\mu = 8.3\ cm^2V^{-1}s^{-1}$) and 100 nm ($\rho = 1 \times 10^{-3}\ \Omega cm$, $n = 9.86 \times 10^{20}\ cm^{-3}$ and $\mu = 3\ cm^2V^{-1}s^{-1}$) films of TaTO5% deposited at 1 Pa in pure oxygen. Hence, it is probable that the TaTO5% 3/1 m.a. films behave as the latter sample, rather than multilayers.

Such hypothesis should be confirmed possibly with ellipsometric measurements, by checking that the dielectric function of these multilayers is almost the same of a TaTO5% film deposited at 1 Pa O_2.

Deposition parameters					Electrical properties		
Gas	d_{th} (nm)	d_{emp} (nm)	Ta%	F $\left(\frac{J}{cm^2}\right)$	ρ (Ωcm)	n $\left(\frac{1}{cm^3}\right)$	μ $\left(\frac{cm^2}{Vs}\right)$
Ar:O_2/O_2	200	186	5	2.2	8.05×10^{-4}	9.87×10^{20}	7.91
Ar:O_2/O_2	100	90	5	2.2	2.18×10^{-3}	8.06×10^{20}	3.57
O_2	200	208	5	2.2	6.07×10^{-3}	4.2×10^{20}	3.36
O_2	100	103	5	2.2	5.97×10^{-3}	5.98×10^{20}	1.86
O_2	200	176	10	2.73	2.07×10^{-3}	7.82×10^{20}	3.88
O_2	100	90	10	2.73	3.18×10^{-3}	6.87×10^{20}	2.93

Table 4.5: *Electrical properties of 3/1 Pa multilayers deposited at different Ta content and different background atmosphere. d_{th} and d_{emp} stand for the nominal and measured thickness respectively. F is the laser fluence.*

Optical properties

The optical properties of the TaTO5% 3/1 Pa m.a. are reported in figure 4.15 with the other 3/1 Pa multilayers deposited in this thesis work. On the left column there are the T, R, A spectra of the 200 nm multilayers, while on the right there are the thinner ones (100 nm).

The thinner films (on the right column) do not show any relevant differences in all the three spectra. The slightly higher absorption associated to a lower reflectance of the TaTO5% 3/1 Pa m.a film can be caused by the higher carrier density of such films. Conversely, focusing on the 200 nm films, while the T spectra look almost the same, the differences in R and A spectra are more pronounced. In fact, not only the carrier density of the thicker TaTO5% 3/1 Pa m.a sample is higher, but the films is fully conductive too, thus free carrier absorption is enhanced with respect to multilayers with dielectric layers.

Lastly, a comparison between the TaTO5% 3/1 Pa m.a multilayers with a TaTO5% films deposited at 1 Pa in pure O_2 (taken from [7]) is reported in Fig. 4.16. The T spectra look almost identical, whereas the relfectance of the former is a little higher associated to a little lower absorbance with respect the latter. Hence, the multilayers behave as TaTO5% films deposited at 1 Pa in pure oxygen and the hyperbolic regime is not expected.

In this section, the attempt of creating a fully conductive multilayers was investigated. At a first glance, from the Raman spectra and the electrical analysis it would seem to have obtained the desired films. However, the optical properties resemble too much the one of TaTO5% films deposited at 1 Pa in pure oxygen, with the same total thickness. Thus, such TaTO5% 3/1 Pa m.a. films are expected to behave as a homogeneous films rather than a multilayers and they should not

display the hyperbolic regime.

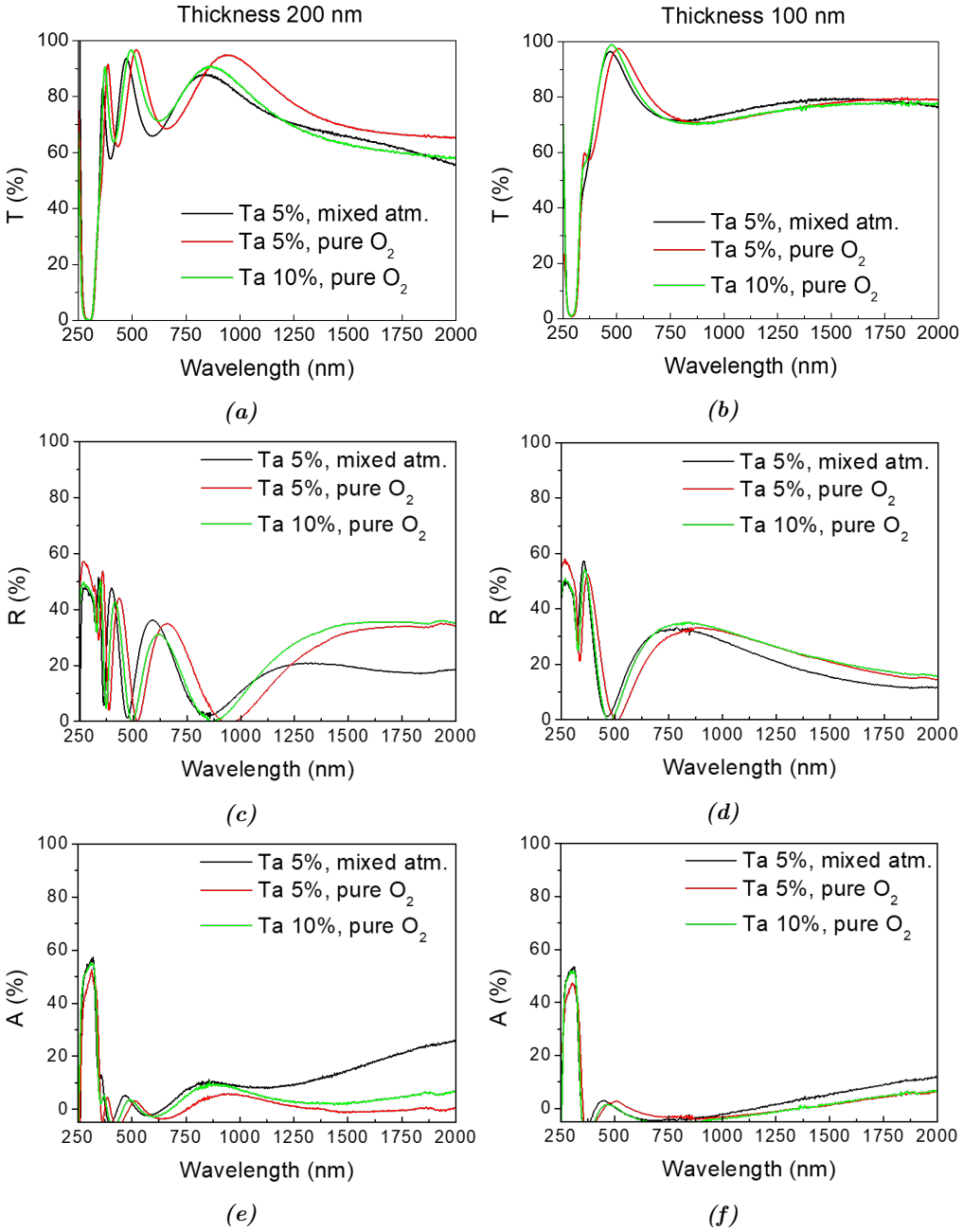

Figure 4.15: *T spectra of (a) 200 nm and (b) 100 nm 3/1 Pa multilayers deposited at different Ta content and different background atmosphere. R spectra of (c) 200 nm and (d) 100 nm 3/1 Pa multilayers deposited at different Ta content and different background atmosphere. A spectra of (e) 200 nm and (f) 100 nm 3/1 Pa multilayers deposited at different Ta content and different background atmosphere.*

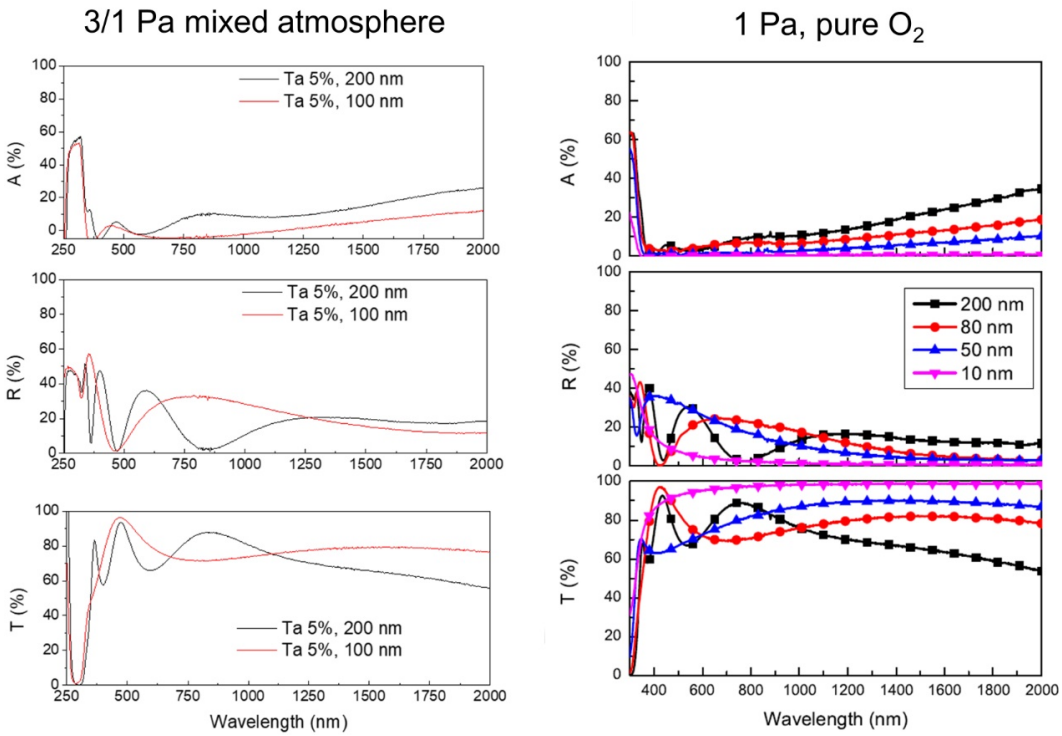

Figure 4.16: *Comparison between the optical properties of TaTO5% 3/1 Pa m.a (left) and TaTO5% deposited at 1 Pa inpure oxygen (right).*

Chapter 5

Conclusion and perspectives

This thesis work explored the synthesis and characterization of TaTO-only multilayers via Pulsed Laser Deposition (PLD) in view of application as Hyperbolic Metamaterial (HMM) in the mid infrared spectral range. This work focused on the characterization of the morphology, the crystalline structure, the electrical and optical properties in the Vis-NIR range. Particularly, the effects of pressure, dopant concentration and geometrical parameters were studied, in order to understand and optimize the deposition parameters for the future HMM.

In order to fully understand the properties exhibited by multilayers, it was necessary to learn the behaviour of the single components and reveal their properties. Pulsed lased deposited TaTO5% was deeply studied by Mazzolini [17]–[20], Ornago [7] and Gaetani [8]. In particular, the effects of the film thickness and the deposition pressure on the overall properties (morphology, crystalline structure, electrical and optical) of TaTO5% films were object of thorough investigation. Therefore, in this work I analyzed only two particular deposition pressure values for TaTO5%, that were not discussed in the aforementioned works. First, TaTO5% was deposited at 6 Pa in pure oxygen atmosphere and then vacuum annealed. The film resulted porous, amorphous and non-conductive. Later, TaTO5% was deposited at 3 Pa in a mixed background atmosphere, composed by Ar and O_2 in proportion 5 to 1. The aim was to achieve a conductive films, but with different dielectric function with respect to film deposited at 1 Pa in pure O_2. The final goal was to create a multilayers (and hopefully a HMM) fully conductive, by alternating layers at 1 Pa in pure O_2 and layers at 3 Pa in mixed atmosphere. After the vacuum annealing, the film deposited at 3 Pa in mixed atmosphere exhibited a compact, more defective and crystalline structure. Electrical characterization confirmed the conductive behaviour of such film ($\rho = 4.84 \times 10^{-3}\ \Omega cm$, $n = 6.19 \times 10^{20}\ cm^{-3}$ and $\mu = 2.46\ cm^2V^{-1}s^{-1}$).

TaTO10% was not object of a thorough study as TaTO5%, therefore I had to

deposit several samples. First, thin layers (20 nm, 10 nm, 5 nm) were deposited at 1 Pa in pure O_2 on glass substrate. This step was necessary to understand if thin TaTO10% could be used as metallic component in multilayers. After vacuum annealing, only the 20 nm thick film crystallized and showed conductive behaviour, whereas the 10 nm and 5 nm thick layer turned out to be insulating due to several possible reasons (non-interconnected film, enhanced surface scattering...). The same three layers (20 nm, 10 nm, 5 nm) were deposited on stoichiometric titania substrate (50 nm thick). Depositing on a lattice matched polycrystalline substrate should help the crystallization process, giving in return better electrical properties. Indeed, these three layers turned out to be conductive (only the 5 nm thick film showed poor electrical properties) after vacuum annealing, hence a partial crystallization had occurred. Moreover, these bilayers outperformed the counterparts deposited on glass substrate and the TaTO5% counterparts deposited on titania substrate by Gaetani in his thesis work [8]. It would seem that TaTO10% wets better the titania substrate or it does not generate the dead layer (thin insulating layer arising at the interface) due to the higher Ta content. TaTO10% bilayers could be efficiently used as transparent electrodes in solar cells. Furthermore, multilayers of TaTO10% and stoichiometric TiO_2 could be of great interest as HMM.

Later, the effect of higher deposition pressures on TaTO10% was studied too. The film deposited at 3 Pa in pure oxygen exhibited compact and crystalline structure after vacuum annealing, but was not conductive. On the contrary, the film deposited at 6 Pa in pure O_2 turned out to be amorphous, porous and non-conductive after the vacuum annealing. As expected from the porous and amorphous structure, the 6 Pa film displayed higher transmittance and absorbance than the compact 3 Pa film.

Finally, the TaTO-only multilayers were deposited. The metallic component corresponded to layers deposited at 1 Pa in pure oxygen, whereas the dielectric one was obtained by increasing the pressure (3 Pa or 6 Pa). By exploiting this feature, multilayers (and possibly HMMs) can be obtained in a single step deposition, without opening the vacuum chamber, thus drastically reducing the operation time.

First, TaTO5%-only multilayers were deposited at 3/1 Pa and 6/1 Pa in pure oxygen atmosphere. The structure was composed by 10 layers of same thickness, hence with metal filling content $p = 0.5$. The single layer thickness was set to 20 nm (period 40 nm, nominal thickness 200 nm) and 10 nm (period 20 nm, nominal thickness 100 nm) for a total of four structures. For the 6/1 Pa structure, increasing the period from 20 nm to 40 nm resulted in better effective electrical properties, whereas no clear trend could be found for the 3/1 Pa ones. Thicker samples displayed lower transmittance and higher reflectance. Increasing the pressure of

the non-conductive layers (from 3 Pa to 6 Pa) resulted in higher transmittance and lower reflectance.

Then, the same four multilayers were deposited with TaTO10%. In this case, reducing the period thickness (from 40 nm to 20 nm) and increasing the pressure (from 3 Pa to 6 Pa) resulted in worse electrical properties. The trend found in the optical properties for the TaTO5%-only multilayers, were found for the TaTO10%-only multilayers as well. However, the tail of the absorption spectra was increasing toward 2000 nm, thus it can be seen the start of the free carrier absorption, sign of the plasmonic response. This is not unexpected, since the Ta content was doubled.

Later, new architectures were implemented. The metal filling content p was set to 0.33 and 0.66 (5 periods of 60 nm), which corresponded to metallic layers of halved and doubled thickness with respect to the dielectric ones, respectively. The pressure was set to 3/1 Pa in pure oxygen and both TaTO5%-only and TaTO10%-only multilayers were deposited. Increasing p resulted in better electrical properties, as expected from a more metallic behaviour of the multilayers. However, the improvement was much more pronounced for TaTO10% than TaTO5%. Moreover, multilayers with $p = 0.66$ displayed lower transmittance compared to films with $p = 0.33$.

Lastly, fully conductive multilayers were deposited. To do that, layers deposited at 1 Pa in pure oxygen were alternated to layers deposited at 3 Pa in mixed atmosphere (Ar:O_2=5:1). Only TaTO5% structures were implemented. The period was set to 40 nm and 20 nm (nominal thickness 200 nm and 100 nm, respectively) with metal filling content $p = 0.5$. The deposited multilayers resembled very much films of same thickness (200 nm and 100 nm) of TaTO5% deposited at 1 Pa in pure O_2, both in the electrical and optical properties. Therefore, the hyperbolic regime is not expected.

The main results of this thesis work are reported below:

- a stoichiometric titania substrate was optimal for achieving good electrical properties of TaTO10% thin films down to 10 nm.
- TaTO5% multilayers with $p = 0.5$: increasing the period results in lower transmittance and higher reflectance. Only the 6/1 Pa structures exhibit better electrical properties for thicker period.
- TaTO10% multilayers with $p = 0.5$: increasing the period and lowering the pressure (3/1 Pa instead of 6/1 Pa) resulted in better electrical properties. Increasing the period results in lower transmittance and higher reflectance. Higher absorbance is displayed with respect the TaTO5% multilayers.
- Multilayers with $p = 0.33$ and $p = 0.66$: the increasing metallic content is beneficial for the electrical properties, but not for the transmittance. The

differences in both electrical and optical properties between the $p = 0.33$ and $p = 0.66$ structures are more enhanced for TaTO10%. Therefore, TaTO10% would seem to be more sensitive to structural and geometrical modifications.

The entirety of this work was devoted to a first understanding of TaTO-only multilayers as possible HMM in the infrared. Since the instrumental setup at our disposal did not allowed to reach this frequency range, this work focused on the structural, morphological, electrical and optical characterization. More architectures need to be implemented in order to fully comprehend the geometry effects on the plasmonic response of such films. For example, the effect of the number of periods was not explored, since all the multilayers were composed of 5 periods (10 layers). TiO_2 can be implemented as the dielectric component and see if differences in electrical and optical properties arise. Furthermore, since ellipsometric measurements are able to extract the dielectric function, they must be performed in order to find the hyperbolic regime, if present. Such analysis would be of extremely importance in order to make a suitable comparison with the HMMs reported in literature. In addition, the modeling of the reflectance and transmittance spectra measured in this work can be implemented, in order to extract the dielectric function in a second moment. Lastly, multilayers made of TCO and metals can be explored. This peculiar choice can ensure a fully conductive multilayer and a hyperbolic dispersion relation in Vis-NIR. In fact, TCOs exhibit a positive ε_r in the Vis, whereas metals display a negative one. Therefore, the right combination of TCOs and metals has to be found in order to respect the impedance matching and to achieve the hyperbolic regime.

Bibliography

[1] S. A. Maier, *Plasmonics: Fundamentals and Applications*. Springer Science & Business Media, 2007 (cit. on pp. 1, 5–9).

[2] G. V. Naik, J. Liu, A. V. Kildishev, V. M. Shalaev, and A. Boltasseva, "Demonstration of Al:ZnO as a plasmonic component for near-infrared metamaterials," *Proceedings of the National Academy of Sciences*, vol. 109, no. 23, pp. 8834–8838, 2012 (cit. on pp. 2, 20).

[3] C. T. Riley, J. S. Smalley, K. W. Post, D. N. Basov, Y. Fainman, D. Wang, Z. Liu, and D. J. Sirbuly, "High-quality, ultraconformal aluminum-doped zinc oxide nanoplasmonic and hyperbolic metamaterials," *Small*, vol. 12, no. 7, pp. 892–901, 2016 (cit. on pp. 2, 20).

[4] P. Kelly, M. Liu, and L. Kuznetsova, "Designing optical metamaterial with hyperbolic dispersion based on an Al:ZnO/ZnO nano-layered structure using the atomic layer deposition technique," *Applied optics*, vol. 55, no. 11, pp. 2993–2997, 2016 (cit. on pp. 2, 20).

[5] P. Kelly, W. Zhang, M. Liu, and L. Kuznetsova, "Engineering the structural, plasmonic, and optical properties of multilayered aluminum-doped zinc oxide metamaterial grown by pulsed laser deposition," *Applied Optics*, vol. 58, no. 21, pp. 5681–5686, 2019 (cit. on pp. 2, 20, 55, 61).

[6] P. Guo, B. T. Diroll, W. Huang, L. Zeng, B. Wang, M. J. Bedzyk, A. Facchetti, T. J. Marks, R. P. Chang, and R. D. Schaller, "Low-loss near-infrared hyperbolic metamaterials with epitaxial ITO-In_2O_3 multilayers," *ACS Photonics*, vol. 5, no. 5, pp. 2000–2007, 2018 (cit. on pp. 2, 20).

[7] L. Ornago, "Synthesis of tantalum-doped titanium oxide thin films: a bridge to infrared plasmonics," Master's thesis, Politecnico di Milano, 2018 (cit. on pp. 2, 9, 14, 36, 41, 43, 44, 49, 54, 65, 69).

[8] F. Gaetani, "Development of tantalum-doped titanium oxide nanostructures for plasmonic applications," Master's thesis, Politecnico di Milano, 2019 (cit. on pp. 2, 9, 14, 24, 36, 37, 41, 43, 44, 69, 70).

[9] D. Pines and D. Bohm, "A collective description of electron interactions: II. Collective vs individual particle aspects of the interactions," *Physical review*, vol. 85, no. 2, pp. 338–353, 1952 (cit. on p. 5).

[10] G. V. Naik, V. M. Shalaev, and A. Boltasseva, "Alternative plasmonic materials: beyond gold and silver," *Advanced Materials*, vol. 25, no. 24, pp. 3264–3294, 2013 (cit. on pp. 5, 9).

[11] N. W. Ashcroft and N. Mermin, *Solid state physics*. Saunders College, 1976 (cit. on pp. 5, 6).

[12] L. Solymar and E. Shamonina, *Waves in Metamaterials*. Oxford University Press, 2009 (cit. on p. 7).

[13] S. Pillai and M. A. Green, "Comprehensive renewable energy: Photovoltaic solar energy," in. Elsevier, 2012, ch. Plasmonics for Photovoltaics (cit. on p. 7).

[14] Z. Zalevsky and I. Abdulhalim, "Integrated nanophotonic devices," in. Elsevier, 2014, ch. Plasmonics (cit. on p. 8).

[15] D. S. Ginley, H. Hosono, and D. C. Paine, *Handbook of transparent conductors*. Springer, 2010 (cit. on pp. 9, 11, 12).

[16] Z. Wang, C. Chen, K. Wu, H. Chong, and H. Ye, "Transparent conductive oxides and their applications in near infrared plasmonics," *Physica Status Solidi (a)*, vol. 216, no. 5, p. 1 700 794, 2019 (cit. on p. 9).

[17] P. Mazzolini, P. Gondoni, V. Russo, D. Chrastina, C. S. Casari, and A. Li Bassi, "Tuning of electrical and optical properties of highly conducting and transparent Ta-doped TiO_2 polycrystalline films," *The Journal of Physical Chemistry C*, vol. 119, no. 13, pp. 6988–6997, 2019 (cit. on pp. 9, 10, 13–15, 41, 69).

[18] P. Mazzolini, V. Russo, C. S. Casari, T. Hitosugi, S. Nakao, T. Hasegawa, and A. Li Bassi, "Vibrational electrical properties relationship in donor doped TiO_2 by raman spectroscopy," *The Journal of Physical Chemistry C*, vol. 120, no. 33, pp. 18 878–18 886, 2016 (cit. on pp. 9, 13, 14, 38, 41, 44, 48, 53, 69).

[19] P. Mazzolini, "Functional properties control of doped TiO_2 for transparent electrodes and photoanodes," PhD thesis, Politecnico di Milano, 2015 (cit. on pp. 9, 13, 15, 69).

[20] P. Mazzolini, T. Acartürk, D. Chrastina, U. Starke, G. Gregori, C. S. Casari, and A. Li Bassi, "Controlling the electrical properties of undoped and Ta-doped TiO_2 polycrystalline films via ultra fast annealing treatments," *Advanced Electronic Materials*, vol. 2, no. 3, p. 1 500 316, 2016 (cit. on pp. 9, 13, 69).

[21] D. C. Qi, A. R. Barman, L. Debbichi, S. Dhar, I. Santoso, T. C. Asmara, H. Omer, K. Yang, P. Krüger, A. T. Wee, T. Venkatesan, and A. Rusydi, "Cationic vacancies and anomalous spectral-weight transfer in $Ti_{1-x}Ta_xO_2$ thin films studied via polarization-dependent near-edge X-ray absorption fine structure spectroscopy," *Physical Review B*, vol. 87, no. 24, p. 245 201, 2013 (cit. on p. 10).

[22] E. Burstein, "Anomalous optical absorption limit in InSb," *Physical Review*, vol. 93, no. 3, p. 632, 1954 (cit. on p. 10).

[23] H. C. Lee and O. O. Park, "Electron scattering mechanisms in indium-tin-oxide thin films: grain boundary and ionized impurity scattering," *Vacuum*, vol. 75, no. 3, pp. 275–282, 2004 (cit. on p. 11).

[24] Y. Zhao, A. Kumar, G. A. Khodaparast, A. Eltahir, H. Wang, and S. Priya, "Sintering temperature-dependent chemical defects and the effect on the electrical resistivity of thermoelectric ZnO," *Energy Harvesting and Systems*, vol. 1, no. 1-2, pp. 113–119, 2014 (cit. on p. 11).

[25] R. G. Gordon, "Criteria for choosing transparent conductors," *MRS bulletin*, vol. 25, no. 8, pp. 52–57, 2000 (cit. on p. 11).

[26] T. J. Coutts, D. L. Young, and X. Li, "Characterization of transparent conducting oxides," *Mrs Bulletin*, vol. 25, no. 8, pp. 58–65, 2000 (cit. on p. 11).

[27] M. Landmann, E. W. G. S. Rauls, and W. G. Schmidt, "The electronic structure and optical response of rutile, anatase and brookite TiO_2," *Journal of physics: condensed matter*, vol. 24, no. 19, p. 195 503, 2012 (cit. on pp. 11, 12).

[28] D. Dorow-Gerspach and M. Wuttig, "Metal-like conductivity in undoped TiO_2: understanding an unconventional transparent conducting oxide," *Thin Solid Films*, vol. 669, pp. 1–7, 2019 (cit. on p. 12).

[29] F. Sauvage, F. D. Fonzo, A. Li Bassi, C. S. Casari, V. Russo, G. Divitini, C. Ducati, C. E. Bottani, P. Comte, and M. Graetzel, "Hierarchical TiO_2 photoanode for dye-sensitized solar cells," *Nano Letters*, vol. 10, no. 7, pp. 2562–2567, 2017 (cit. on p. 12).

[30] M. S. Ahmad, A. K. Pandey, and N. A. Rahim, "Advancements in the development of TiO_2 photoanodes and its fabrication methods for dye sensitized solar cell (DSSC) applications. A review," *Renewable and Sustainable Energy Reviews*, vol. 77, pp. 89–108, 2017 (cit. on p. 12).

[31] L. Mascaretti, S. Ferrulli, P. Mazzolini, C. S. Casari, V. Russo, R. Matarrese, I. Novac, G. Terraneo, N. Liue, P. Schmuki, and A. Li Bassi, "Hydrogen-treated hierarchical titanium oxide nanostructures for photoelectrochemical water splitting," *Solar Energy Materials and Solar Cells*, vol. 169, pp. 19–27, 2017 (cit. on p. 12).

[32] M. G. Walter, E. L. Warren, J. R. McKone, S. W. Boettcher, Q. Mi, E. A. Santori, and N. S. Lewis, "Solar water splitting cells," *Chemical reviews*, vol. 110, no. 11, pp. 6446–6473, 2010 (cit. on p. 12).

[33] Y. Furubayashi, T. Hitosugi, Y. Yamamoto, K. Inaba, G. Kinoda, Y. Hirose, T. Shimada, and T. Hasegawa, "A transparent metal: Nb-doped anatase TiO_2," *Applied Physics Letters*, vol. 86, no. 25, p. 252 101, 2005 (cit. on p. 12).

[34] T. Hitosugi, Y. Furubayashi, A. Ueda, K. Itabashi, K. Inaba, Y. Hirose, G. Kinoda, Y. Yamamoto, T. Shimada, and T. Hasegawa, "Ta-doped anatase TiO_2 epitaxial film as transparent conducting oxide," *Japanese Journal of Applied Physics*, vol. 44, no. 34, pp. 1063–1065, 2005 (cit. on p. 13).

[35] J. Tauc, R. Grigorovici, and A. Vancu, "Optical properties and electronic structure of amorphous germanium," *physica status solidi (b)*, vol. 15, no. 2, pp. 627–637, 1966 (cit. on p. 13).

[36] W. Cai and V. M. Shalev, *Optical Metamaterials: Fundamentals and Applications*. Springer, 2010 (cit. on pp. 15, 17, 21).

[37] R. A. Shelby, D. R. Smith, and S. Schultz, "Experimental verification of a negative index of refraction," *Science*, vol. 292, no. 5514, pp. 77–79, 2001 (cit. on p. 15).

[38] V. G. Velesago, "The electrodynamics of substances with simultaneously negative values of ϵ and μ," *Physics Uspekhi*, vol. 10, no. 4, pp. 509–514, 1968 (cit. on p. 16).

[39] J. B. Pendry, "Negative refraction makes a perfect lens," *Physical review letters*, vol. 85, no. 18, p. 3966, 2000 (cit. on p. 16).

[40] D. R. Smith, W. J. Padilla, D. C. Vier, and S. C. N.-N. S. Schultz, "Composite medium with simultaneously negative permeability and permittivity," *Physical review letters*, vol. 84, no. 18, p. 4184, 2000 (cit. on p. 16).

[41] L. Li, R. E. Simpson, and S. K. Valiyaveedu, "Active hyperbolic metamaterials: Progress, materials and design," *Journal of Optics*, vol. 20, no. 10, p. 103 001, 2018 (cit. on pp. 16, 17, 19, 24).

[42] P. Huo, S. Zhang, Y. Liang, Y. Lu, and T. Xu, "Hyperbolic metamaterials and metasurfaces: Fundamentals and applications," *Advanced Optical Materials*, vol. 7, no. 14, p. 1 801 616, 2019 (cit. on pp. 16, 21, 23).

[43] A. Poddubny, I. Iorsh, P. Belov, and Y. Kivshar, "Hyperbolic metamaterials," *Nature Photonics*, vol. 7, no. 12, p. 948, 2013 (cit. on pp. 16–18, 22).

[44] L. Ferrari, C. Wu, D. Lepage, X. Zhang, and Z. Liu, "Hyperbolic metamaterials and their applications," *Progress in Quantum Electronics*, vol. 40, pp. 1–40, 2015 (cit. on pp. 18, 22, 23).

[45] S. V. Zhukovsky, O. Kidwai, and J. E. Sipe, "Physical nature of volume plasmon polaritons in hyperbolic metamaterials," *Optic Express*, vol. 21, no. 12, pp. 14 982–14 987, 2013 (cit. on p. 19).

[46] Z. Liu, H. Lee, Y. Xiong, C. Sun, and X. Zhang, "Far-field optical hyperlens magnifying sub-diffraction-limited objects," *Science*, vol. 315, no. 5819, p. 1686, 2007 (cit. on pp. 19, 22).

[47] L. Li, W. Wang, T. S. Luk, X. Yang, and J. Gao, "Enhanced quantum dot spontaneous emission with multilayer metamaterial nanostructures," *ACS Photonics*, vol. 4, no. 3, pp. 501–508, 2017 (cit. on pp. 19, 24).

[48] H. N. Krishnamoorthy, Z. Jacob, E. Narimanov, I. Kretzschmar, and V. M. Menon, "Topological transitions in metamaterials," *Science*, vol. 336, no. 6078, pp. 205–209, 2012 (cit. on pp. 19, 24).

[49] J. Rho, Z. Ye, Y. Xiong, X. Yin, Z. Liu, H. Choi, G. Bartal, and X. Zhang, "Spherical hyperlens for two-dimensional sub-diffractional imaging at visible frequencies," *Nature communications*, vol. 1, no. 1, pp. 1–5, 2010 (cit. on pp. 19, 22).

[50] J. Kim, V. P. Drachev, Z. Jacob, G. V. Naik, A. Boltasseva, E. E. Narimanov, and V. M. Shalaev, "Improving the radiative decay rate for dye molecules with hyperbolic metamaterials," *Optics express*, vol. 20, no. 7, pp. 8100–8116, 2012 (cit. on pp. 19, 24).

[51] K. V. Sreekanth, A. De Luca, and G. Strangi, "Experimental demonstration of surface and bulk plasmon polaritons in hypergratings," *Scientific reports*, vol. 3, p. 3291, 2013 (cit. on p. 19).

[52] J. H. Kim, Y.-J. Moon, S.-K. Kim, Y.-Z. Yoo, and T.-Y. Seong, "Al-doped ZnO/Ag/Al-doped ZnO multilayer films with a high figure of merit," *Ceramics International*, vol. 41, no. 10, pp. 14 805–14 810, 2015 (cit. on p. 19).

[53] M. Acosta, J. Mendez-Gamboa, I. Riech, C. Acosta, and M. Zambrano, "AZO/Ag/AZO multilayers electrodes evaluated using a photonic flux density figure of merit for solar cells applications," *Superlattices and Microstructures*, vol. 127, pp. 49–53, 2019 (cit. on p. 19).

[54] D. R. Sahu, S.-Y. Lin, and J.-L. Huang, "Investigation of conductive and transparent Al-doped ZnO/Ag/Al-doped ZnO multilayer coatings by electron beam evaporation," *Thin solid films*, vol. 516, no. 15, pp. 4728–4732, 2008 (cit. on p. 19).

[55] S. H. Oh, S.-M. Lee, and K. C. Choi, "Relationship between surface plasmon and transmittance enhancement in indium-tin-oxide/Ag/indium-tin-oxide multilayer electrodes," *Thin Solid Films*, vol. 520, no. 9, pp. 3605–3608, 2012 (cit. on p. 19).

[56] H. Ferhati and F. Djeffal, "Performance assessment of TCO/metal/TCO multilayer transparent electrodes: From design concept to optimization," *Journal of Computational Electronics*, pp. 1–10, 2020 (cit. on p. 19).

[57] X. Fang, C. L. Mak, J. Dai, K. Li, H. Ye, and C. W. Leung, "ITO/Au/ITO sandwich structure for near-infrared plasmonics," *ACS applied materials & interfaces*, vol. 6, no. 18, pp. 15 743–15 752, 2014 (cit. on p. 19).

[58] K. K. Lam, S. M. Ng, H. F. Wong, L. Fei, Y. Liu, K. H. Chan, H. Ye, C. W. Leung, and C. L. Mak, "Effect of thickness on the optical and electrical properties of ITO/Au/ITO sandwich structures," *ACS Applied Materials & Interfaces*, vol. 12, no. 11, pp. 13 437–13 446, 2020 (cit. on p. 19).

[59] Y. Liu, S. Zhu, and B. Song, "Optical and electrical properties of transparent conductive NTTO/Cu/NTTO multilayer films deposited by magnetron sputtering," *JOM*, vol. 71, no. 10, pp. 3720–3726, 2019 (cit. on p. 20).

[60] C. Chen, Z. Wang, K. Wu, H. Chong, Z. Xu, and H. Ye, "ITO-TiN-ITO sandwiches for near-infrared plasmonic materials," *ACS applied materials & interfaces*, vol. 10, no. 17, pp. 14 886–14 893, 2018 (cit. on p. 20).

[61] D. R. Smith, D. Schurig, J. J. Mock, P. Kolinko, and P. Rye, "Partial focusing of radiation by a slab of indefinite media," *Applied physics letters*, vol. 84, no. 13, pp. 2244–2246, 2004 (cit. on p. 21).

[62] P. Huo, Y. Liang, S. Zhang, Y. Lu, and T. Xu, "Angular optical transparency induced by photonic topological transitions in metamaterials," *Laser & Photonics Reviews*, vol. 12, no. 8, p. 1 700 309, 2018 (cit. on pp. 21, 22).

[63] S. A. Ramakrishna, J. Pendry, M. Wiltshire, and W. Stewart, "Imaging the near field," *Journal of Modern Optics*, vol. 50, no. 9, pp. 1419–1430, 2003 (cit. on p. 22).

[64] Y. Xiong, Z. Liu, and X. Zhang, "Projecting deep-subwavelength patterns from diffraction-limited masks using metal-dielectric multilayers," *Applied physics letters*, vol. 93, no. 11, p. 111 116, 2008 (cit. on p. 23).

[65] T. Xu, Y. Zhao, J. Ma, C. Wang, J. Cui, C. Du, and X. Luo, "Sub-diffraction-limited interference photolithography with metamaterials," *Optics Express*, vol. 16, no. 18, pp. 13 579–13 584, 2008 (cit. on p. 23).

[66] K. Okamoto, I. Niki, A. Shvartser, Y. Narukawa, T. Mukai, and A. Scherer, "Surface-plasmon-enhanced light emitters based on ingan quantum wells," *Nature materials*, vol. 3, no. 9, pp. 601–605, 2004 (cit. on p. 23).

[67] M. Francardi, L. Balet, A. Gerardino, N. Chauvin, D. Bitauld, L. Li, B. Alloing, and A. Fiore, "Enhanced spontaneous emission in a photonic-crystal light-emitting diode," *Applied Physics Letters*, vol. 93, no. 14, p. 143 102, 2008 (cit. on p. 23).

[68] G. Shambat, B. Ellis, A. Majumdar, J. Petykiewicz, M. A. Mayer, T. Sarmiento, J. Harris, E. E. Haller, and J. Vučković, "Ultrafast direct modulation of a single-mode photonic crystal nanocavity light-emitting diode," *Nature communications*, vol. 2, no. 1, pp. 1–6, 2011 (cit. on p. 23).

[69] M. D. Eisaman, J. Fan, A. Migdall, and S. V. Polyakov, "Single-photon sources and detectors," *Review of scientific instruments*, vol. 82, no. 7, p. 071 101, 2011 (cit. on p. 23).

[70] J. H. Prechtel, A. V. Kuhlmann, J. Houel, L. Greuter, A. Ludwig, D. Reuter, A. D. Wieck, and R. J. Warburton, "Frequency-stabilized source of single photons from a solid-state qubit," *Physical review X*, vol. 3, no. 4, p. 041 006, 2013 (cit. on p. 23).

[71] E. M. Purcell, "Spontaneous emission probabilities at radio frequencies," in *Confined Electrons and Photons*, 1995, pp. 839–839 (cit. on p. 23).

[72] Z. Jacob, J.-Y. Kim, G. V. Naik, A. Boltasseva, E. E. Narimanov, and V. M. Shalaev, "Engineering photonic density of states using metamaterials," *Applied physics B*, vol. 100, no. 1, pp. 215–218, 2010 (cit. on p. 23).

[73] K. M. Schulz, H. Vu, S. Schwaiger, A. Rottler, T. Korn, D. Sonnenberg, T. Kipp, and S. Mendach, "Controlling the spontaneous emission rate of quantum wells in rolled-up hyperbolic metamaterials," *Physical review letters*, vol. 117, no. 8, p. 085 503, 2016 (cit. on p. 24).

[74] K. V. Sreekanth, Y. Alapan, M. ElKabbash, E. Ilker, M. Hinczewski, U. A. Gurkan, A. De Luca, and G. Strangi, "Extreme sensitivity biosensing platform based on hyperbolic metamaterials," *Nature materials*, vol. 15, no. 6, pp. 621–627, 2016 (cit. on p. 24).

[75] Y. Lee, S.-J. Kim, H. Park, and B. Lee, "Metamaterials and metasurfaces for sensor applications," *Sensors*, vol. 17, no. 8, p. 1726, 2017 (cit. on p. 24).

[76] Y. Guo, W. Newman, C. L. Cortes, and Z. Jacob, "Applications of hyperbolic metamaterial substrates," *Advances in OptoElectronics*, vol. 2012, 2012 (cit. on p. 24).

[77] C. S. Casari and A. Li Bassi, "Advances in laser and optics research. volume 7," in. Nova Science Publishers, 2011, ch. Pulsed Laser Deposition of Nanostructured Oxides: From Clusters to Functional Films (cit. on pp. 26–28).

[78] R. Eason, *Pulsed laser deposition of thin films: applications-led growth of functional materials*. John Wiley & Sons, 2007 (cit. on p. 26).

[79] P. Willmott and J. Huber, "Pulsed laser vaporization and deposition," *Reviews of Modern Physics*, vol. 72, no. 1, p. 315, 2000 (cit. on p. 26).

[80] F. Romeo, "Molybdenum coatings on rough graphite for applications in nuclear fusion devices and particle accelerators," Master's thesis, Politecnico di Milano, 2019 (cit. on p. 27).

[81] P. E. Flewitt and R. K. Wild, *Physical methods for materials characterisation*. CRC Press, 2017 (cit. on pp. 29, 30).

[82] D. Brandon and W. D. Kaplan, *Microstructural characterization of materials*. John Wiley & Sons, 2013 (cit. on p. 29).

[83] J. Chalmers and P. Griffiths, *Handbook of Vibrational Spectroscopy, 5 volumes set*. Wiley, 2002 (cit. on p. 30).

[84] L. J. van der Pauw, "A method of measuring the resistivity and Hall coefficient on lamellae of arbitrary shape," *Philips technical review*, vol. 20, pp. 220–224, 1958 (cit. on p. 32).

[85] P. Gondoni, "Nanostructured transparent conducting oxides for advanced photovoltaic applications," PhD thesis, Politecnico di Milano, 2014 (cit. on pp. 32, 33).

[86] B. R. Bricchi, "Engineering of titanium oxide and nitride nanostructures for plasmonic applications," PhD thesis, Politecnico di Milano, 2020 (cit. on p. 36).

[87] F. Di Fonzo, C. S. Casari, V. Russo, M. F. Brunella, A. Li Bassi, and C. E. Bottani, "Hierarchically organized nanostructured TiO_2 for photocatalysis applications," *Nanotechnology*, vol. 20, no. 1, p. 015 604, 2008 (cit. on p. 41).